Republic of Iraq
Ministry of Higher Education
and Scientific Research
University of Babylon
College of Education for Pure Sciences
Department of Physics

Study the energies $Cu_2O:CaF_2$ nanofilms prepared via thermal evaporation technique

A Thesis

Submitted to the Council of the College of Education for Pure Sciences at University of Babylon in Partial Fulfillment of the Requirements for the Degree of Master in Education/ Physics

By

Jenan Hashem Ali Abbas

B. Sc. in Physics

(University of Babylon 2012 A.D)

Supervised By

Prof. Dr. Khalid Haneen Abass

2023 A.D. **1445 A.H.**

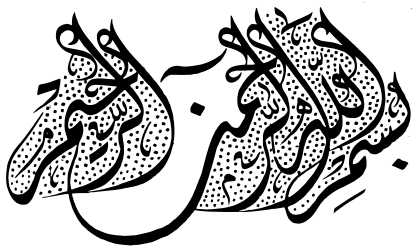

نَرْفَعُ دَرَجَاتٍ مَّن نَّشَاءُ وَفَوْقَ كُلِّ

ذِي عِلْمٍ عَلِيمٌ ﴿ ٧٦ ﴾

صدق الله العلي العظيم

سورة يوسف (الآية ٧٦)

Dedication

I dedicate this work to Allah who always provides me with strength knowledge, and wisdom in everything I do.

I dedicate this work to my husband and family, who encouraged and supported me throughout the study period

Jenan

Acknowledgments

I would like to express my deep gratitude and appreciation to my supervisors, Prof. Dr. Khalid Haneen Abass for his guidance, suggestions, and encouragement throughout the research work, without him, this thesis would have been impossible.

I would like to thank the members of my family for their help and encouragement. I would also like to thank my husband and everyone who helped me during the preparation of this thesis.

Jenan

Supervisor's Certificate

I certify that this thesis entitled " **Study the energies $Cu_2O:CaF_2$ nanofilms prepared via thermal evaporation technique**" was written by the student **(Jenan Hashem Ali Abbas)** under my supervision at the College of Education for Pure Sciences of University of Babylon in partial fulfillment of the requirements for the Degree of Master in Education/ Physics.

Signature

Name Dr. Khalid Haneen Abass

Title Professor

(Supervisor)

Date / / 2023

Head of the Department Certificate

In view of the available recommendations, I forward this thesis for debate by the examining committee.

Signature:

Name Dr. Khalid Haneen Abass

Title Professor

(Head of The Physics Department)

Date / / 2023

EXAMINATION COMMITTEE CERTIFICATION

I certify that we have read this thesis entitled (**Study the energies Cu_2O:CaF_2 nanofilms prepared via thermal evaporation technique**) and as committee, examined the student (**Jenan Hashem Ali Abbas**) its contents and that in our opinion it meets the standards of a thesis the Degree of Master in Education/ Physics.

Signature
Name
Title
Date / / 2023
(Chairman)

Signature:
Name
Title
Date / / 2023
(Member)

Signature
Name
Title
Date / / 2023
(Member)

Signature:
Name
Title
Date / / 2023
(Member)

Signature:
Name
Title
Date / / 2023
(Member/ Supervisor)

Approved by the Dean of the College

Signature:
Name
Title
Address Dean of the College.
Date / /2023

Abstract

In this work, $Cu_2O_{(0.75)}$:$CaF_{2(0.25)}$ thin films was prepared by thermal evaporation technique under pressure 1×10^{-7} mbar with rate of deposition 0.5 nm/sec. deposited on glass substrates at room temperature (RT) with different thickness (16, 19, 22, 29, 35, 42, 50 and 57) nm. The structural, morphological and optical properties were investigated. The X-ray diffraction (XRD) results showed that the prepared film were amorphous. With increasing thickness, the peak exhibited at 24.2º, which attributed to the CaF_2 that corresponded to the (111) with face center cubic, while the peak at corresponding to the $2\theta = 7^o$ may be attributed to the interaction between Cu_2O and CaF_2 NPs and Thus, it will lead to a phase mutation, and therefore this peak cannot be obtained by Miller indices. Atomic force microscopy (AFM) confirmed that the films grown by this technique had a good homogeneous surface. The roughness average, root mean square value, and average grain diameter increased with the increasing thickness. Field emission scanning electron microscope (FE-SEM) uniform morphology revealing a rather soft surface and with increase of the thickness led to changes in the morphology of the surface and increase the roughness.

The optical properties results showed that the absorbance, absorption coefficient, extinction coefficient, refractive index, real and imaginary dielectric constant and optical conductivity increased with increasing thickness while the transmittance and energy gap decreased with the increase of thickness. The Cu_2O:CaF_2 thin films allowed a direct energy gap (E_g) that was decreased from 3.77 to 3.62 eV with the increase of thickness. The surface energy loss function (SELF) and volume energy loss function (VELF) values observed that the SELF and VELF increased with the increase of thickness.

The dispersion parameters such as; E_o, E_d, n_o, n_2, M_{-1}, and M_{-3} were calculated using the Wemple–DiDomenico model. The value of the optical energy gap estimated by Wemple–DiDomenico calculations was consistent with the value of the optical energy gap obtained from the Tauc relation and found that the parameters were decreased with the increase of thickness.

Table of Content

No.	Subject	Page
	Dedication	
	Acknowledgments	
	Abstract	I
	Table of Content	IV
	List of Figures	VI
	List of Tables	VII
	List of Symbol and Abbreviation	X
Chapter One Introduction and Literature Review		
1.1	Introduction	1
1.2	Nanomaterials	2
1.3	Nanomaterials at the Experiment	4
1.3.1	Copper oxides (Cu_2O)	4
1.3.2	Calcium fluoride (CaF_2)	7
1.4	Literature Review	8
1.5	Aim of the Work	13
Chapter Two Theoretical Background		
2.1	Introduction	14
2.2	Thermal Evaporation	14
2.3	Structural and Morphological Properties	15
2.3.1	X-ray diffraction (XRD)	15
2.3.2	Field Emission Scanning Electron Microscope (FE-SEM)	16
2.3.3	Atomic Force Microscope (AFM)	17

2.4	Optical Properties of Crystalline Semiconductors	18
2.4.1	The electronic transitions	20
2.4.1.1	Direct transition	20
2.4.1.2	Indirect transitions	20
2.4.2	Optical constants	22
2.5	The Volume Energy Loss Function (VELF) and Surface Energy Loss Function (SELF)	23
2.6	Dispersion Parameters	25
Chapter Three Experimental Work		
3.1	Introduction	27
3.2	Nanomaterial at the Experiment	26
3.3	Substrate Preparation	28
3.4	Evaporation Boat	28
3.5	The Coating Unit	29
3.6	Thin Film Growth	30
3.7	Films Thickness Measurement	31
3.7.1	Optical measurement methods	31
3.7.2	The weight method	32
3.8	Structural and Morphological Measurements	32
3.8.1	X-ray diffraction (XRD)	32
3.8.2	Field emission scanning electron microscope (FE-SEM)	33
3.8.3	Atomic Force Microscope (AFM)	34
3.9	Optical Measurement	35
Chapter Four Results and Discussion		
4.1	Introduction	36
4.2	The Structural and Morphological Properties	36

4.2.1	X-ray diffraction (XRD)	36
4.2.2	Atomic force microscope (AFM)	41
4.2.3	Field emission scanning electron microscope (FE-SEM)	47
4.3	The Optical Properties	50
4.3.1	Absorbance (A)	50
4.3.2	Transmittance (T)	51
4.3.3	Absorption coefficient (α)	52
4.3.4	Optical energy gaps of the allowed direct transition	53
4.3.5	Extinction coefficient (k_o)	55
4.3.6	Refractive Index (n)	55
4.3.7	Real and imaginary parts of dielectric constant	56
4.3.8	The optical conductivity (σ)	58
4.4	The Volume Energy Loss Function (VELF) and Surface Energy Loss Function (SELF).	59
4.5	Dispersion Parameters	61
4.6	Conclusions	66
4.7	Future Works	67
References		68

List of Figures

No.	Subject	Page
1.1	Different Physical and Chemical Thin Film Deposition Processes	2
1.2	Schematic Representation of the 'Bottom up' and 'Top Down' Synthesis Processes of Nanomaterials	3
1.3	Classification of Nanomaterials (a) 0D Nanomaterials (b) 1D Nanomaterials (c) 2D Nanomaterials (d) 3D Nanomaterials	4
1.4	Crystal Structure of the Copper Oxide (Cu_2O)	6
1.5	Crystal Structure of the Calcium Fluoride (CaF_2)	7
2.1	Configuration of a Basic Coating System	14
2.2	Bragg's Diffraction	16
2.3	Field Emission Scanning Electron Microscope (FE-SEM)	17
2.4	Diagram of Atomic Force Microscope	18
2.5	Fundamental Absorption Edge of Crystalline Semiconductor	19
2.6	The Types of Transition	22
3.1	Schematic Diagram of Experimental Work	28
3.2	Molybdenum Evaporation Boat	29
3.3	Thermal Evaporation System	30
3.4	Basic Steps Deposition Processes	31
3.5	Optical Thin Film Measurement	32
3.6	The System of the XRD	34
3.7	Diagram of a System of FE-SEM Device	35
3.8	The System of AFM	35
3.9	The Photographic of UV-VIS-NIR Spectrophotometer	36
4.1	The XRD Spectra of Cu_2O:CaF_2 Thin Films with Different Thicknesses (a) 16 nm, (b) 19 nm, (c) 22 nm, (d) 29 nm, (e) 35 nm, (f) 42 nm, (g) 50 nm, (h) 57 nm	41

4.2	AFM Images of Cu_2O:CaF_2 Thin Films at Thickness 16 nm of a) 2D, b)3D, c) Grain Histogram, and d) Height Distribution	43
4.3	AFM Images of Cu_2O:CaF_2 Thin Films at Thickness 19 nm of a) 2D, b)3D, c) Grain Histogram, and d) Height Distribution	44
4.4	AFM Images of Cu_2O:CaF_2 Thin Films at Thickness 22 nm of a) 2D, b)3D, c) Grain Histogram, and d) Height Distribution	44
4.5	AFM Images of Cu_2O:CaF_2 Thin films at Thickness 29 nm of a) 2D, b) 3D, c) Grain Histogram, and d) Height distribution.	45
4.6	AFM Images of Cu_2O:CaF_2 Thin Films at Thickness 35 nm of a) 2D, b) 3D, c) Grain Histogram, and d) Height Distribution.	45
4.7	AFM Images of Cu_2O:CaF_2 Thin Films at Thickness 42 nm of a) 2D, b) 3D, c) Grain Histogram, and d) Height Distribution.	46
4.8	AFM Images of Cu_2O:CaF_2 Thin Films at Thickness 50 nm of a) 2D, b) 3D, c) Grain Histogram, and d) Height Distribution.	46
4.9	AFM images of Cu_2O:CaF_2 thin films at thickness 57 nm of a) 2D, b) 3D, c) Grain Histogram, and d) Height distribution	47
4.10	FE-SEM Images of Cu_2O:CaF_2 Thin Films with Different Thicknesses of a) 16 nm, b) 19 nm, c) 22 nm, d) 29 nm, e) 35 nm, f) 42 nm, g)50 nm and h) 57nm	51
4.11	The Transmittance Versus Wavelength of Cu_2O:CaF_2 Thin Films with Different Thicknesses	52
4.12	The Transmittance Versus Wavelength of Cu_2O:CaF_2 Thin Films with Different Thicknesses	53
4.13	The Absorption Coefficient Versus Wavelength of Cu_2O:CaF_2 Thin Films with Different Thicknesses	54
4.14	The Allowed Energy Gap Versus Photon Energy of Cu_2O:CaF_2 Thin Films with Different Thicknesses	55
4.15	The Extinction Coefficient Versus Wavelength of Cu_2O:CaF_2 Thin Films with Different Thicknesses	56

4.16	The Refractive Index Versus Wavelength of Cu_2O:CaF_2 Thin Films with Different Thicknesses	57
4.17	The Real Part of Dielectric Constant Versus Wavelength of Cu_2O:CaF_2 Thin Films with Different Thicknesses	58
4.18	The Imaginary Part of Dielectric Constant Versus Wavelength of Cu_2O:CaF_2 Thin Films with Different Thicknesses	58
4.19	The Optical Conductivity Versus Wavelength of Cu_2O:CaF_2 Thin Films with Different Thicknesses	59
4.20	Surface Energy Loss Functions as a Function of the Wavelength of Cu_2O:CaF_2 Thin Films with Different Thicknesses	61
4.21	Volume Energy Loss Functions as a Function of the Wavelength of Cu_2O:CaF_2 Thin Films with Different Thicknesses.	61
4.22	Plot of $(n^2 -1)^{-1}$ vs $(h\upsilon)^2$ of Cu_2O:CaF_2 Thin Film with Different Thicknesses of (a) 16 nm, (b) 19 nm, (c) 22 nm, (d) 29 nm, (e) 35 nm, (f) 42 nm, (g) 50 nm, (h) 57 nm.	66

List of Tables

No.	Subject	Page
1.1	Some Important Properties of Cu_2O	6
1.2	Some Important Properties of CaF_2	8
4.1	The Results of the XRD Data of Cu_2O:CaF_2 Thin Films at Different Thicknesses	42
4.2	Morphological Characteristics of Cu_2O:CaF_2 Thin Film with Different Thicknesses	47
4.3	The Values of Energy Gap of the Allowed Direct Transition of Cu_2O:CaF_2 Thin Film with Different Thicknesses	55
4.4	Dispersion Parameters of Cu_2O:CaF_2 Thin Film with Different Thicknesses	66

List of Symbols and Abbreviations

Symbol	Definition
MBE	Molecular beam epitaxy
CVD	Chemical vapor deposition
ALE	Atomic layer epitaxy
Cu_2O	Copper Oxides
CaF_2	Calcium fluoride
FCC	Face-centered cubic
λ	Wavelength
θ	Bragg diffraction angle
D	Crystallite size
FWHM	Full width at the half of the maximum intensity
FE-SEM	Field Emission Scanning Electron Microscope
XRD	X-ray diffraction
AFM	Atomic Force Microscope
ν	Frequency
h	Plank constant
$E_g^{opt.}$	Optical Energy gap
c	Speed of light in vacuum
Ep	The energy of absorbed or emitted phonon
K	The wave vector of electron
n	Refractive index
k_o	Extinction coefficient

ε_r	Real parts of dielectric constant
ε_i	Imaginary parts of dielectric constant
A	The absorbance
R	The reflectance
T	The transmittance
t	The sample thickness
σ_{op}	Optical conductivity
VELF	The volume energy loss function
SELF	The surface energy loss function
WDD	The Wemple–DiDomenico
E_o	Single oscillator
E_d	The dispersion energy
$n_o(0)$	The static refractive index
M_{-1} **and** M_{-3}	Moments of the optical spectra
d	Inter-planar spacing
λ_c	Wavelength cut off
υ_o	The critical frequency

Chapter One Introduction and Literature Review

1.1 Introduction

The expression of "Thin Films" is used to describe a layer or several layers of atoms for a certain substance whose thickness less than (1 μm) [1]. A thin film has physical properties that are different from those of their characteristic materials in their majority [2]. In 1852, the scientists Grove and Bunsen could be prepare these films by using Chemical Reaction and in 1857, the scientist Faraday was able to obtain a thin metal film by using Thermal Evaporation [3]. Thin films have large use today, because of their applied industries. These films have been used in different fields such as manufacturing (p-n) junctions, rectifiers, reflected and anti-reflected coating, photograph, mirrors with two types ordinary and thermally, integrated circuits, and of optical communications as light emitting diodes, detectors and solar cells, …., etc. for example, thin film (CdTe, ZnO, CdS, ..… etc) [4].

Based on the nature of deposition process, the methods employed for thin oxide film deposition can be divided into two group physical and chemical methods. All possible deposition processes are shown in Figure (1.1). The physical deposition processes include vacuum evaporation, laser ablation, molecular beam epitaxy (MBE), and sputtering. The chemical deposition processes comprise gas phase deposition methods and solution techniques. The gas phase methods are chemical vapor deposition (CVD) and atomic layer epitaxy (ALE), while spray pyrolysis, sol-gel, spin and dip-coating methods employ precursor solutions [5]. Nanomaterial's in principle, materials of which a single unit small sized (in at least one dimension) between (1 – 100) nm the usual definition of nanoscale and nanoscale defined as the "length range approximately from 1 nm to 100 nm". This includes both nanoobjects [6].

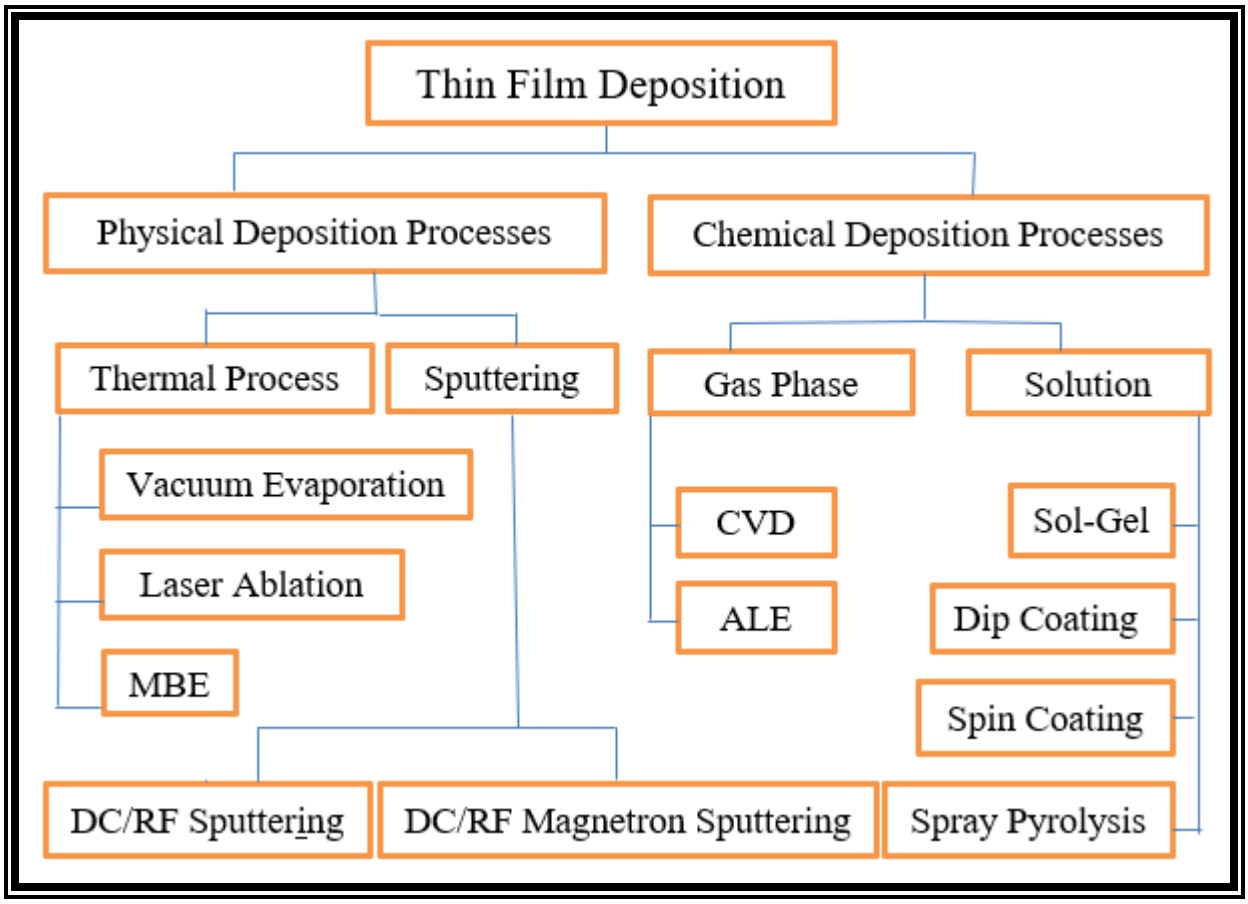

Fig.(1.1) Different Physical and Chemical Thin Film Deposition Processes [5].

1.2 Nanomaterials

Nanomaterial's research takes a materials science-based approach to nanotechnology, leveraging advances in materials metrology and synthesis which have been developed in support of microfabrication research. Materials with structure at the nanoscale often have unique optical, electronic, thermo-physical or mechanical properties [7-9]. Nanomaterials are slowly becoming commercialized [10] and beginning to emerge as commodities [11].

Obviously, there are two approaches to the synthesis of nanomaterials and the fabrication of nanostructures top-down and bottom-up as in Figure (1.2)**.** Attrition or milling is a typical top-down method in making nanomaterials [12-14].

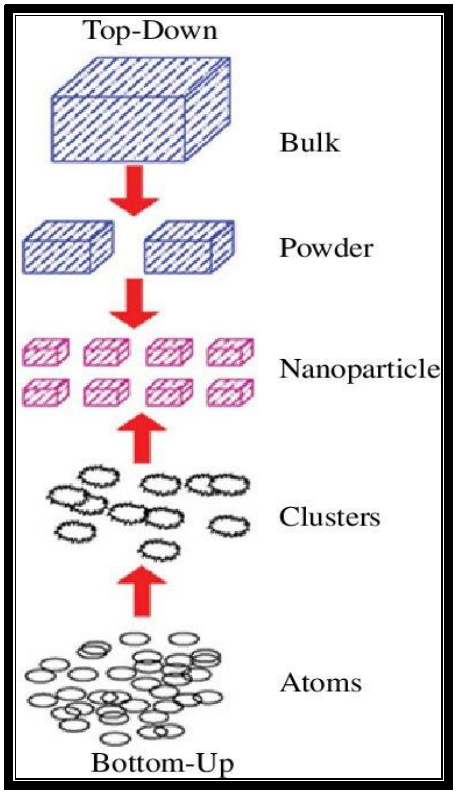

Fig (1.2) Schematic Representation of the 'Bottom up' and 'Top Down' Synthesis Processes of Nanomaterials [14].

The classification of nanomaterials is based on the number of dimensions, which are in nano range (≤ 100 nm) [15], as shown in Figure (1.3) [16]:

1- 0D nanomaterials have all the dimension within nanoscale, i.e. no dimension is larger than 100 nm. Nanoparticle is most common example for this classification. These nanoparticles can be crystalline or amorphous, metallic, ceramic, or polymeric.

2- 1D nanomaterials have at least one dimensions in nano range. This leads to needle like shaped materials having one dimension at nanoscale. 1D nanomaterial's include nanoplatelets, nanorods, nanoclays and nanosheets.

3- 2D nanomaterials have two dimensions in nano range. 2D nanomaterials include nanofibers, nanotubes, nanorods and whiskers. Carbon nanotubes are good example of 2D nanomaterials.

4- 3D nanomaterials have all three dimension is not nano range. 3D nanomaterials include nanogranules, nanoclays and equiaxed nanoparticles.

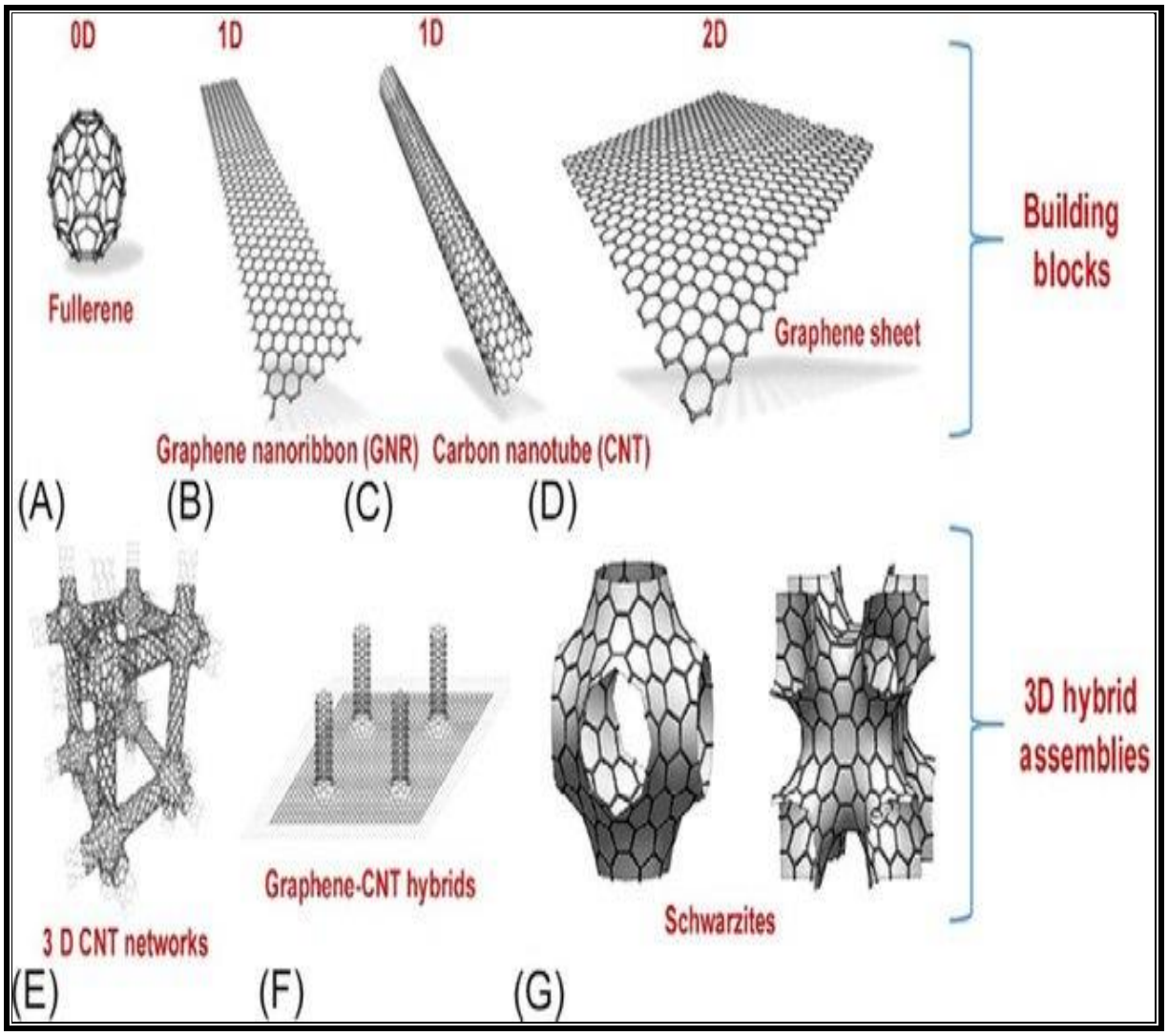

Fig (1.3) Classification of Nanomaterials (a) 0D Nanomaterials (b) 1D Nanomaterials (c) 2D Nanomaterials (d) 3D Nanomaterials [16].

1.3 Nanomaterials at the Experimental

1.3.1 Copper oxides (Cu_2O)

Metal oxides are one of these materials that are readily available and currently have a low cost of manufacturing in addition, copper oxides also have low toxicity, low band gap, and a high absorption coefficient which are all valuable qualities. The most popular forms of copper oxides include the following cupric oxide (CuO—tenorite in the mineral form), cuprous oxide (Cu_2O), and Cu_4O_3 (paramelaconite in the mineral form) [17].

The paramelaconite is a meta-stable copper oxide, which is an intermediate compound between CuO and Cu_2O. The stable forms are the CuO and the Cu_2O. Both show promising qualities due to their electrical and optical properties [18]. The CuO has a dark brown/black color and the Cu_2O is a yellow/ red color. In the presence of moist air, the Cu_2O will change into CuO. The CuO has a smaller band gap than Cu_2O and as a result, is potentially superior in photon-detection and optical switching applications that are used in combination with visible and near-infrared spectrums [19]. The Cu_2O has a cubic structure as shown in Figure (1.4) [20] and a band gap between 2.0 eV and 2.6 eV [21]. The CuO has a monoclinic (a group of crystalline solids whose crystals have three axes of unequal length, with two being perpendicular to one another) structure with a bandgap between 1.3 eV and 2.2 eV [21].

Copper oxides (Cu_2O) is potentially a good candidate for solar cell applications due to high electron mobility and high optical absorptivity in the visible spectrum. It also has high conductivity and low electrical resistivity. The copper oxides are p-type semiconductors and are usually coupled with n-type semiconductors like zinc oxide (ZnO), silicon (Si), and cadmium sulfide (CdS). The high conduction of the p-type copper oxide is attributed mainly to the negatively charged copper (Cu) vacancies [21]. it has shown great promise for a variety of applications including water splitting [22,23], gas sensing [24,25], photocatalysis [26, 27] and photovoltaics [28-30]. In particular, thin film Cu_2O has the potential to serve as the light-harvesting material in photovoltaic applications and has shown to be the most promising p-type semiconductor oxide considered for the fabrication of low-cost, all-oxide solar cells [28]. Cu_2O nano films can be synthesized using a variety of physical and chemical methods, including thermal oxidation [28], rf-sputtering [29], pulsed laser deposition [31], chemical vapor deposition [32] and electrochemical deposition [30]. Table (1.1) explain some physical properties of Cu_2O [33].

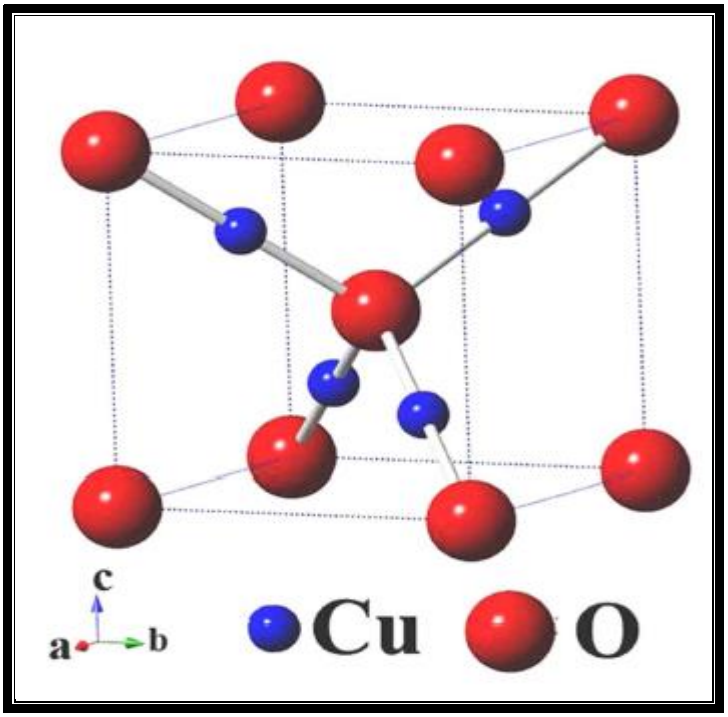

Fig (1.4) Crystal Structure of the Copper Oxide (Cu_2O) [20].

Table (1.1) Some Important Properties of Cu_2O [21,33].

Property	Value
Symbol	Cu_2O
Colour	black to brown
Type of conductivity	p-type
Crystal structure	cubic
Energy gap	2.1 eV
Density	$6.31 g/cm^3$
Melting point	1232^oC
Boiling point	1800^oC
Refractive index	1.4

1.3.2 Calcium Fluoride (CaF_2)

Considering the high technological importance of calcium fluoride (CaF_2), it is not surprising, that during the last years, it has been the subject of many experimental and theoretical studies [34]. The superionic conductor, CaF_2, crystallize in the cubic fluorite structure and constitute an important class of relatively simple ionic crystals whose optical and lattice-dynamical properties are of much theoretical and experimental interest. Calcium fluoride (CaF_2) is a face-centered cubic (FCC) crystal formed by the calcium (Ca^{2+}) and the fluoride (F^{1-}) ions as shown in Figure (1.5). The experimental lattice constant of this compound is 5.46 Å. It is an indirect band gap material with high band gap value of 12 eV [35]. Numerous techniques have been introduced for depositing CaF_2 thin films on substrates for various purposes such as electron beam evaporation [36–39], radio frequency magnetron sputtering [40], molecular beam epitaxial [41], pulsed laser deposition [42,43] and thermionic vacuum arc [44]. From these techniques, thermal evaporation has been found to be the most suitable because of its advantages of large-area deposition, low-temperature, and simple process, and it has been proven to be a cheap fabrication process [45]. Table (1.2) explain some physical properties of CaF_2 [35,46]

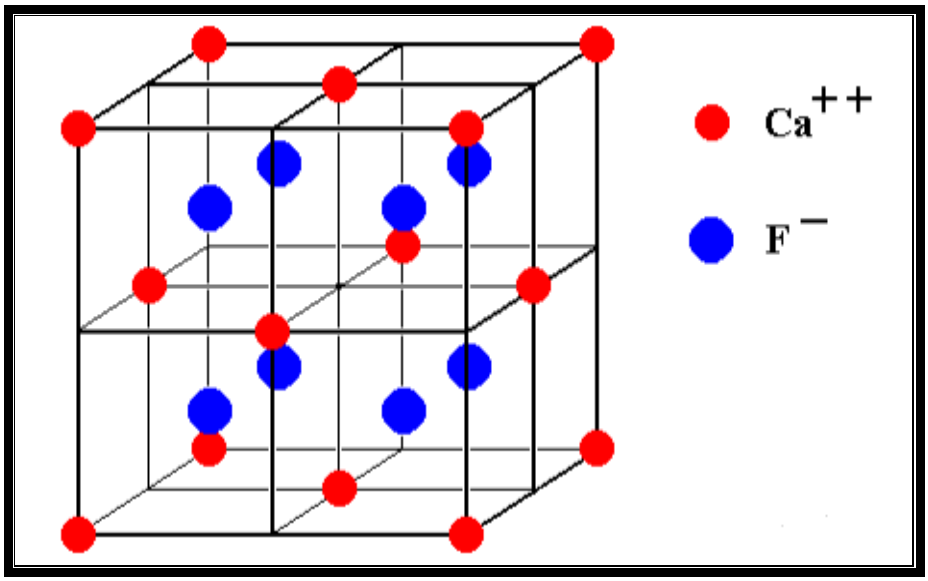

Fig (1.5) Crystal Structure of the Calcium Fluoride (CaF_2) [35].

Table (1.2) Some Important Properties of CaF_2 [35,46].

Property	Value
Symbol	CaF_2
Colour	White crystalline solid (single crystals are transparent)
Type of conductivity	n-type
Crystal structure	cubic
Energy gap	12 eV
Density	3.18 g/cm^3
Melting point	1418 °C
Boiling point	2533 °C
Refractive index	1.43

1.4 Literature Review

In 2015, D. S. Murali, *et. al.* [47] prepared transparent Cu_2O thin films using magnetron sputtering at 300 K on glass substrates and vacuum annealing (5×10^{-6} mbar at 700 K for 1 h). The Cu_2O thin films are p-type and show enhanced properties grain size (54.7 nm), optical transmission 72% (at 600 nm) and Hall mobility 51 cm2/Vs. The bulk and surface Valence band spectra of Cu_2O and CuO thin films are studied by temperature dependent Hall effect and Ultra violet photo electron Spectroscopy (UPS). CuO thin films show a significant band bending downwards (due to higher hole concentration) than Cu_2O thin films

In 2016, Y. Yang, *et. al.* [48] worked on the formation of Cu_2O films from an alkaline copper-lactate electrolyte using potentiostatic pulse electrodeposition has been conducted. The resulting films were examined using

SEM and XRD techniques and compared with those obtained from DC electro-deposition. It was shown that the morphology of Cu_2O films can be controlled by manipulating the on- and off-times during pulsed electro-deposition. By increasing the pulsing frequency or reducing the duty cycle, the typical cubic morphology of the Cu_2O films obtained under DC conditions can become truncated and less angular, leading to the formation of spherical particles.

In 2017, N. A. Raship, *et. al.* [49] studied copper oxide films which were grown on silicon substrates by sol-gel dip coating method. In order to study the effects of annealing temperature on the properties of copper oxide films, the temperature was varied from 200 ^oC to 450^oC. From the XRD results, we found that pure cuprite (Cu_2O) phase can be obtained by annealing the films annealed at 200 ^oC. Films annealed at 300^oC had a combination phase which consists of tenorite (CuO) and cuprite (Cu_2O) phase while pure tenorite (CuO) phase can be obtained at 450 ^oC annealing temperature. The surface microstructure showed that the grains size is increased whereas the surface roughness is increased and then decreases by increasing in annealing temperature. The films showed that the resistivity decreased with increasing annealing temperature. Consequently, it was observed that annealing temperature has strong effects on the structural, morphological and electrical properties of copper oxide films.

In 2018, R. D. Prabu, *et. al.* [50] deposited Cu_2O thin films by Nebulizer Spray Pyrolysis technique using different pressure rates. The structural studies confirmed that the deposited Cu_2O thin films are in polycrystalline nature having cubic crystal structure. Laser Raman analysis confirmed that all peaks are correspond to Cu_2O phase. Optical analysis showed band gap values 2.26, 2.12 and 1.99 eV for pressures 1, 2 and 3 bars، respectively. Photoluminescence analysis confirmed that the emission peak obtained at 617 nm corresponds to cuprous oxide phase. Films deposited at high pressure i.e. 3 bars showed low resistivity 1.73×102 Ω.cm. Solar cells were fabricated using the depo sited Cu_2O film with ZnO as heterojunction that showed fill factor values 0.29, 0.35 and

0.39 for pressures 1, 2 and 3 bars, respectively. The power conversion efficiency (η) was increased from 0.039 to 0.57% (about 15 times) by increasing the pressure from 1 to 3 bars.

In 2019, C. Qin, *et. al.* [51] demonstrated an effective surface passivation method to enhance the power conversion efficiency of Cu_2O/SnO_2 heterojunction solar cell by modifying Cu_2O surface with an ultrathin MgO layer. The MgO layer deposited by E-Beam Evaporation in high-vacuum was found to be more metallic, and the availability of elemental Mg could reduce the CuO oxidation state efficiently forming a stoichiometry Cu_2O surface confirmed by high-resolution XPS. J-V measurements under dark condition show an order of magnitude reduction in dark saturation current density after MgO modification. Finally, great enhancement was achieved in PCE by introducing a 1-nm-thick MgO layer to Cu_2O/SnO_2 heterojunction.

In 2020, M. A. Zahid, *et. al.* [52] deposited calcium fluoride (CaF_2) via vacuum thermal evaporation on borosilicate glass to produce an anti-reflection coating for use in solar modules. Experimentally, a 120 nm thin CaF_2 film on glass shows an average increase of ~4% in transmittance and a decrease of ~3.2% in reflectance، respectively, the electrical PV performance of CaF_2-coated glass (CaF_2-CG) was analyzed for conventional and lightweight photovoltaic module applications. An improvement in the short-circuit current (J_{sc}) from 38.13 to 39.07 mA/cm^2 and an increase of 2.40% in the efficiency (η) was obtained when CaF_2-CG glass was used instead of Un CG in a conventional module. Furthermore، J_{sc} enhancement from 35.63 to 36.44 mA/cm^2 and improvement of 2.32% was observed when a very thin CaF_2-CG was placed between the polymethyl methacrylate (PMMA) and solar cell in a lightweight module.

In 2020, D. O. Ozaslan, *et. al.* [53] prepared Cu_2O film on a glass substrate at 70 °C by the SILAR (Succesive Ionic Layer Adsorption and

Reaction) method. The Cu_2O film was annealed in an air atmosphere at 100 ^oC, 300 °C, and 500 °C temperatures for one hour and the effect of the annealing temperature on the physical properties was investigated. The phase-transition temperature that corresponds to the transformation from Cu_2O to CuO was occurred at temperature of approximately 300 ^oC with annealing process. The energy band gap (E_g) was reduced from 2.57 eV to 1.91 eV with the increasing annealing temperature. Hall measurement revealed that the film showed p-type conductivity, while the film annealed at 300 °C and 500 °C the resistivity of CuO was found to be 8.23×10^3 and 5.11×10^2 Ω.cm, respectively.

In 2020, S. M. Butte and S. A. Waghuley [54] prepared CuO and Cu_2O by calcination process. The average crystallite size calculated from Scherrer formula of as synthesize sample. The crystallite size is found to be 6.39 nm and for CuO nanoparticles is 27.17 nm. The PL spectra for Cu_2O nanoparticles shows the peaks at 470 nm and 390 nm respectively. For CuO nanoparticle the peaks obtained at 393 nm, 470 nm and 494 nm. The UV visible spectroscopy shows the presence of Cu_2O due to increase in intensity and the decreased response in CuO absorption peak is due to the deformation of lattice due to strain produced by inelastic scattering of charge carries by photons and imperfection also internal electrical fields within the crystal.

In 2021, R. Bunea, *et. al.* [55] prepared CuO thin films utilizing RF sputtering technique with deposition occurring at room temperature followed by thermal annealing between 100˚C and 400˚C and using different gases, oxygen (O_2) (oxidizing and reactive gas) and nitrogen (N_2) (inert gas), besides air. In addition, the CuO results were compared to our Cu_2O results from a previous study to assess their differences, the CuO thin film initially had a bandgap of 2.19 eV at room temperature and by increasing the annealing temperature to different levels, the band gap decreased respectively. The presence of air in the chamber allowed for the highest decrease, followed by the nitrogen (N_2) and the lowest decrease was observed in the presence of oxygen (O_2). This was reflected

in the decrease in the bandgap values from 2.19 eV (room temperature) to 2.05 eV for the films annealed at 400 ˚C.

In 2022, E. Güneri*, et. al.* [56] cuprous oxide (Cu_2O) thin films were prepared for the different weights (0.08, 0.09, 0.10, 0.13, and 0.14 g) on glass substrates by the chemical bath deposition (CBD) method. The effects of weight on the structural, morphological, and optical properties of thin films were investigated. The XRD pattern shows cubic structured Cu_2O thin films and the crystallinity is increased with an increase in weight. The average crystallite size is also increased from 10 to 17 nm. The FESEM images picturized cubic and irregular-shaped non-homogeneous particles. The transmittance is found to be decreased with an increase in weight. The direct energy bandgap decreased from 2.26 eV to 2.17 eV as the weight increased. Also, the extinction coefficient, refractive index, and dielectric coefficients have been affected by the variation of weight.

In 2023, A. M. Koshy*, et. al.* [57] prepared copper oxide thin films are deposited on quartz substrates by DC magnetron sputtering and the effect of deposition temperature on the optical properties is examined in detail. Sputter deposition is carried out with the substrate at room temperature and at elevated temperatures between 200 and 300 °C. XRD analysis indicates that the oxide formed is primarily Cu_2O and the absorption spectra show a critical absorption edge at around 300 nm. The sheet resistance gradually decreases with increase in deposition temperature, corresponding to an increase in the conductivity of the films. Also observed is an increase in the band gap energy from 2.02 eV for room temperature deposition to 2.35 eV at 300 °C, corresponding to an improved film crystallinity and reduction in defect density.

1.5 Aims of the Work

The aims of this study the properties of Cu_2O:CaF_2 thin films using thermal evaporation method. The other objectives can be achieved through this study such as structural, morphological and optical properties and can be prepared devices for some application.

Chapter Two

Theoretical Background

2.1 Introduction

This chapter focuses on the theoretical part which represented thermal evaporation, structural and morphological properties (X-ray, scanning electron microscope, diffraction, atomic force microscopy (AFM) and optical properties of crystalline semiconductors.

2.2 Thermal Evaporation

A thermal evaporator uses an electric resistance heater to melt the material and raise its vapor pressure to a useful range. This is done in a high vacuum, both to allow the vapor to reach the substrate without reacting with or scattering against other gas-phase atoms in the chamber, and reduce the incorporation of impurities from the residual gas in the vacuum chamber [58,59]. Thermal evaporation is the simplest way of depositing material onto a substrate under pressure $1x10^{-7}$mbar and given excellent purity of films. Figure (2.1) explains the configuration of a basic coating system [60,61].

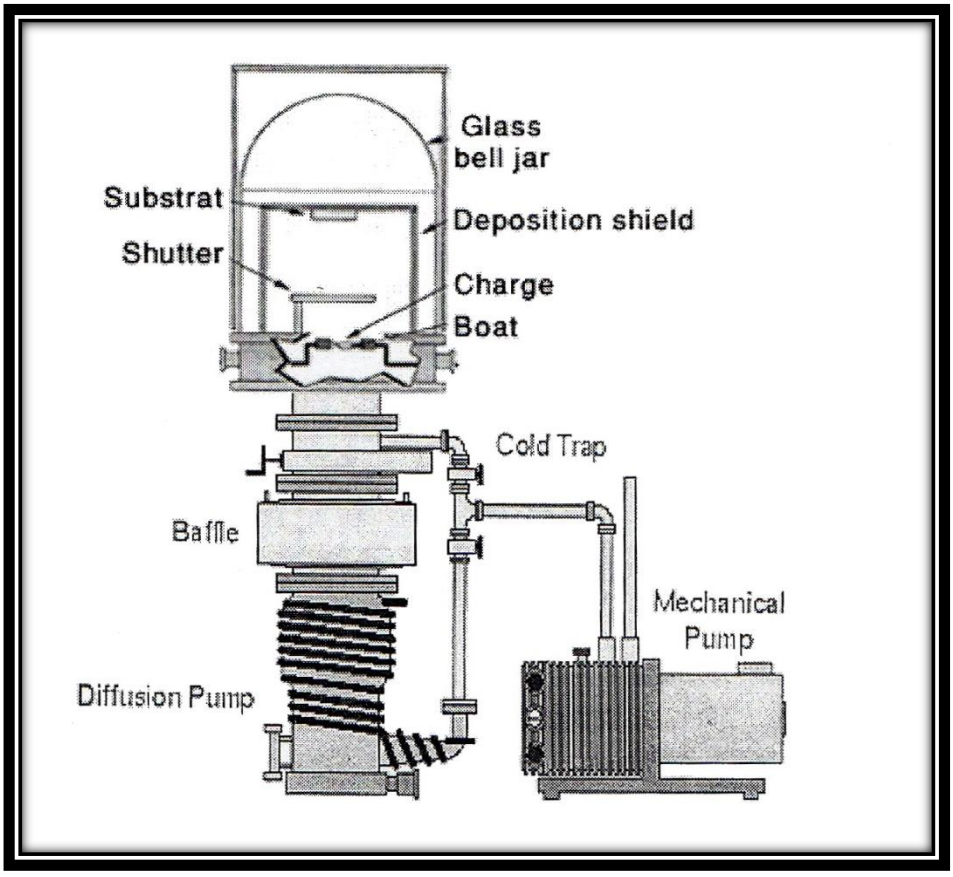

Fig (2.1) Configuration of a Basic Coating System [61].

2.3 Structural and Morphological Properties

2.3.1 X-ray Diffraction (XRD)

It is possible to apply XRD to investigate the crystallization process, unit cell lattice parameter detail, crystal structure, crystal orientation, and crystallite size, which is a fast and effective approach. The constructive interference of a monochromatic beam of X-rays is used to produce the XRD peaks after scattered of each set of lattice planes in the sample at specific angles, where the distribution of the atoms determines the peak intensities within lattice. Therefore, the periodic atomic fingerprint of materials is represented by XRD pattern [62].

The sample holder, X-ray tube, and X-ray detector are the three basic components of an X-ray diffractometer. The cathode ray tube is responsible for creating X-rays by burning the filament to create electrons, which are subsequently driven toward a target by a voltage and attack the target substance. When electrons with sufficient energy displace inner shell electrons of the target material, X-ray spectra are produced [63].

When X-ray light of wavelength (λ) is projected at an angle (θ) onto a crystal lattice, the incoming X-rays interact constructively with the sample if the circumstances meet Bragg's law, as shown in Fig (2.4) [64]:

$$2d_{hkl}sin\theta = \lambda \qquad (2\text{-}1)$$

Where $d_{hkl} = d/n$, θ is Bragg diffraction angle (degree) and λ is wavelength for incident X-ray beam (Å).

The crystallite size (D), can be estimated using the Scherer's formula [65]:

$$D = 0.9\lambda/\beta cos\theta \qquad (2\text{-}2)$$

Where λ is the X-ray wavelength (Å), β is the full width at the half of the maximum intensity (FWHM)(radian), θ is Bragg diffraction angle of the XRD peak (degree).

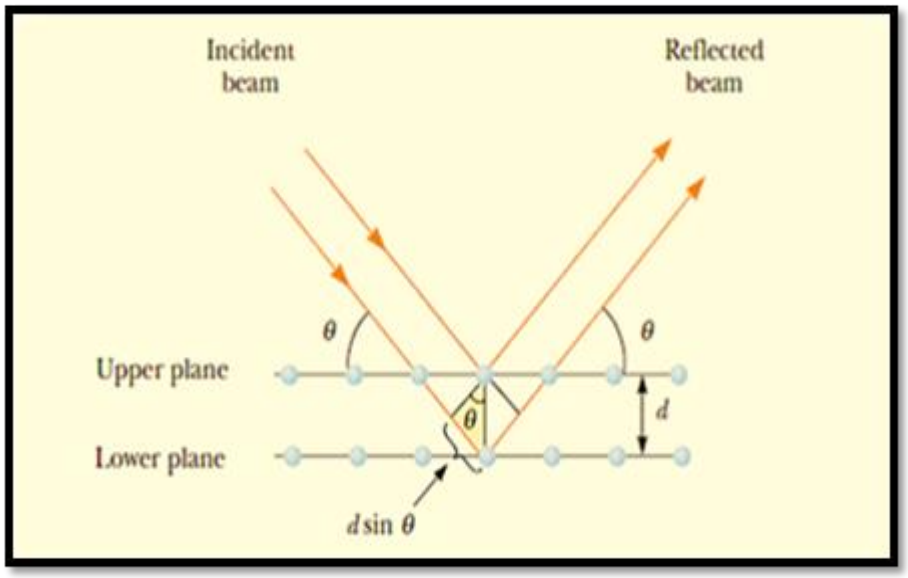

Fig (2.2) Bragg's Diffraction [64].

2.3.2 Field Emission Scanning Electron Microscope (FE-SEM)

The field emission scanning electron microscope is undoubtedly one of the most important electron beam technology inventions of the twentieth century. Ever since the first commercial instrument appeared in the early 1960s, the design of the scanning electron microscope has been constantly evolving and improving [66]. Recognition that the FE-SEM is much more than a powerful microscope came early. In addition to providing high-resolution topographical images of the surface of a specimen, it was realized that the FE-SEM could also provide a variety of different contrast modes, where information relating to things like the surface voltage is embedded in its output signals [66]. FE-SEM has a magnification range of 5 to 300, 000 times, and an acceleration voltage parameter for a coating analysis range between 10 and 20 kV, at higher magnifications, much more surface detail is visible in biological samples when

using an acceleration voltage between 2 kV and 300 V are shown in Fig (2.3) [67].

FE-SEM is commonly used in metallurgy, geology, biology, and medicine, where the user can obtain a strong depth of view with high magnification images and analyze individual crystals or other features [66]. When using in combination with the closely related technique of energy-dispersive X-ray microanalysis, a high-resolution FE-SEM image will display information down to 25 Angstroms, or better. One may decide the composition of individual crystals or features [68].

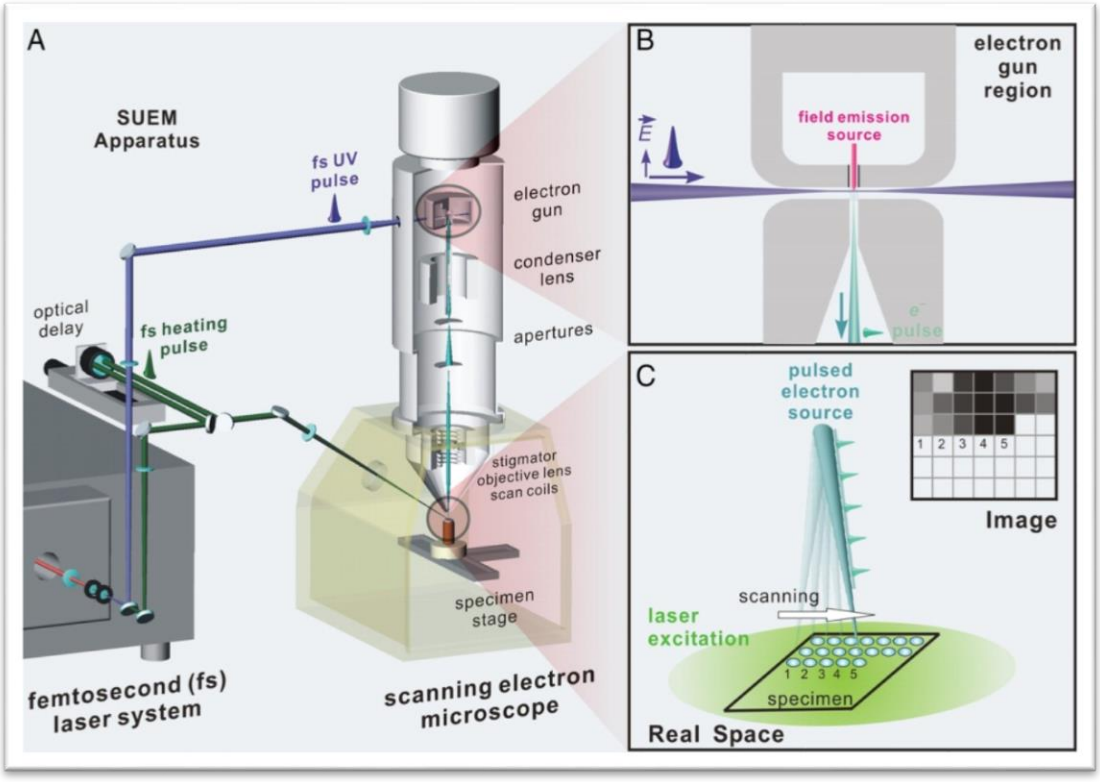

Fig (2.3) Field Emission Scanning Electron Microscope (FE-SEM) [67].

2.3.3 Atomic Force Microscope (AFM)

The atomic force microscopy (AFM) is a mechanical imaging instrument that measures the three-dimensional topography as well as physical properties of a surface with a sharpened probe. The sharpened probe is positioned close

enough to the surface such that it can interact with the force fields associated with the surface. Then the probe is scanned across the surface such that the forces between the probe remain constant [69]. An image of the surface is then reconstructed by monitoring the precise motion of the probe as it is scanned over the surface. Typically, the probe is scanned in a raster-like pattern. (AFM) analyses in order to find the average grain size and surface topography at atomic scale of the samples [70], as shown in Figure (2.4).

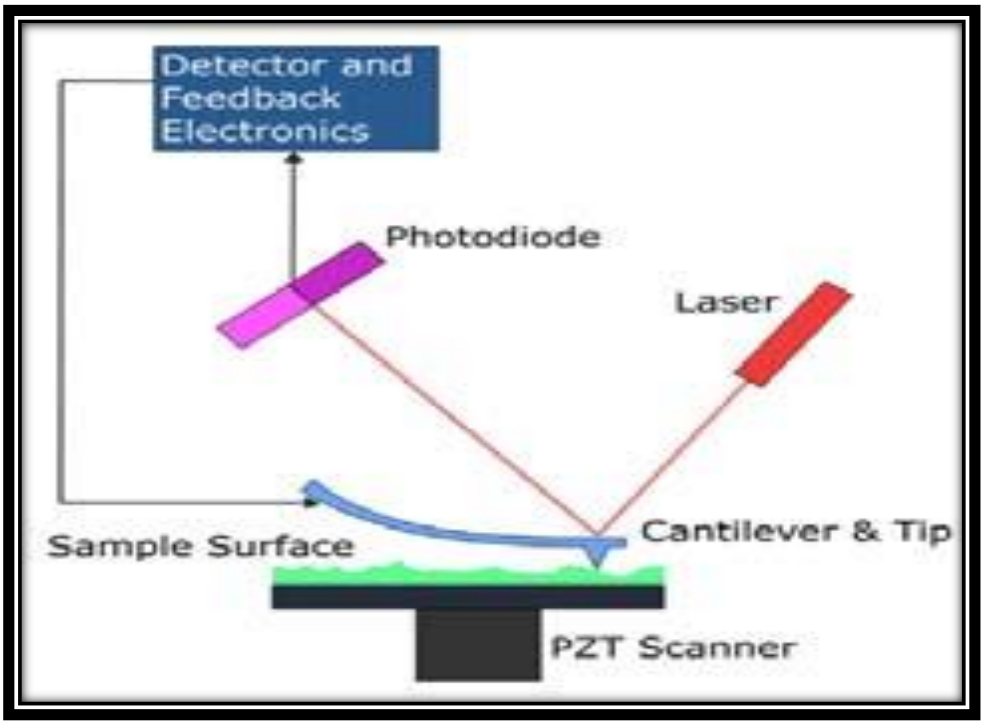

Fig. (2.4) Diagram of Atomic Force Microscope [70].

2.4 Optical Properties of Crystalline Semiconductors

The process of basically absorptance in crystalline semiconductors for incident rays happens when an electron in valance band absorbs high energy from incident photon to escape to conduction band if the photon energy(hν) is equal or larger than forbidden energy gap (E_g) [71].

$$h\nu \geq E_g \qquad (2\text{-}3)$$

where ν is the frequency in (Hz) and (h) Plank constant (6.625×10^{-34}J.s). Spectroscopy of incident ray's region which start electrons in its transporting is

called (fundamental absorption edge). The fundamental absorption edge is one of the greatest striking features of the absorption spectrum of a semiconductor. It equals the difference between top valence band and bottom conduction band, as shown in Figure (2.5) [72].

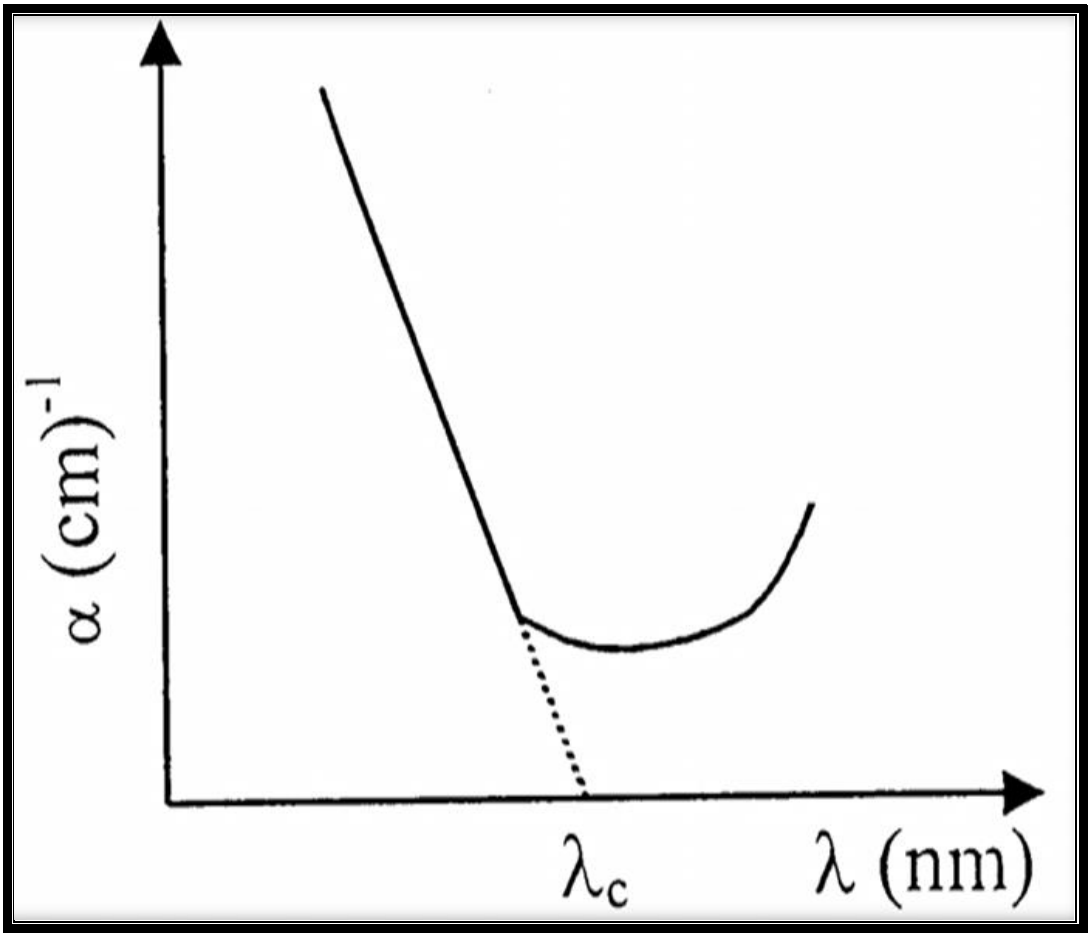

Fig (2.5) Fundamental Absorption Edge of Crystalline Semiconductor [72].

When ($E_g=h\nu_o$) where (ν_o) is called critical frequency and the wavelength facing it is called wavelength cut off (λ_c). This process happens when the width of forbidden energy gap equals to incident energy photon which can be expressed in equation (2-3) [73]:

$$\lambda(nm) = \frac{hc}{E_g} = \frac{1240}{E_g\ (eV)} \qquad (2\text{-}4)$$

where (c) is speed of light in vacuum.

The absorbance occurs when light passes through a material and the intensity is reduced based on the colors that are absorbed. It can be defined as the ratio between absorbed light intensity (I_A) by material and the incident intensity of light (I_o) [73]

$$A = \frac{I_A}{I_O} \qquad (2\text{-}5)$$

The intensity of transmitted rays from the film (I_T) over the intensity of incident rays on the film (I_o) is called the transmittance (T), and can be obtained as follows [73]:

$$T = \frac{I_T}{I_o} \qquad (2\text{-}6)$$

2.4.1 The Electronic Transitions

The electronic transitions can be classified basically into two types [75]:

2.4.1.1 Direct Transition

This transition happens in semiconductors when the bottom of conduction band (C.B) is exactly over the top of valence band (V.B). This means that they have the same value of wave vector ($\Delta K=0$). In this state, the absorption seems when ($E_g=h\upsilon$). This transition type needed the laws of conservation in energy and momentum. There are two types of direct transitions, they are [75]:

a) Allowed direct transition

Figure (2-6-a) shows this transition happens from top points in the (V. B) and the bottom point in the (C. B.). The empirical relationship for this type of transition is given by the equation [75]:

$$\alpha h\nu \approx \beta\left[h\nu - E_g\right]^{1/2} \qquad (2\text{-}7)$$

b) Forbidden direct transitions

Figure (2-6-b) shows these transition happens from near the top points of (V. B) and the near bottom points of (C.B).The empirical relationship which corresponds to this transition is given by the equation[76]:

$$\alpha h\nu \approx \beta\left[h\nu - E_g\right]^{3/2} \qquad (2\text{-}8)$$

2.4.1.2 Indirect Transitions

This transition happens when the bottom of (C.B) is not over the top of (V.B), in curve (E-K). The electron transits from (V.B) is not perpendicularly where the value of the wave vector of electron before and after transition is not equal ($\Delta K \neq 0$). This transition type happens with the help of a like particle called "Phonon", for conservation of the energy and momentum law. Therefore, assistance of a phonon is necessary to conserve the momentum, so [76]:

$$h\nu \approx E_g \pm E_P \qquad (2\text{-}9)$$

$$hk_f \approx hk_i \pm hk_P \qquad (2\text{-}10)$$

where E_p is the energy of absorbed or emitted phonon.

c) Allowed indirect transitions

Figure (2-6-c) shows this transition occurring between the top of (V.B) and the bottom of (C.B) which are found in the difference region of (K-space), so that [76]

$$\alpha h\nu \approx \left[h\nu - E_g\right]^2 \pm \mathrm{E_{ph}} \qquad (2\text{-}11)$$

d) Forbidden indirect transitions

Figure (2-6-d) shows this transition occurring between near points in the top of (V.B) and near points in the bottom of (C.B). The absorption coefficient for transition with a phonon absorption is given by following equation [77]

$$\alpha h\nu \approx \left[h\nu - E_g\right]^3 \pm \mathrm{E_{ph}} \qquad (2\text{-}12)$$

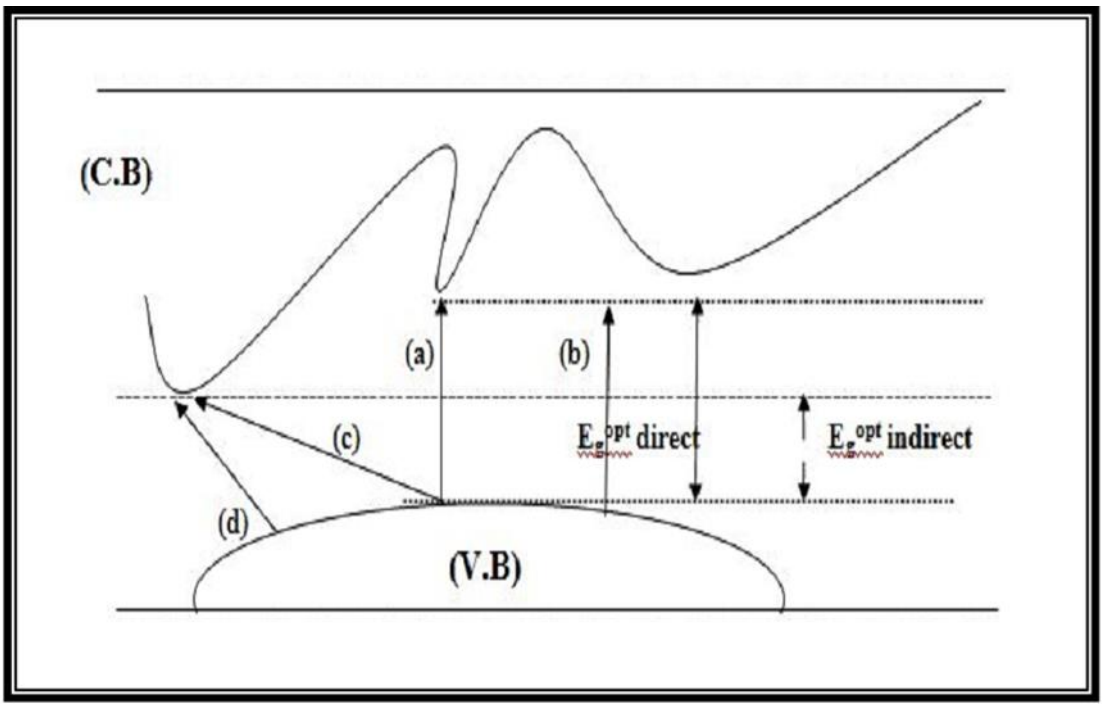

Fig. (2.6) The Types of Transition [75] .

(a) Allowed direct, (b) Forbidden direct, (c) Allowed indirect, (d) Forbidden indirect.

2.4.2 Optical Constants

The optical constants are very necessary parameters because they describe the optical behavior of the materials. The extraction of optical constants from different types of optical measurement is a field of widespread interest [78]. Optical constants included refractive index (n), extinction coefficient (k_o), real (ε_r) and imaginary (ε_i) parts of dielectric constant [79].

$$n = \left(\frac{4R}{(R-1)^2} - k^2\right)^{1/2} + \frac{(R+1)}{(R-1)} \qquad (2\text{-}13)$$

where (R) is the reflectance.

The extinction coefficient (k_o) is related to the exponential decay of the wave as it passes through the medium and it is defined [80]:

$$k_0 = \frac{\alpha\lambda}{4\pi} \qquad (2\text{-}14)$$

where (λ) is the wavelength of the incident radiation and (α) is given by[80]:

$$\alpha = 2.303\frac{A}{t} \quad (2\text{-}15)$$

(A) is the absorbance, and (t) is the sample thickness. And (R) is calculated from the following equation [80]:

$$R + T + A = 1 \quad (2\text{-}16)$$

Dielectric constant represents the ability of material to polarization, whose expression, is given by the following equation [81]:

$$\varepsilon = \varepsilon_1 - i\varepsilon_2 \quad (2\text{-}17)$$

$$\varepsilon = (n^*)^2 \quad (2\text{-}18)$$

$$(n - ik_0)^2 = \varepsilon_1 - i\varepsilon_2 \quad (2\text{-}19)$$

$$\varepsilon = (n^2 - k_0^2) - i(2nk_0) \quad (2\text{-}20)$$

From equation (2-19) and (2-20) real and imaginary complex dielectric coefficient can be written as in following equation [81]:

$$\varepsilon_r = n^2 - k_0^2 \quad (2\text{-}21)$$

$$\varepsilon_i = 2nk_0 \quad (2\text{-}22)$$

The optical conductivity (σ_{op}) has been determined from the following equation [81]

$$\sigma_{Op} = \alpha\frac{nc}{4\pi} \quad (2\text{-}23)$$

2.5 The Volume Energy Loss Function (VELF) and Surface Energy Loss Function (SELF)

The function of energy loss is another crucial factor that may be used to demonstrate the optical-transitions of electrons in thin-film materials. The process of energy dissipation can be conceptualized as the energy-dependent passage of multiple or single free carriers through a material. The light energy received by these single or multiple carriers is dissipated either in the bulk (volume) or at the surface of the material. The ensuing heat loss is denoted by the acronym (ELF) and is split into two distinct categories (VELF) for losses in volume and (SELF) for losses on the surface. Using the complex dielectric constants [82], we can calculate the SELF and VELF:

$$SELF = \frac{\varepsilon_r}{(\varepsilon_r+1)^2+\varepsilon_i^2} \quad (2\text{-}24)$$

$$VELF = \frac{\varepsilon_i}{(\varepsilon_r)^2+\varepsilon_i^2} \quad (2\text{-}25)$$

here, ε_i is the imaginary dielectric constant, while ε_r is the real dielectric constant.

2.6 Dispersion Parameters

The dispersion parameters are very important in many applications such as optical communications and in the design of optical devices. The Wemple–DiDomenico (WDD) single effective oscillator model accurately describes the refractive index dispersion [83]. This model provides an understandable physical interpretation for the observed parameters, which aids in fitting the experimental results [84]. The energy of the effective single oscillator (E_o) and the dispersion energy (E_d) are the model's primary outputs.

The energy (E_o), or average energy gap, provides quantitative information about the material's overall band structure. It must be considered that the information gained through (E_o) is completely different from to that obtained from the optical energy gap (E_g). The optical energy gap is related to the material's optical characteristics near its basic absorption edge. In spite of the difference be showing that the oscillator energy, (E_o) is often twice the optical energy gap, (E_g) i.e. ($E_o \approx 2E_g$) [83]. On the other hand, the dispersion energy (E_d), which is a measure of oscillator strength, quantifies the average energy of inter band optical transitions and is associated to the sample's structural order, i.e, it is related to the ionicity, anion valency and coordination number of the material. It's worth noting at this point that the dispersion energy (E_d) is almost completely independent of the effective single oscillator energy, (E_o). This is because E_d is proportional to the dielectric loss, whereas (E_o) is independent of the dielectric loss, either close or from afar. The relationship between (E_o, E_d) and incident photon energy (hυ) is as follows according to the (WDD) model [83,85].

$$(n^2 - 1) = \frac{E_d\, E_0}{E_0^2 - (h\nu)^2} \qquad (2\text{-}26)$$

where n refractive index, E_o the energy of the effective single oscillator, E_d the dispersion energy, hυ incident photon energy.

The static refractive index $n_0(0)$ and the static dielectric constant can be obtained from the following relations [86]

$$n_2(0) = 1 + \frac{E_d}{E_o} \quad (2\text{-}27)$$

The M_{-1} and M_{-3} moments of the optical spectra can be obtained from the relationships [87]:

$$E_0^2 = \frac{M_{-1}}{M_{-3}} \quad (2\text{-}28)$$

$$E_d^2 = \frac{M_{-1}^2}{M_{-3}} \quad (2\text{-}29)$$

The obtained values are given formula the M_{-1} and M_{-3} moments changed due to the formation coordination Wimple-DiDomenico.

Chapter Three

Experimental Work

3.1 Introduction

This chapter emphasizes the experimental details used in the fabrication and investigation of Cu_2O:CaF_2 thin films by using the thermal evaporation technique. The techniques used for preparation and testing structural and morphological features by X-ray diffraction (XRD), field emission scanning electron microscope (FE-SEM), and atomic force microscope (AFM) respectively. Also, can be study the optical properties. The schematic diagram of the experimental work starting from material up to film characterization is displayed in Figure (3.1).

3.2 Nanomaterials at the Experiment

1- Copper Oxides (Cu_2O):

It was observed as a powder from Zhengzhou dongyao nano materials Co. LTD china company, with a nano grain size of 50 nm, density of 6.31 g/cm^3, color black to brown, and high purity (99.99 %).

2- Calcium Fluoride (CaF_2)

It was observed as a powder from Vardaan House Daryaganj, New Delhi-110002 (India), with nano grain size 30 nm, high purity (99.99 %), the color white solid, and a density of 3.18 g/cm^3.

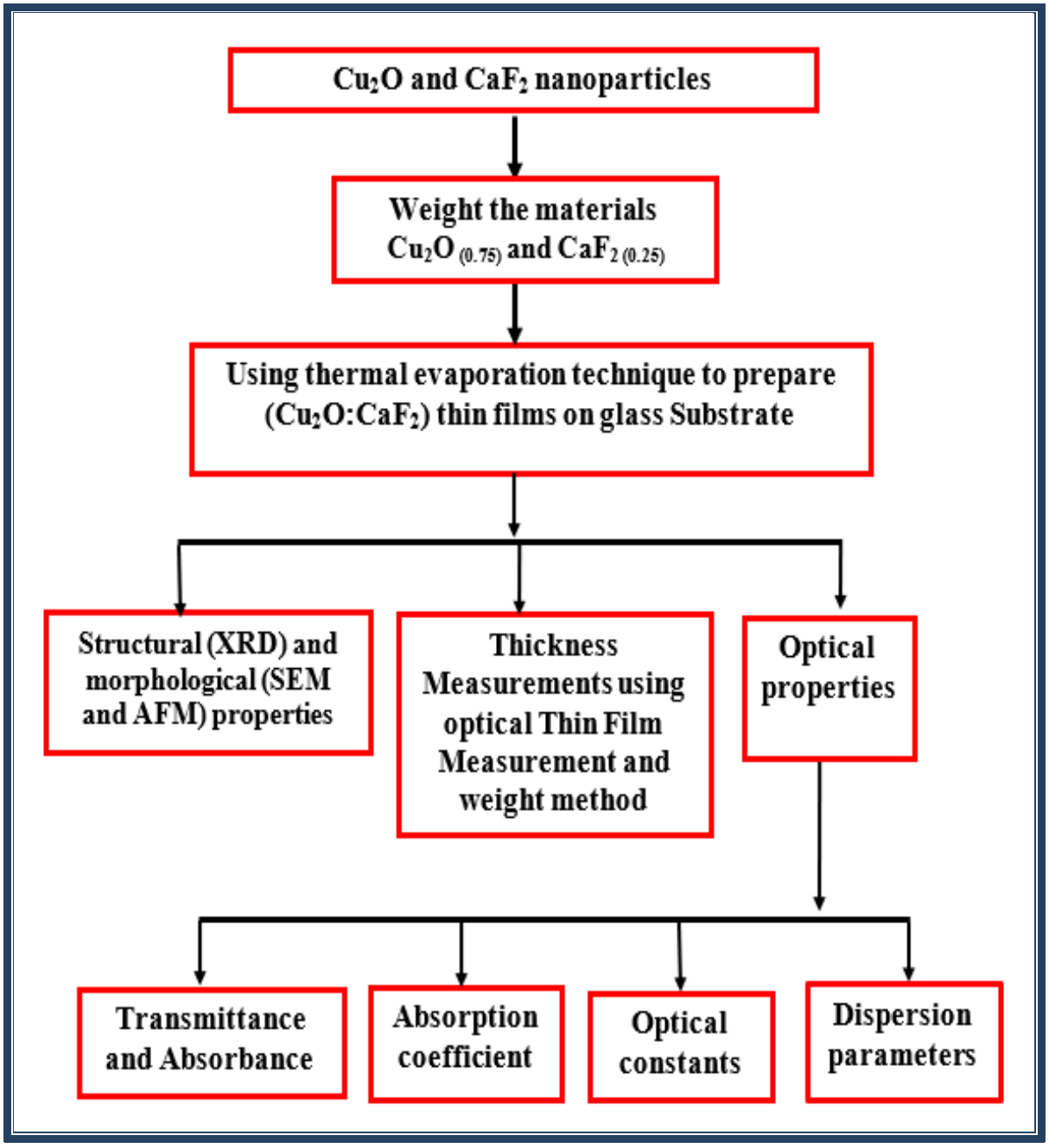

Fig. (3.1) Schematic Diagram of Experimental Work.

3.3 Substrate Preparation

The glass slides each of (2.54 × 7.62) cm^2 area was used as substrates with thickness 0.1-0.12 cm. These glass slides were subjected to the following steps:

1- The substrates were cleaned with alcohol.

2- The substrates were immersed in a clean beaker containing distilled water, and then washed ultrasonically for 10 min.

3- Lastly, the glass substrates were dried by an air-jet and rubbed with soft paper.

3.4 Evaporation Boat

The most commonly used materials for evaporation boats are metals with a high melting point, such as tungsten (W) (M.P = 3370 ^oC), and molybdenum (Mo) (M.P = 2622 ^oC). In this work, boats were used for evaporation; a molybdenum boat is used for the deposition of Cu_2O:CaF_2 nano films, as shown in Figure (3.2).

Fig (3.2) Molybdenum Evaporation Boat.

3.5 The Coating Unit

The vacuum unit system is:

1 Edwards Auto 306 that modified its chamber.
2 Uses tungsten or Molybdenum filaments to heat evaporates.
3 Ultimate chamber pressure 1×10^{-7} mbar.
4 Typical filament currents are 100-200 A.
5 Maximum deposition thickness that can be achieved is 1.5 μm.

The main constructions of the typical vacuum coating unit are shown in Figure. (3.3). This calculation was carried out Department of Physics, University of Babylon/College of Education for Pure Sciences.

Fig (3.3) Thermal Evaporation System.

3.6 Thin Film Growth

In the present work, thin films of Cu_2O:CaF_2 have been obtained by the additive 75% of Cu_2O (powder, purity 99.99%) and 25% CaF_2 (powder, purity 99.99%). The deposition of Cu_2O:CaF_2 thin films have been performed by electrical resistance heated thermal evaporation process. In this process, the electrical power is passed through the boat to create a vapor that travels in straight-line paths to the substrate. In general, there are three steps in any vacuum deposition process; creation of an evaporant from the source material; transport of the evaporant from the source to the substrate; and condensation of the evaporant onto the substrate to form the thin film deposited as in Figure (3.4). In this work, the evaporation processes have been performed at room temperature (R.T). The pressure during the evaporation was approximated to 10^{-7} mbar with a rate of deposition of 0.5 nm. s^{-1}. The distance between the source and substrate was kept at 15 cm.

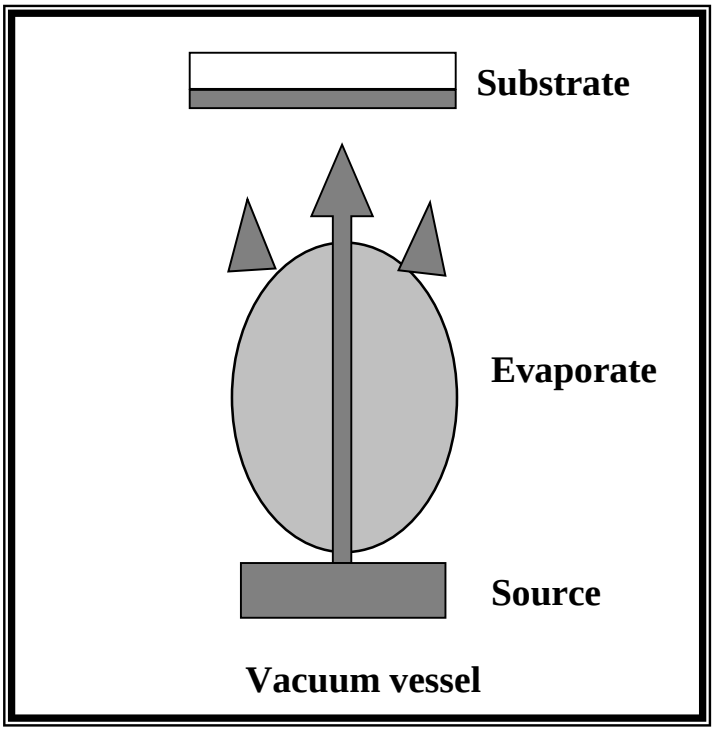

Fig. (3.4) Basic Steps Deposition Processes.

3.7 Films Thickness Measurement

Thickness is one of the most important thin film parameters. There are several methods used for measuring the thickness of thin film. In this work, the thickness of the films was measured by using the optical measurement and weight method.

3.7.1 Optical measurement methods

Film thickness measurements by optical thin film measurement have been obtained. This method is based on interference of the light beam reflected from the thin film surface and substrate bottom. He-Ne laser (632 nm) was used and the thickness was determined by the difference in optical path lengths of the two reflections, as shown in Figure (3.5). This calculation was carried out Department of Physics, University of Babylon/College of Education for Pure Sciences.

Fig. (3.5) Optical Thin Film Measurement.

3.7.2 The weight method

The thickness of the thin films has been calculated according to the following equation [1]:

$$t = \frac{m}{2\pi\rho R^2} \quad \text{.....} \quad (3\text{-}1)$$

where t is the thickness of the thin films (nm), m mass of the materials in (g), ρ is the density of materials (g/cm^3), and R is the distance between the substrate and the boat (cm). This method gives an approximate thickness because not all the material is deposited on the substrate but some of the material is lost or fleeing on the sides of the heater.

3.8 Structural and Morphological Measurements

3.8.1 X-ray diffraction (XRD)

The main purpose of these measurements is to investigate the type of structure of the prepared thin films. This experimental technique has long been used to determine the overall structure of bulk solids, including lattice constants, identification of unknown materials, the orientation of single crystals, the orientation of polycrystals, defects, stresses, etc. X-ray diffraction using SHIMADZU X-ray diffracts meter system (XRD-6000) which records the intensity as a function of Bragg's angle. The conditions of the system were:

Source CuK_α with radiation of wavelength λ = 1.5406 Å. Target Cu, Current = 30 mA, Voltage = 40 kV, Scanning speed = 0.25 deg/min, and the X-ray scans are performed between 2θ values of 5° and 80° as shown in Figure (3.6). This calculation was carried out Iran at University of Tahran.

Fig (3.6) The System of the XRD.

3.8.2 Field Emission Scanning Electron Microscope (FE-SEM)

FE-SEM is an electron microscope that images the sample surface with a high-energy beam of electrons in a raster scan pattern. After the preparation of the sample, the part of each sample with dimensions (5 mm × 10 mm) was cut and pleased into the FE-SEM sample holder for examination. The surface morphology of Cu_2O:CaF_2 is observed using (INSPECT S50, company, Japan origin, type FEI customer ownership FE-SEM), as shown in Fig (3.7). This calculation was carried out of Iran at University of Tahran.

Fig.(3.7) Diagram of a System of FE-SEM Device.

3.8.3 Atomic Force Microscope (AFM)

The atomic force microscope (AFM) enables you to have a look at surfaces on a molecular level. Instead of only pictures real topography data are collected. AFM determines the size and other characteristics of the synthesized nanoparticles, and an atomic force microscope (AFM) is used. The operation principle of an AFM is presented in Figure (3.8). All the samples are studied using a nasoscope AFM. This calculation was carried out Department of Physics, University of Babylon/College of Education for Pure Sciences.

Fig (3.8) The System of AFM.

3.9 Optical Measurement

The optical measurements of Cu_2O:CaF_2 thin films are obtained by using a spectrophotometer (Shimadzu UV- 1650 PC) made by Phillips, (Japanese company), as shown in Figure (3.9), for the wavelength range from 200 to 1100 nm. The optical properties are calculated from these optical measurements. This calculation was carried out Department of Physics, University of Babylon/College of Education for Pure Sciences.

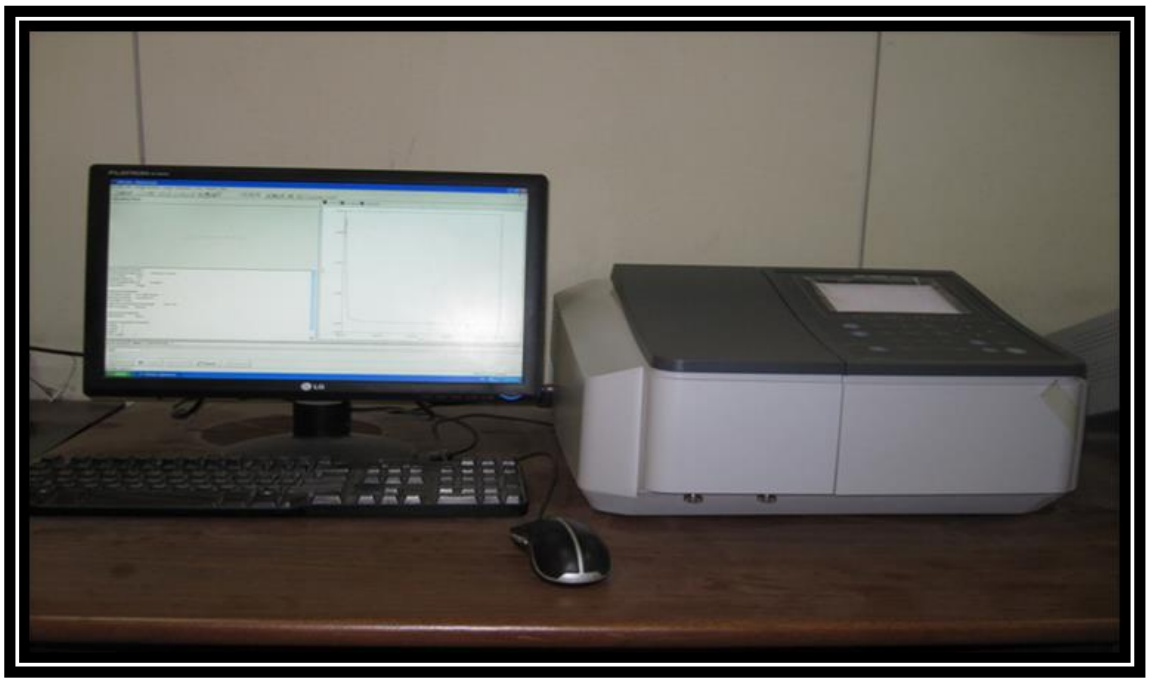

Fig.(3.9) The Photographic of UV-VIS-NIR Spectrophotometer.

Chapter Four

Results and Discussion

4.1 Introduction

This chapter presents the results and discussion of the structural, morphological, and optical properties of $Cu_2O_{(0.75)}CaF_{2(0.25)}$ films, the dispersion parameters were also investigated using the Wemple-Didominco model. The samples were diagnosed by XRD, FE-SEM, AFM, and UV-Visible spectrophotometer.

4.2 The Structural and Morphological Properties

Structural and morphological properties include the X-ray Diffraction (XRD), Field Emission Scanning Electron Microscope (FESEM), and Atomic Force Microscope (AFM).

4.2.1 X-ray Diffraction (XRD)

To investigate the structural nature of $Cu_2O_{(0.75)}$:$CaF_{2(0.25)}$ films, the X-ray diffraction was recorded between 5º-80º. The XRD spectra of Cu_2O:CaF_2 thin films with different thicknesses prepared by thermal evaporation technique at R.T under pressure up to 1×10^{-7} mbar with a rate of deposition 0.5 nm/sec^{-1} onto a glass substrate.

The XRD pattern of $Cu_2O_{(0.75)}$:$CaF_{2(0.25)}$ thin films is shown in Fig (4.1). From the figure, no sharp peaks were noticed in the prepared indicating that the crystallization of the nanofilm is poor. Only two broad peaks were determined (no predominant peak) at 2θ = 7º and 25º. The Cu_2O diffraction peak is readily indexed to face centered cubic Cu_2O (JCPDS 05–0667, a = 0.470 nm) at 2θ = 24º-25º [88]. In this work, the deposited Cu_2O: CaF_2 nanofilms for eight specimens as shown in figure whose peaks observed at 2θ ranged between (22.5-25.76) accordance with the plane (111) of the cubic structure attributed to the CaF_2 NPs.[89], while the peak at corresponding to the 2θ = 7º may be attributed to the interaction between Cu_2O NPs and CaF_2 NPs and Thus, it will lead to a phase mutation, and therefore these peaks cannot be obtained by Miller indices.

The crystallite size (D) was calculated from Scherer's formula (2-2). It can be noted that the average crystalline size increased from 4.88 nm at a thickness of 16 nm to 14.71 nm at a thickness of 57 nm. The values of crystallite size and FWHM are tabulated in Table (4.1). The high values of the FWHM refer to the small crystallite size. Similar behaviour was reported in [50,90,91].

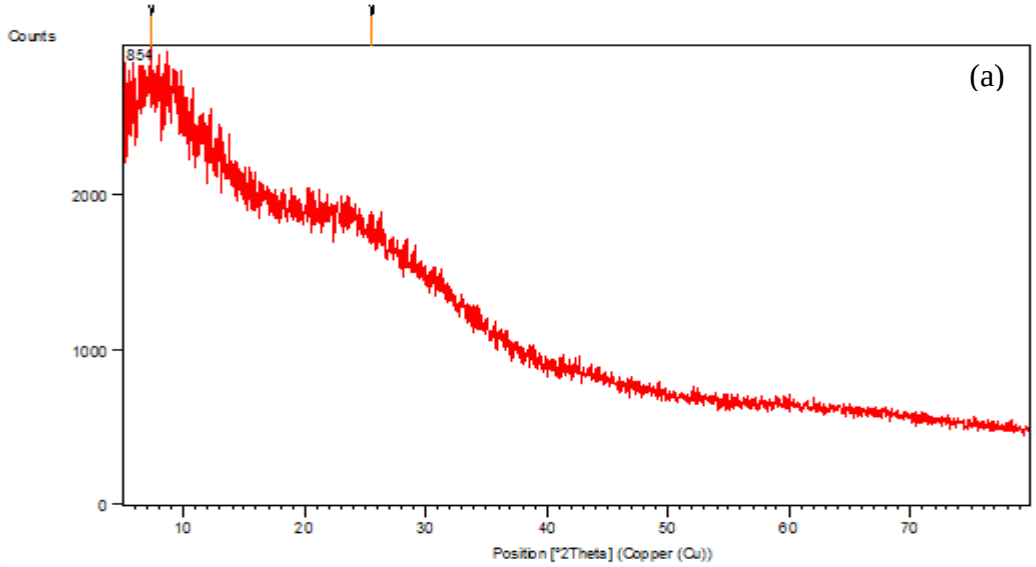

Pe

Pos.[°2Th.]	Height [cts]	FWHMLeft[°2Th.]	d-spacing [Å]	Rel. Int. [%]
7.330159	220.086400	7.800000	12.05021	100.00
25.573690	189.642700	9.767052	3.48040	86.17

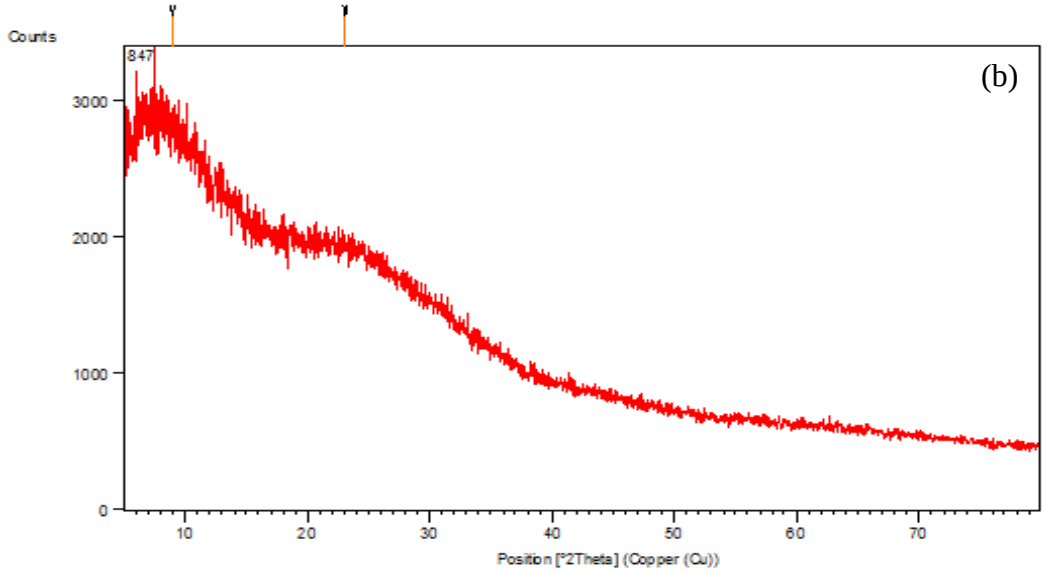

Peak List

Pos.[°2Th.]	Height [cts]	FWHMLeft[°2Th.]	d-spacing [Å]	Rel. Int. [%]
8.920118	223.056600	5.148542	9.90558	100.00
23.087950	87.741850	5.352899	3.84919	39.34

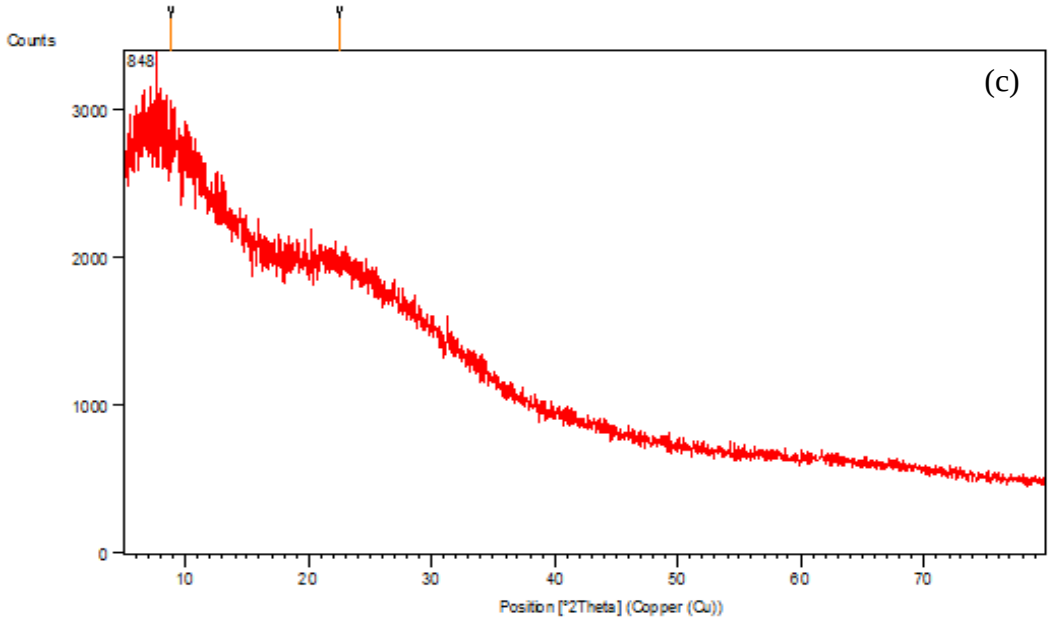

Peak List

Pos.[°2Th.]	Height [cts]	FWHMLeft[°2Th.]	d-spacing [Å]	Rel. Int. [%]
8.841324	208.269500	3.866215	9.99368	100.00
22.503760	77.118740	4.804810	3.94777	37.03

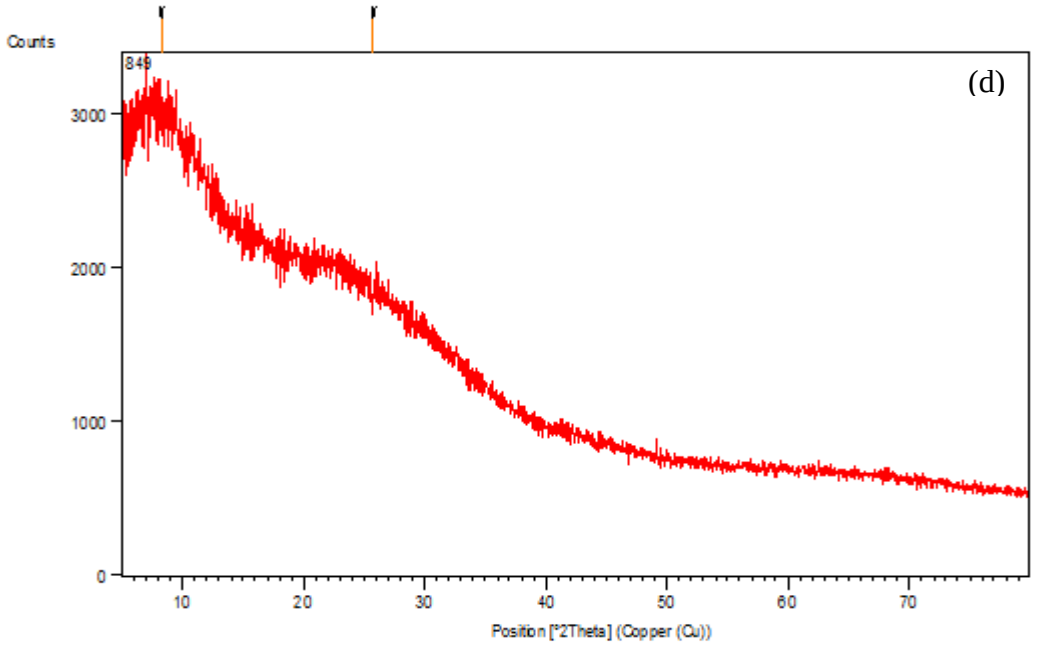

Peak List

Pos.[°2Th.]	Height [cts]	FWHMLeft[°2Th.]	d-spacing [Å]	Rel. Int. [%]
8.269289	255.543700	11.252800	10.68368	100.00
25.762020	195.512800	10.757820	3.45539	76.51

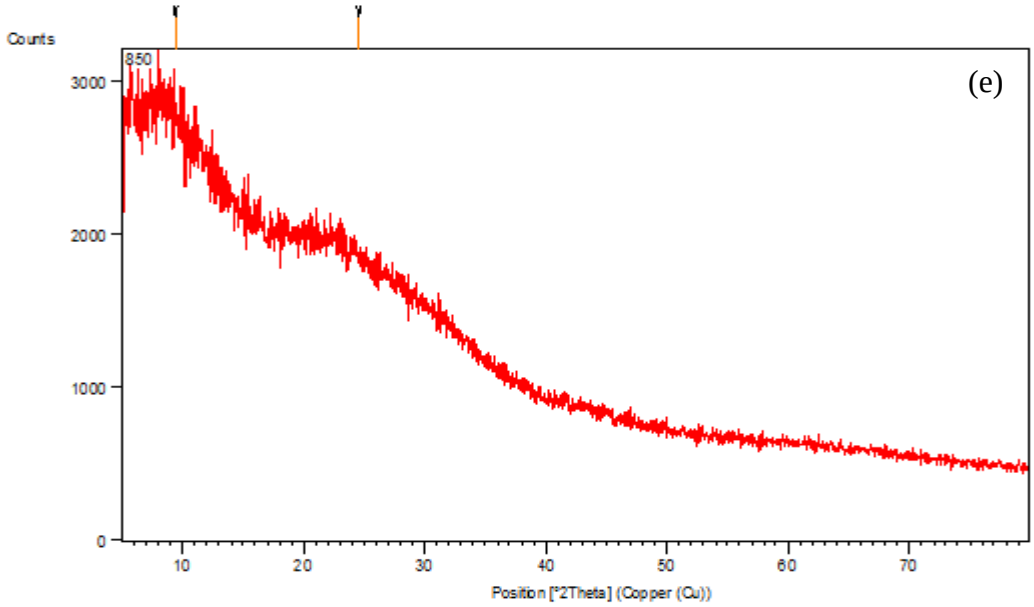

Peak List

Pos.[°2Th.]	Height [cts]	FWHMLeft[°2Th.]	d-spacing [Å]	Rel. Int. [%]
9.373566	178.045100	10.254400	9.42739	100.00
24.527070	142.331600	9.120786	3.62650	79.94

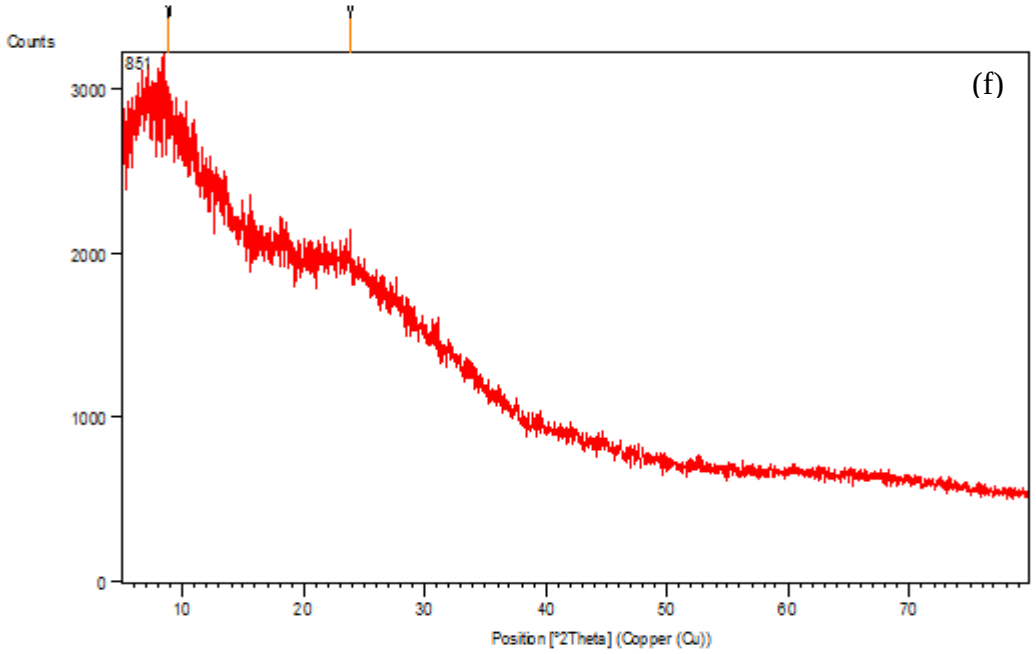

Peak List

Pos.[°2Th.]	Height [cts]	FWHMLeft[°2Th.]	d-spacing [Å]	Rel. Int. [%]
8.878424	293.833300	6.423650	9.95201	100.00
23.833500	129.547400	5.329407	3.73044	44.09

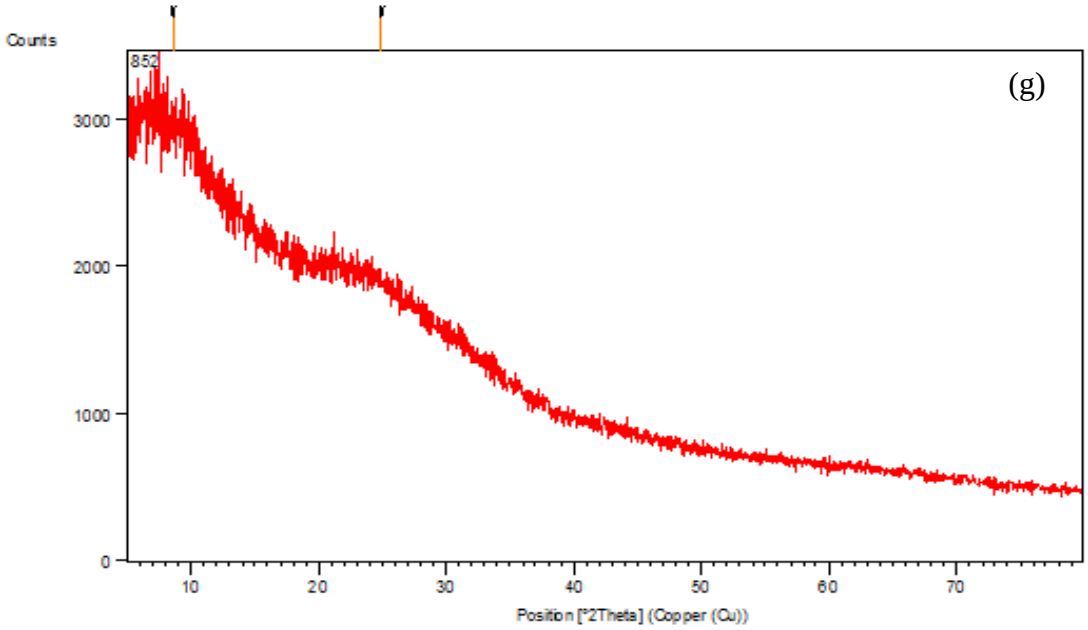

Peak List

Pos.[°2Th.]	Height [cts]	FWHMLeft[°2Th.]	d-spacing [Å]	Rel. Int. [%]
8.547926	186.548400	10.620500	10.33604	100.00
24.950110	177.869100	7.667309	3.56596	95.35

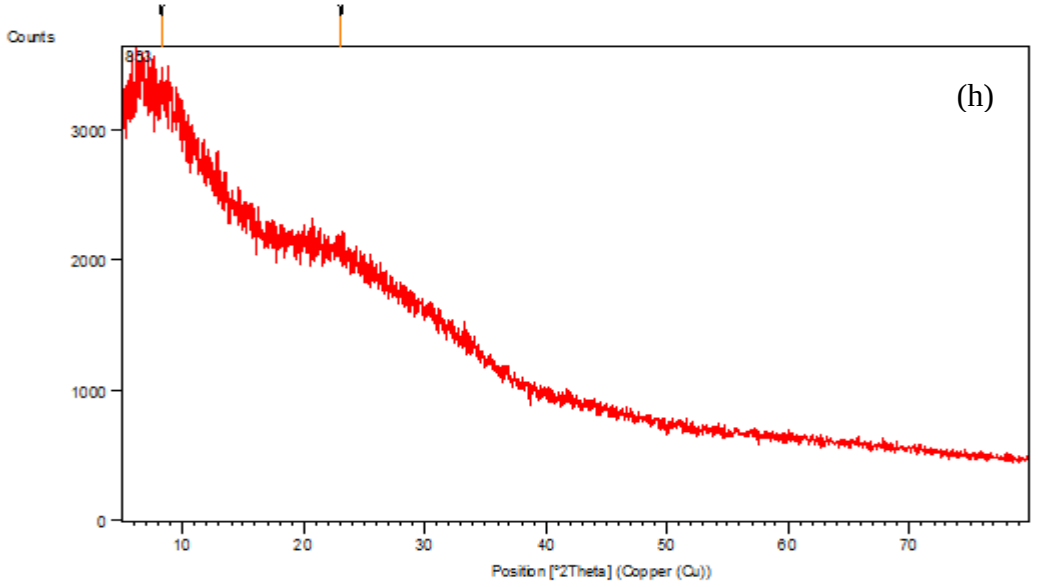

Peak List

Pos.[°2Th.]	Height [cts]	FWHMLeft[°2Th.]	d-spacing [Å]	Rel. Int. [%]
8.274397	239.157300	5.859873	10.67709	100.00
23.095710	133.518300	5.546782	3.84791	55.83

Fig (4.1) The XRD Spectra of $Cu_2O:CaF_2$ Thin Films with Different Thicknesses (a) 16 nm, (b) 19 nm, (c) 22 nm, (d) 29 nm, (e) 35 nm, (f) 42 nm, (g) 50 nm, (h) 57 nm.

Table (4.1) The Results of the XRD Data of $Cu_2O:CaF_2$ Thin Films at Different Thicknesses.

Thickness (nm)	2Ɵ (degree)	hkl	FWHM (degree)	Crystallite size (nm)	Average crystallite size (nm)
16	7.33		7.8	1.06	4.88
	25.57	(111)	9.76	8.7	
19	8.92		5.148	1.61	1.595
	23.087	(111)	5.352	1.58	
22	8.84		3.866	2.15	1.935
	22.5	(111)	4.904	1.72	
29	8.26		11.25	7.3	7.6
	25.76	(111)	10.75	7.9	
35	9.37		10.25	8.1	8.7
	24.52	(111)	9.12	9.3	
42	8.87		6.42	12.9	14.4
	23.83	(111)	5.32	15.9	
50	8.54		10.62	7.8	9.4
	24.95	(111)	7.66	11.0	
57	8.27		5.85	14.22	14.71
	23.09	(111)	5.54	15.2	

4.2.2 Atomic Force Microscope (AFM)

The AFM images of $Cu_2O:CaF_2$ thin film with different thicknesses prepared by the thermal evaporation technique are shown in Figures. (4.2-4.9).

Images in part (a) and (b) for all these figures reveal to the two and three dimensions respectively. From this images that the $Cu_2O:CaF_2$ thin film show a high surface homogeneity in which the distribution of crystalline granules is uniform which is evident from the convergence of the roughness and root mean square (RMS). The white areas of the images indicate that there are a set of crystalline granules one on top other, so it can be believed that the adjacent granules come together to form large clusters; therefore, we find that the granules in the white areas are larger than that in other regions. The roughness and root mean square (RMS) values are increased from 0.24 nm and 0.30 nm for the thickness of 16 nm to 2.25 nm and 3.12 nm for the thickness of 57 nm, which is attributed to the fact that aggregate forms bigger grains at higher

thicknesses. Therefore, the surface morphology of thin film is strongly affected by the degree of aggregation. The increase in RMS leads to an increase in crystalline growth in a vertical direction more than a horizontal direction.

Images in part (c) for all these figures obtain the grain histogram. From these images, it can be note that there is different in grain size distributed which that the grain size increased with increasing thickness that indicate to increasing concentration for Cu_2O and CaF_2 NPs.

Image in part (d) for all these figures illustrate the hight distribution of the grains inside the surface of thin films. From this image, its show that the white region reveals to the hight grain, while the black region reveals to the small region and that is different of grain size with increasing thickness that is corresponding to the images of two and three dimension in part (a) and (b) respectively.

Also, Table (4.2) contain the ten-point height and the average diameter, the average diameter increased with increasing thickness from 204 nm to 435.1 nm. Similar behaviour was reported in [92]. The small values of ten-point height refer to fine surfaces.

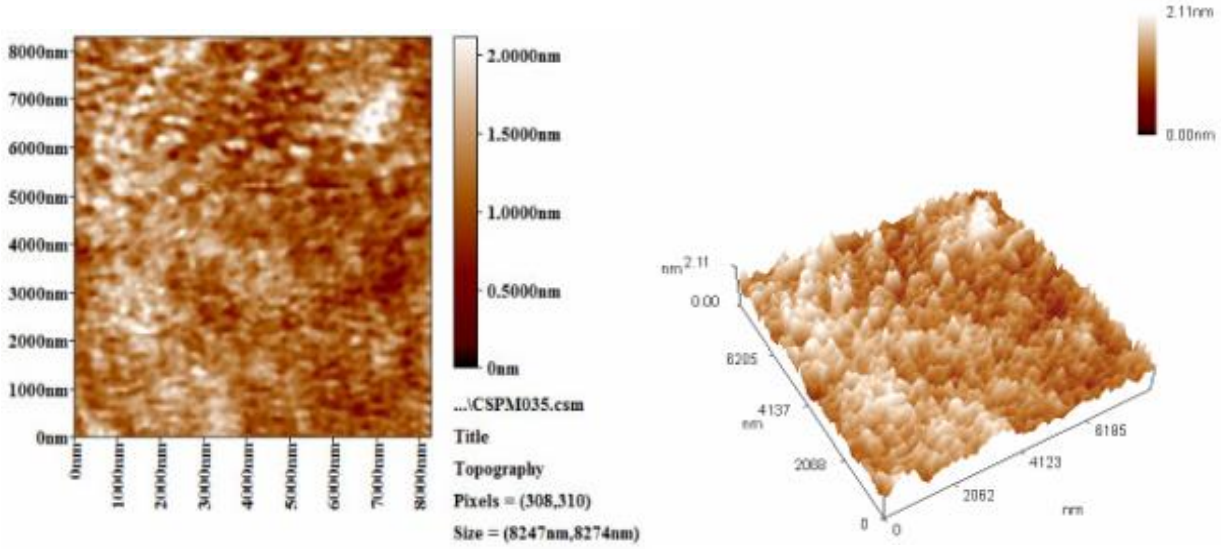

(a) (b)

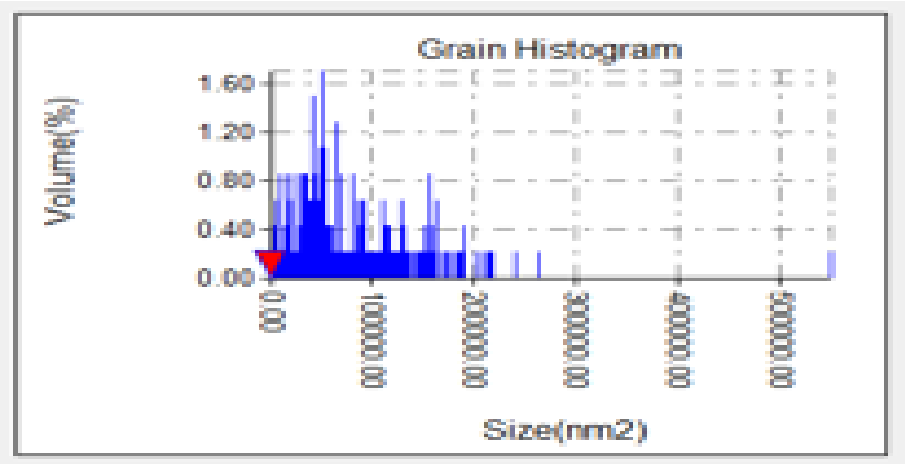

(c)

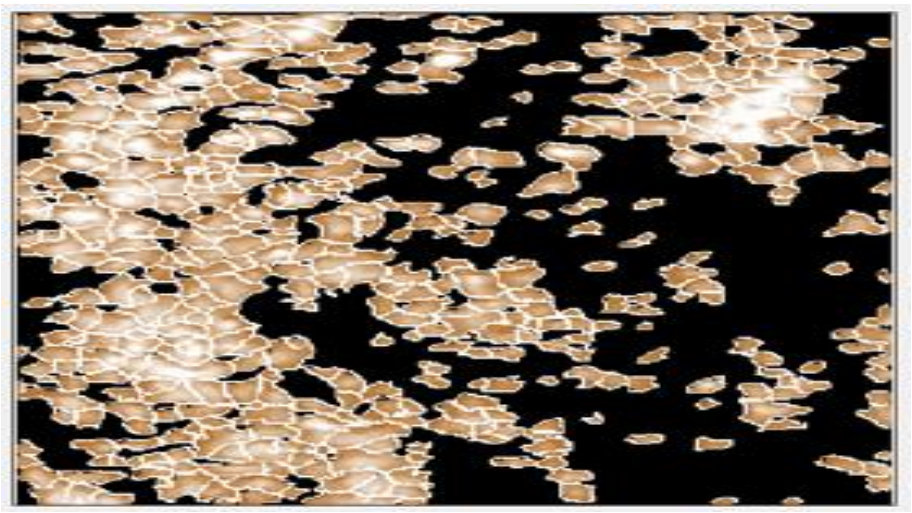

(d)

Fig (4.2). AFM Images of Cu_2O:CaF_2 Thin Films at Thickness 16 nm of a) 2D, b)3D, c) Grain Histogram, and d) Height Distribution.

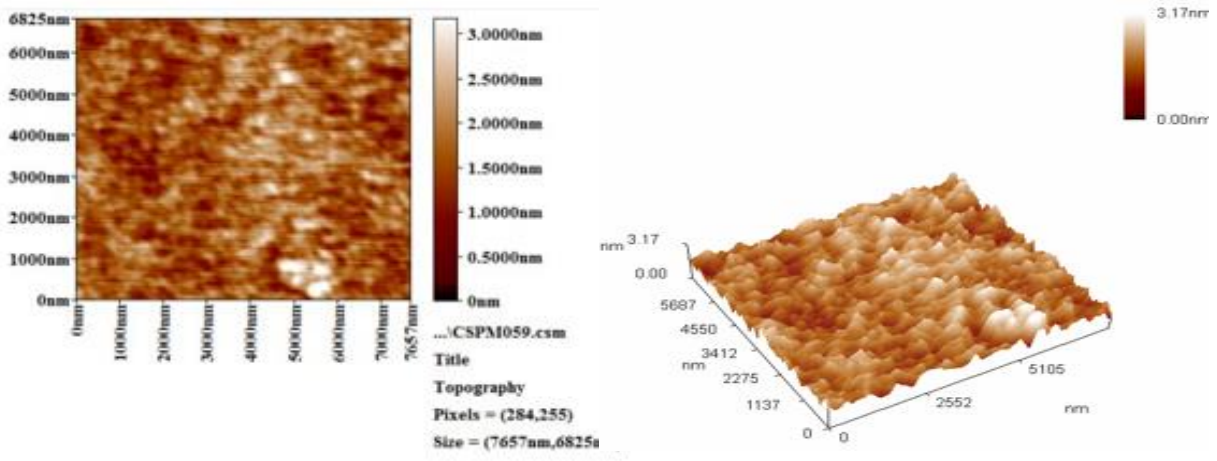

(a) (b)

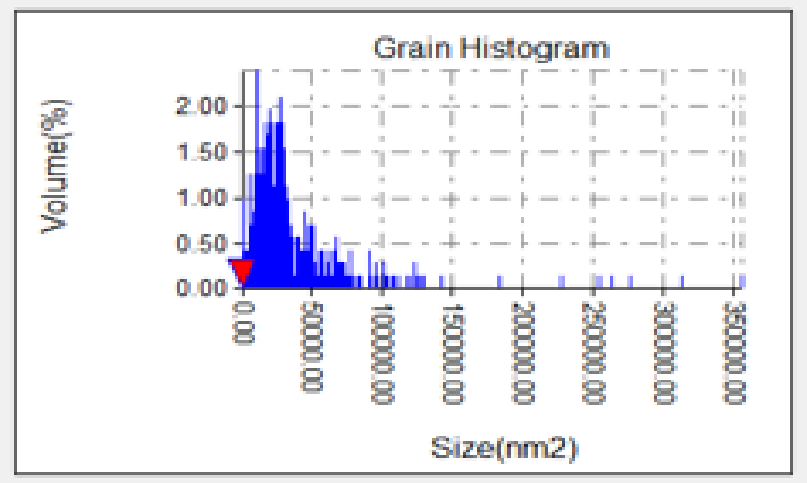

(c)

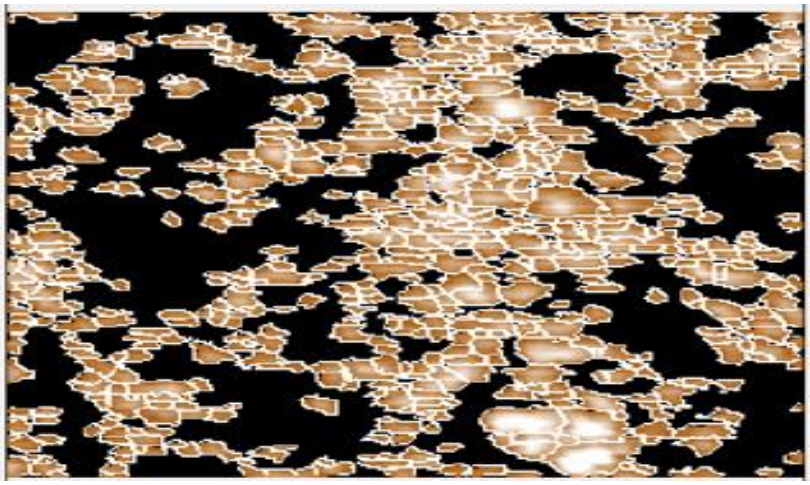

(d)

Fig (4.3). AFM Images of Cu_2O:CaF_2 Thin Films at Thickness 19 nm of a) 2D, b)3D, c) Grain Histogram, and d) Height Distribution.

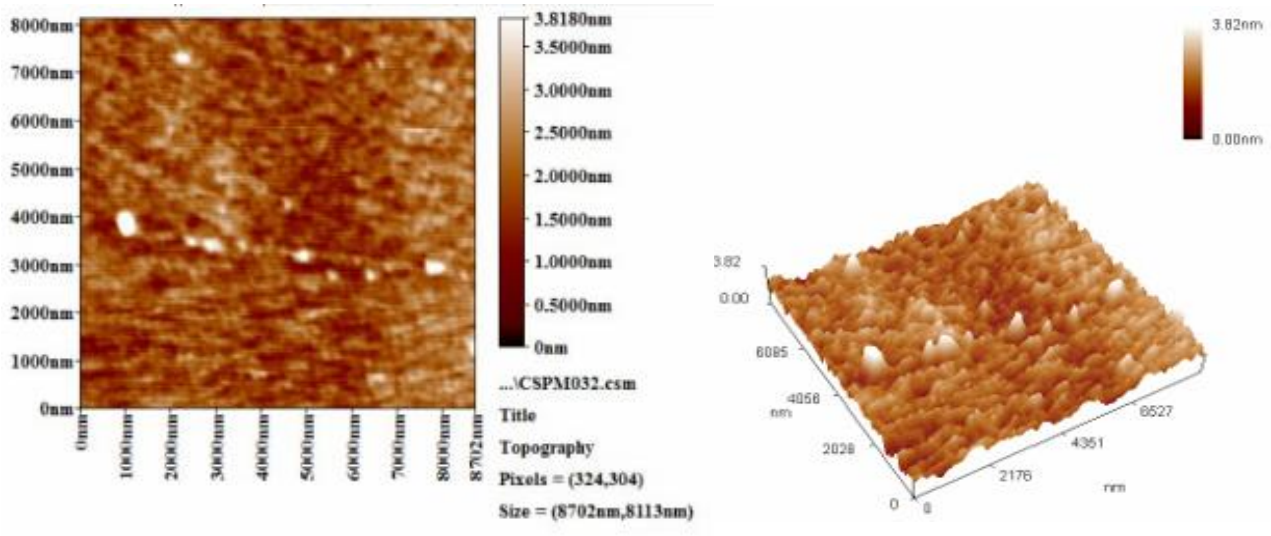

(a) (b)

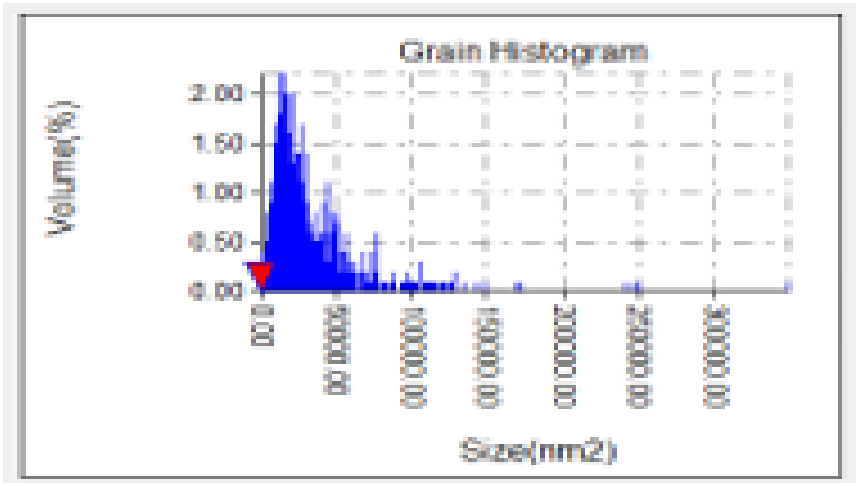

(c)

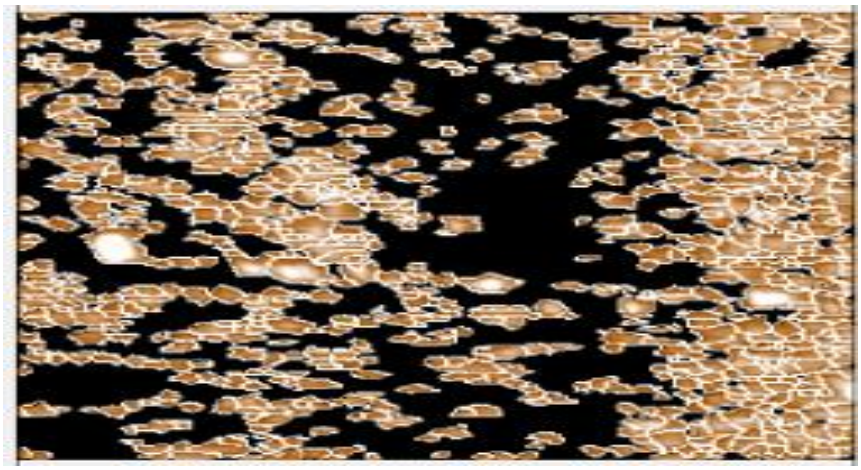

(d)

Fig (4.4). AFM Images of Cu_2O:CaF_2 Thin Films at Thickness 22 nm of a) 2D, b)3D, c) Grain Histogram, and d) Height Distribution.

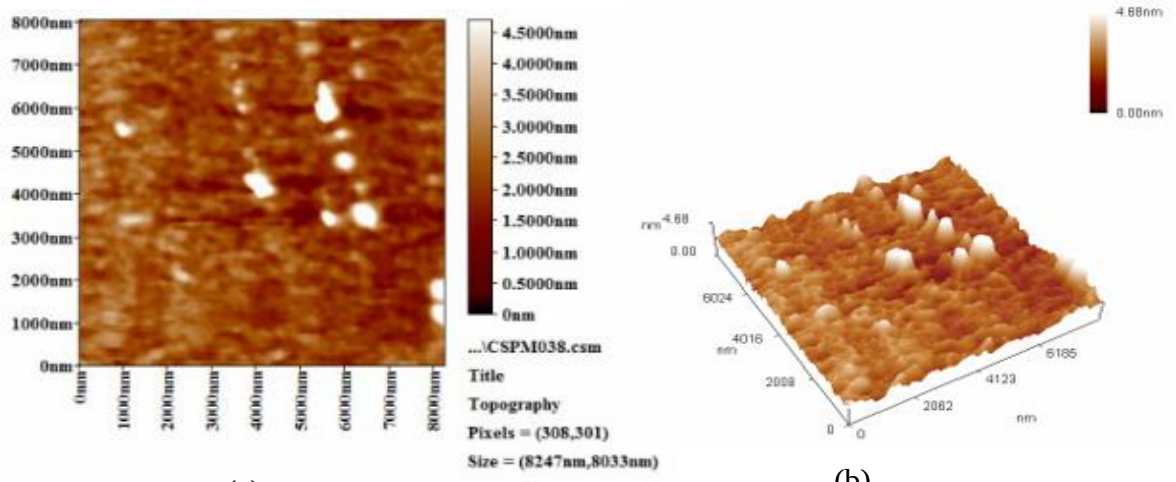

(a) (b)

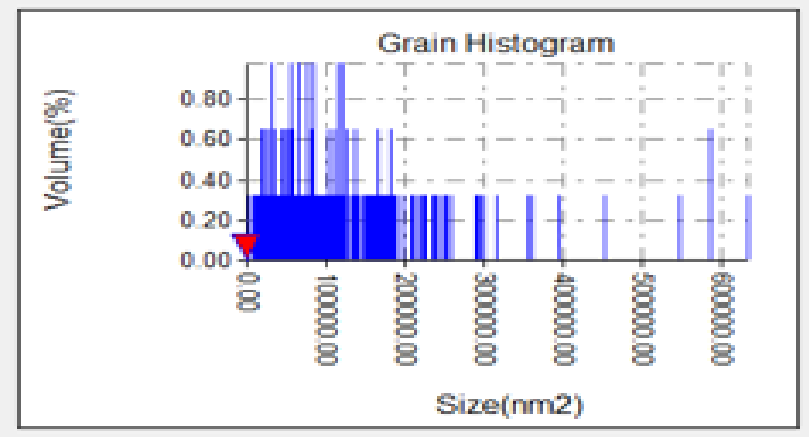

(c)

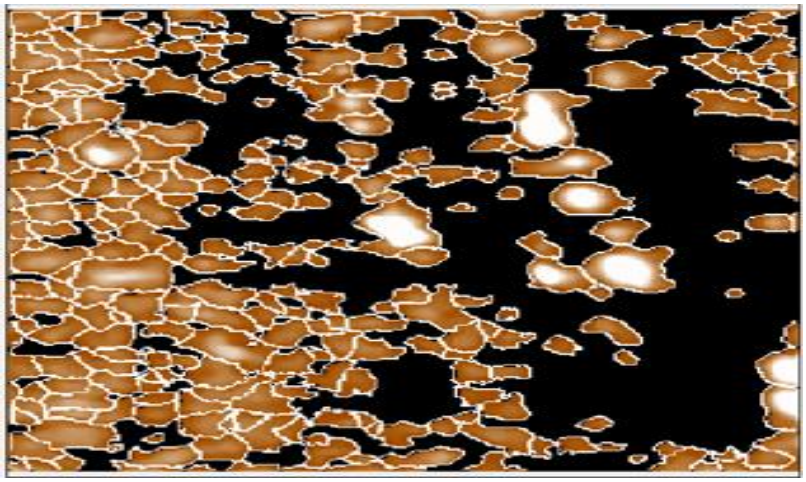

(d)

Fig (4.5). AFM Images of Cu_2O:CaF_2 Thin Films at Thickness 29 nm of a) 2D, b)3D, c) Grain Histogram, and d) Height Distribution.

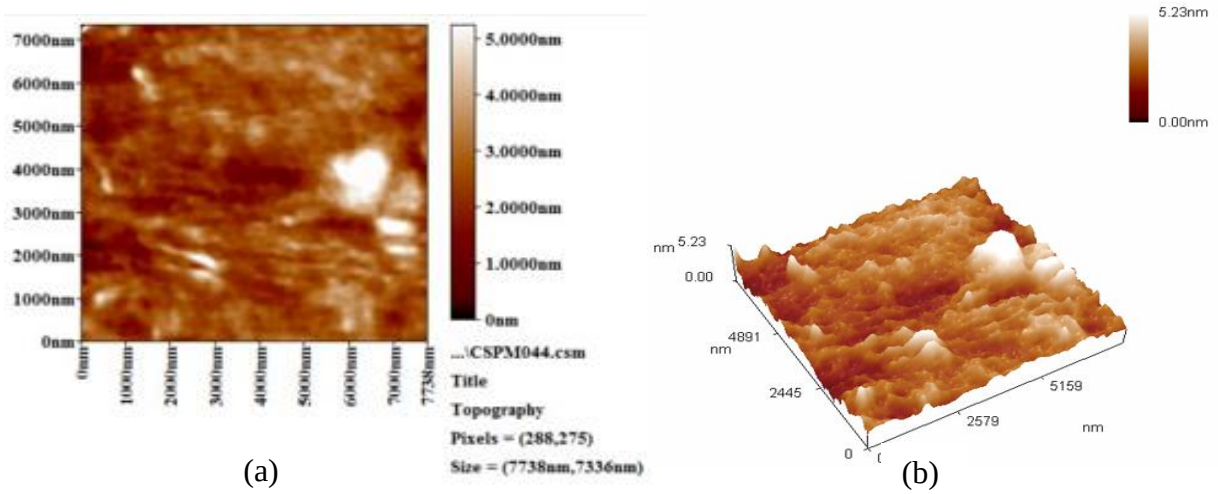

(a) (b)

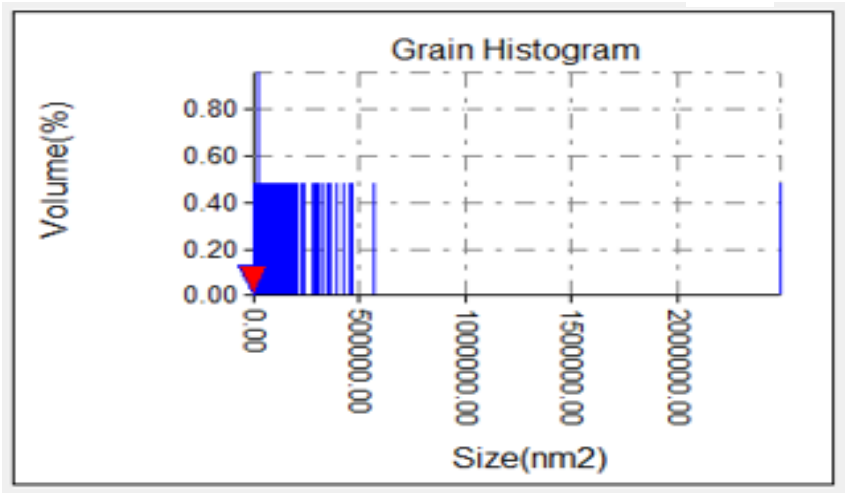

(c)

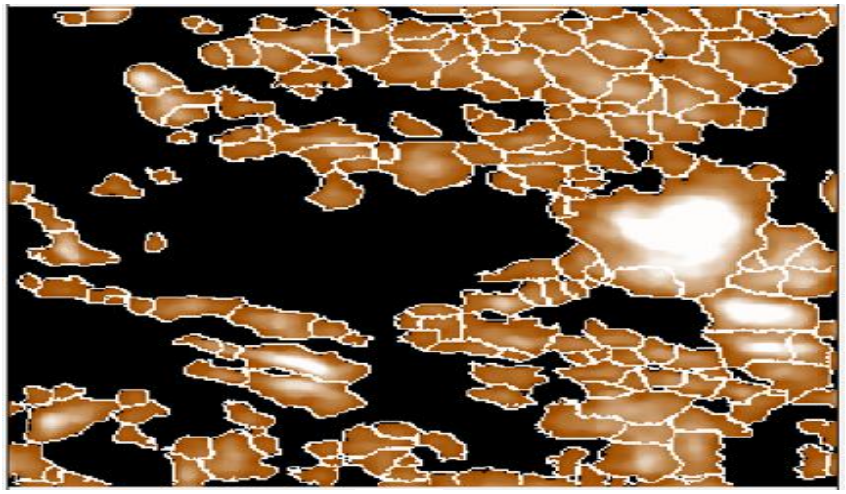

(d)

Fig (4.6). AFM Images of Cu_2O:CaF_2 Thin Films at Thickness 35 nm of a) 2D, b)3D, c) Grain Histogram, and d) Height Distribution.

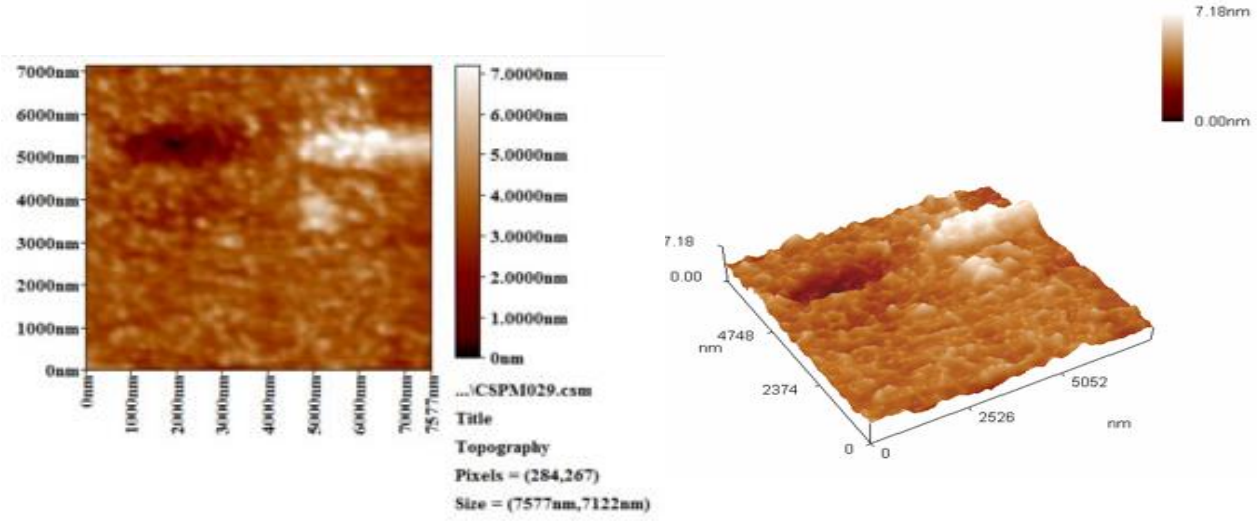

(a) (b)

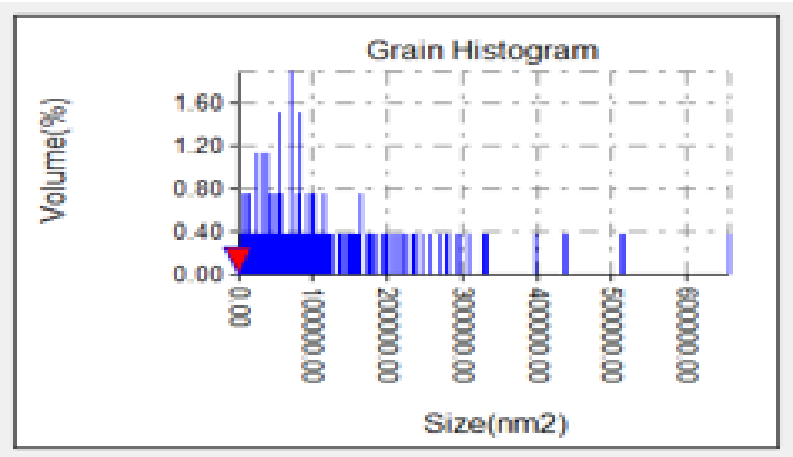

(c)

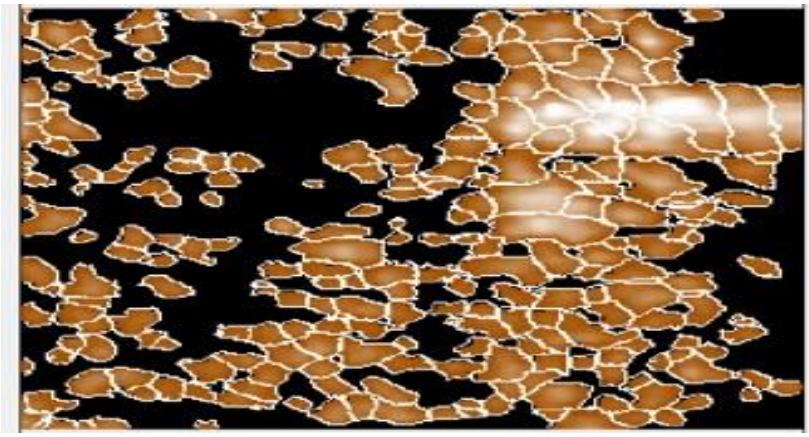

(d)

Fig (4.7). AFM Images of Cu_2O:CaF_2 Thin Films at Thickness 42 nm of a) 2D, b)3D, c) Grain Histogram, and d) Height Distribution.

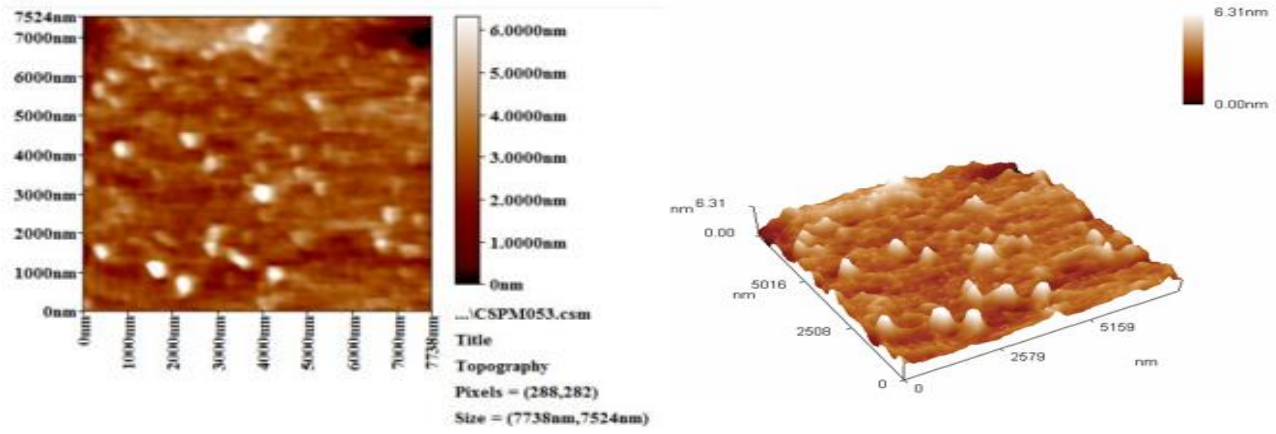

(a) (b)

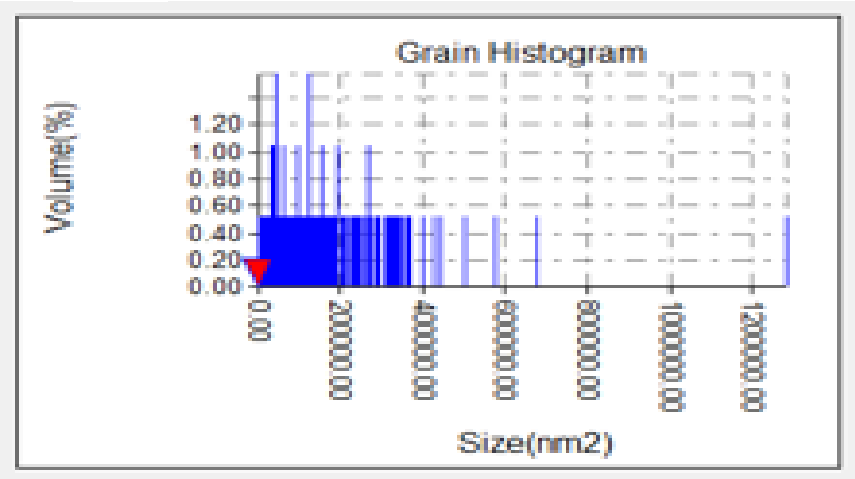

(c)

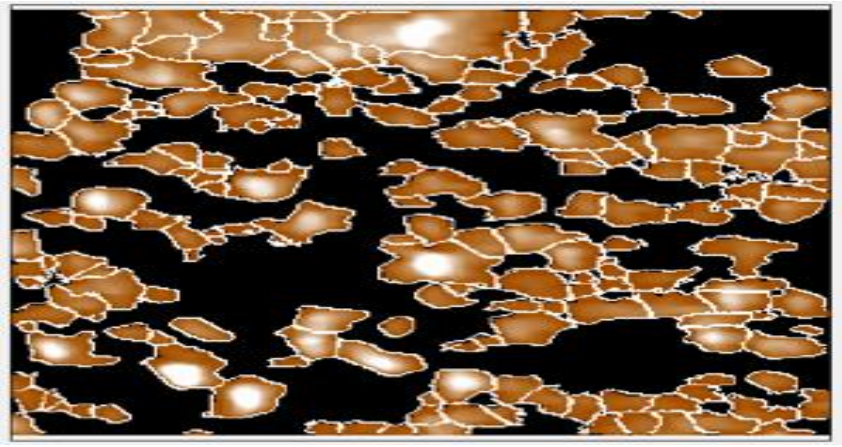

(d)

Fig (4.8). AFM Images of Cu_2O:CaF_2 Thin Films at Thickness 50 nm of a) 2D, b)3D, c) Grain Histogram, and d) Height Distribution.

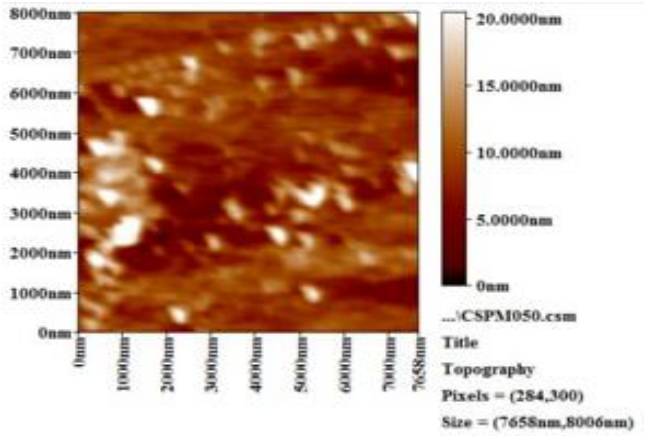

(a)

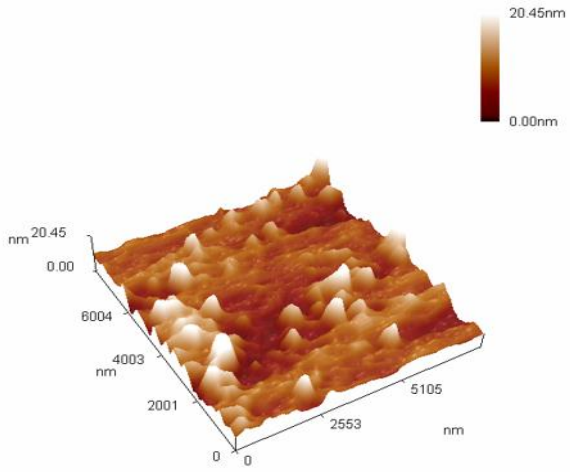

(b)

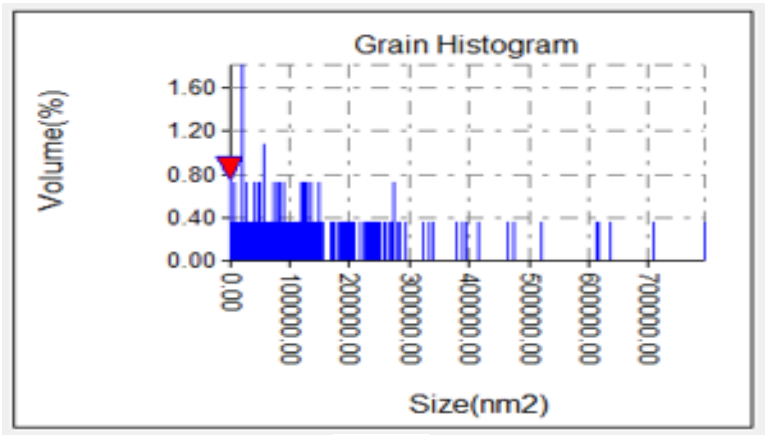

(c)

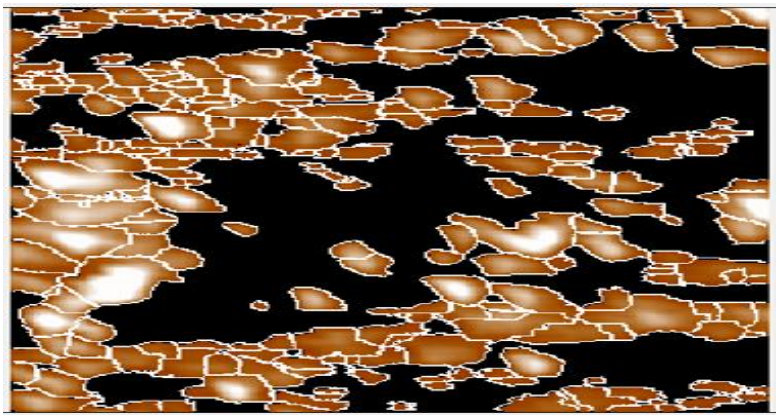

(d)

Fig (4.9). AFM Images of Cu_2O:CaF_2 Thin Films at Thickness 57 nm of a) 2D, b)3D, c) Grain Histogram, and d) Height Distribution.

Table (4.2) Morphological Characteristics of $Cu_2O:CaF_2$ Thin Film with Different Thicknesses.

Thickness (nm)	Roughness average (nm)	Root mean square (nm)	Ten-point height (nm)	Average diameter (nm)
16	0.24	0.30	1.81	204
19	0.32	0.41	2.93	210.1
22	0.34	0.44	2.69	293.3
29	0.41	0.57	3.21	362.8
35	0.55	0.75	3.59	367.1
42	0.56	0.83	5.49	372.3
50	0.57	0.81	4.21	412.4
57	2.25	3.12	18.8	435.1

4.2.3 Field Emission Scanning Electron Microscope (FE-SEM)

Field Emission Scanning Electron Microscope (FE-SEM) was used to investigate the surface morphology of samples and the dispersion of $Cu_2O:CaF_2$ nanoparticles on the surface as shown in Fig. (4.10) explain the FE-SEM images of $Cu_2O:CaF_2$ thin films with different thicknesses at magnification 50kx and scale 200 nm. From this figure, uniform morphology revealing a rather soft surface and with increase of the thickness led to changes in the morphology of the surface and increase the roughness therefore, the average particle size increased with increasing thickness, it is increased from 25.30 nm at thickness 16 nm to 75 nm at thickness 57 nm. The $Cu_2O:CaF_2$ thin films that were fine dispersion without aggregates with well-distributed and spread densely on the surface at low thickness, this may be indicating the occurrence of a homogeneous growth mechanism. At thickness (50 and 57) nm lead to aggregate and form clusters, which may be attributed to the interaction between Cu_2O and CaF_2 NPs. The results are consistent with AFM and the results of the previous researchers [47, 90,91].

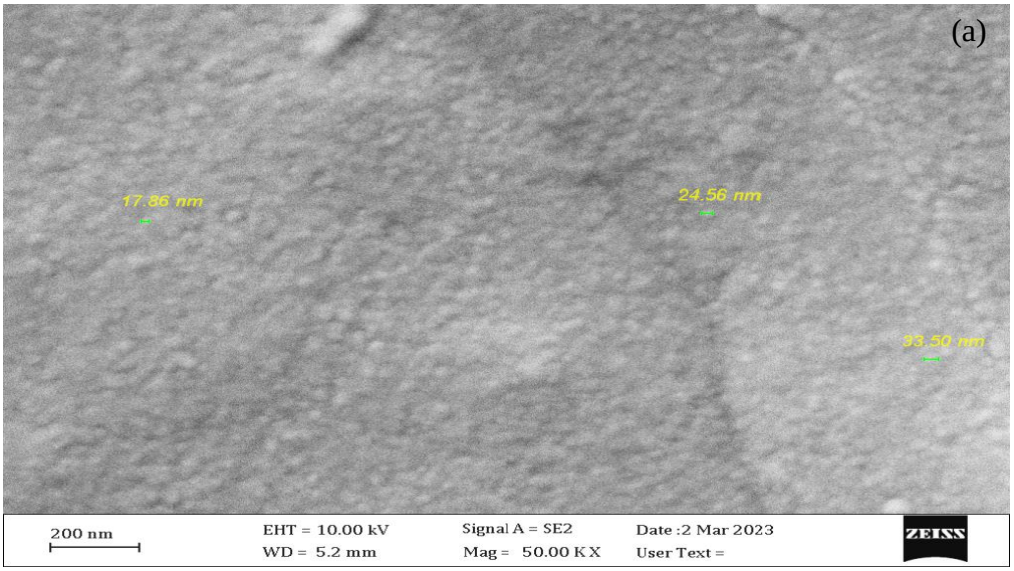
(a)
17.86 nm
24.56 nm
33.50 nm
200 nm
EHT = 10.00 kV
WD = 5.2 mm
Signal A = SE2
Mag = 50.00 K X
Date :2 Mar 2023
User Text =
ZEISS

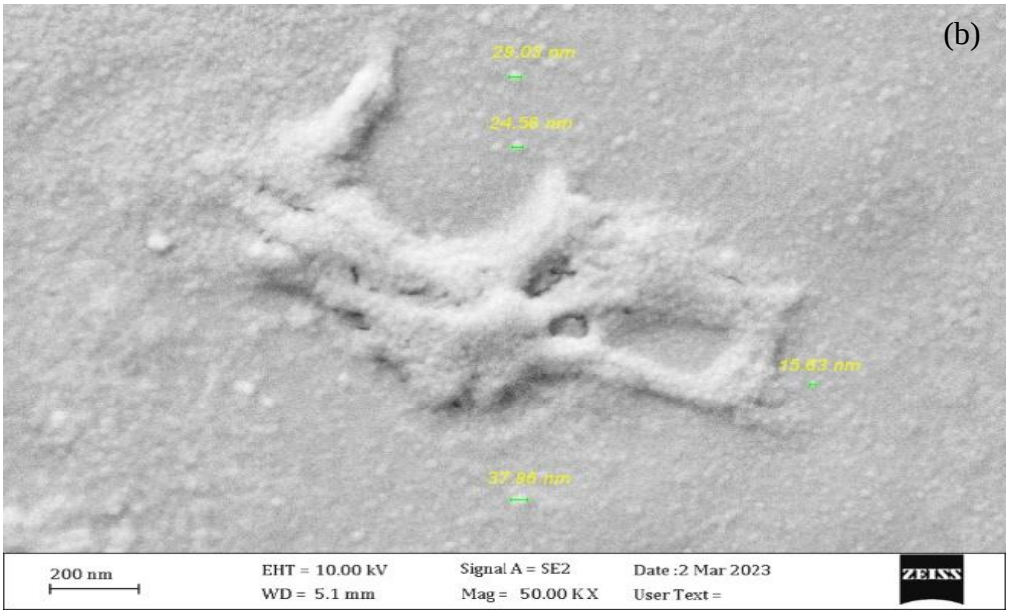
(b)
28.08 nm
24.58 nm
15.83 nm
37.86 nm
200 nm
EHT = 10.00 kV
WD = 5.1 mm
Signal A = SE2
Mag = 50.00 K X
Date :2 Mar 2023
User Text =
ZEISS

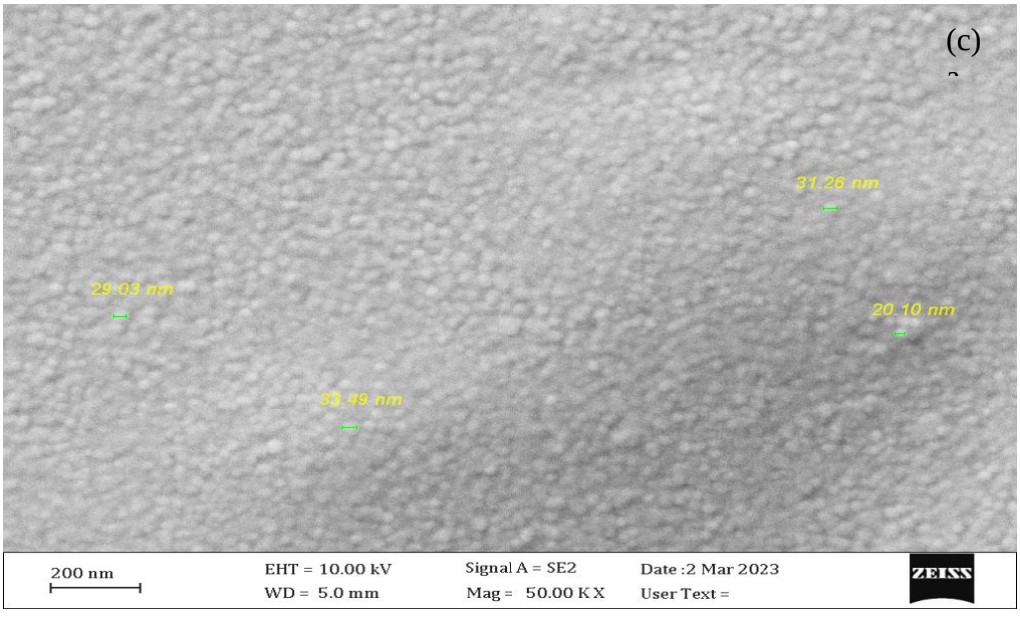
(c)
31.26 nm
29.03 nm
20.10 nm
33.49 nm
200 nm
EHT = 10.00 kV
WD = 5.0 mm
Signal A = SE2
Mag = 50.00 K X
Date :2 Mar 2023
User Text =
ZEISS

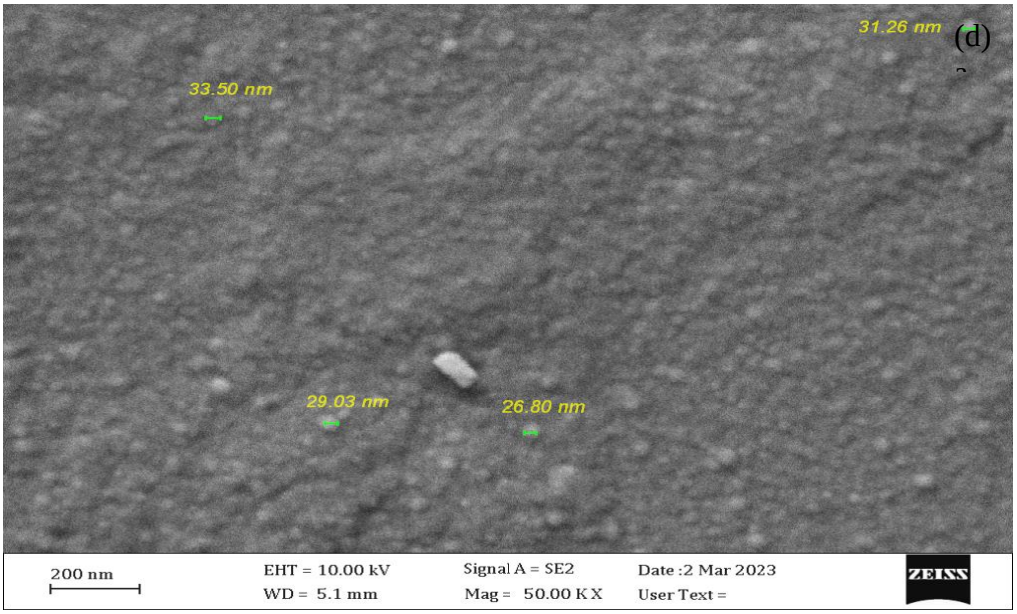
31.26 nm
(d)
33.50 nm
29.03 nm
26.80 nm
200 nm
EHT = 10.00 kV
WD = 5.1 mm
Signal A = SE2
Mag = 50.00 K X
Date :2 Mar 2023
User Text =
ZEISS

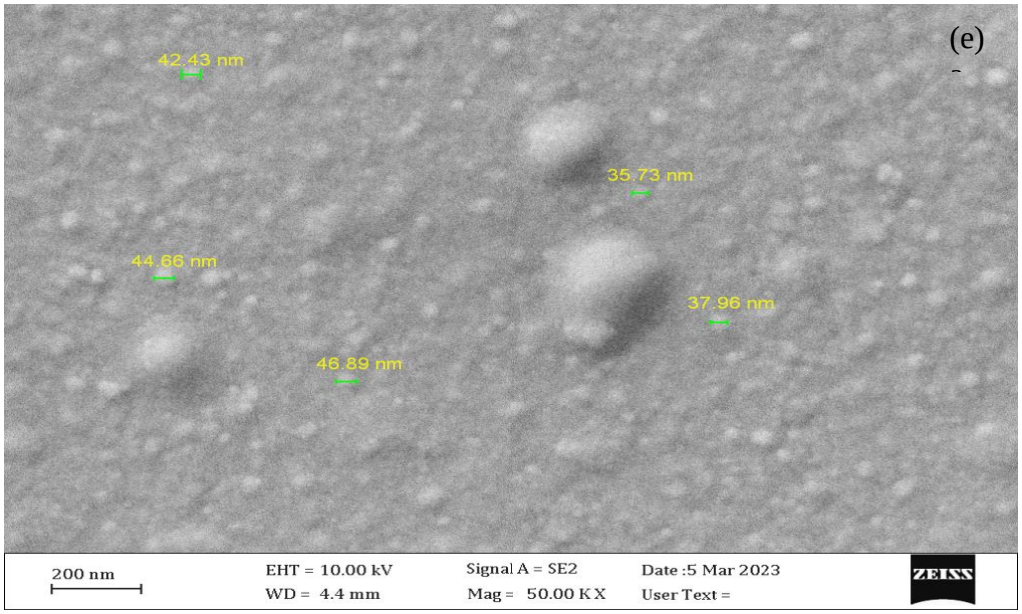
(e)
42.43 nm
35.73 nm
44.66 nm
37.96 nm
46.89 nm
200 nm
EHT = 10.00 kV
WD = 4.4 mm
Signal A = SE2
Mag = 50.00 K X
Date :5 Mar 2023
User Text =
ZEISS

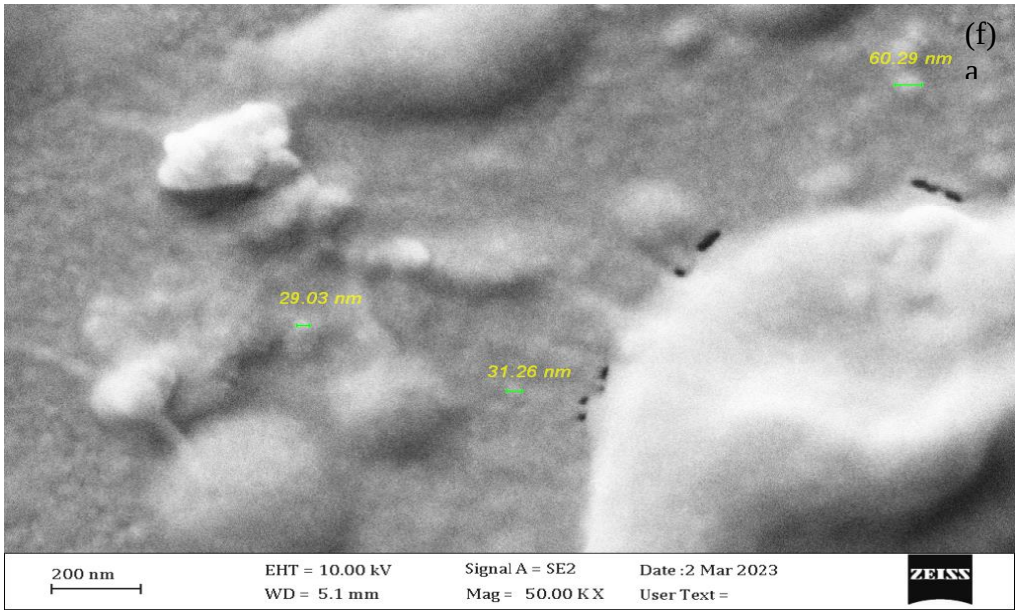
(f)
60.29 nm
29.03 nm
31.26 nm
200 nm
EHT = 10.00 kV
WD = 5.1 mm
Signal A = SE2
Mag = 50.00 K X
Date :2 Mar 2023
User Text =
ZEISS

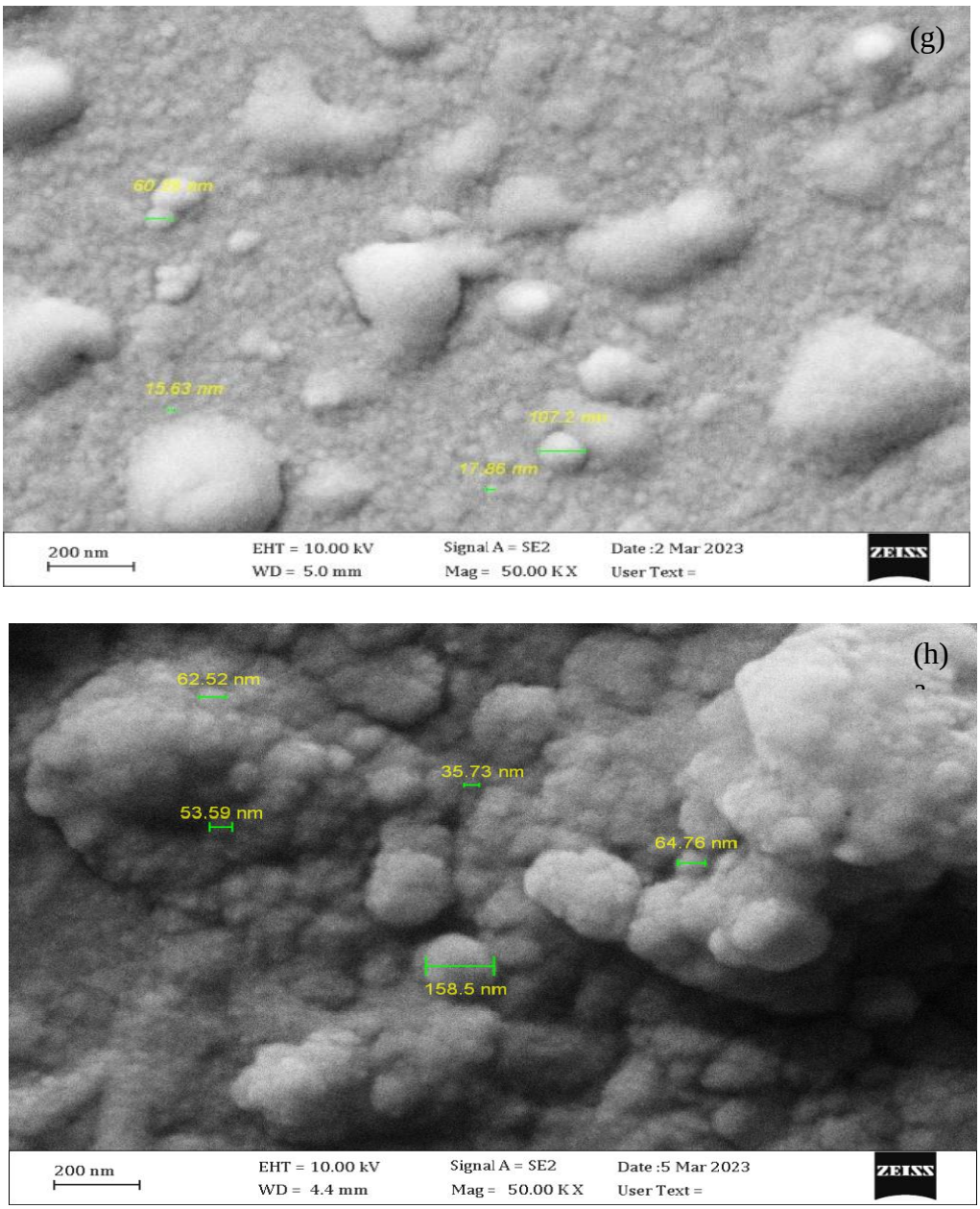

Fig (4.10) FE-SEM Images of $Cu_2O:CaF_2$ Thin Films with Different Thicknesses of a) 16 nm, b) 19 nm, c) 22 nm, d) 29 nm, e) 35 nm, f) 42 nm, g)50 nm and h) 57nm.

4.3 The Optical Properties

The main purpose of studying the optical properties of the $Cu_2O:CaF_2$ thin films with different thickness. The research covers the recording of the spectrum of absorbance of the $Cu_2O:CaF_2$ thin films at the room temperature and calculating the transmission, absorption coefficient, extinction coefficient and other optical constants, as well as identifying the types of electronic transitions and calculating energy gaps

4.3.1 Absorbance (A)

The optical properties of $Cu_2O:CaF_2$ thin film with different thicknesses are investigated using a UV-Visible spectrophotometer in the wavelength range (200-1100) nm. The absorbance of $Cu_2O:CaF_2$ thin film with different thicknesses was recorded at room temperature and calculating from the relation (2-5). Figure (4.11), display the variation of optical absorbance with wavelength of $Cu_2O:CaF_2$ thin film. From these figures it can be noted that the spectra reveal that all the films show more absorbance in ultraviolet region. All films show that low absorbance in the visible region, this behavior can be explained as follows at high wavelength the incident photons doesn't have enough energy to interact with atoms and thus the photon will be transmitted. When the wavelength decreases (at the neighborhood of the fundamental absorption edge), the interaction between incident photon and material will occur, and the photon will be absorbance. The absorbance increases with the increasing of thichness. This is due to absorb the incident light by free electrons. The results agree with the results of the previous researchers [93].

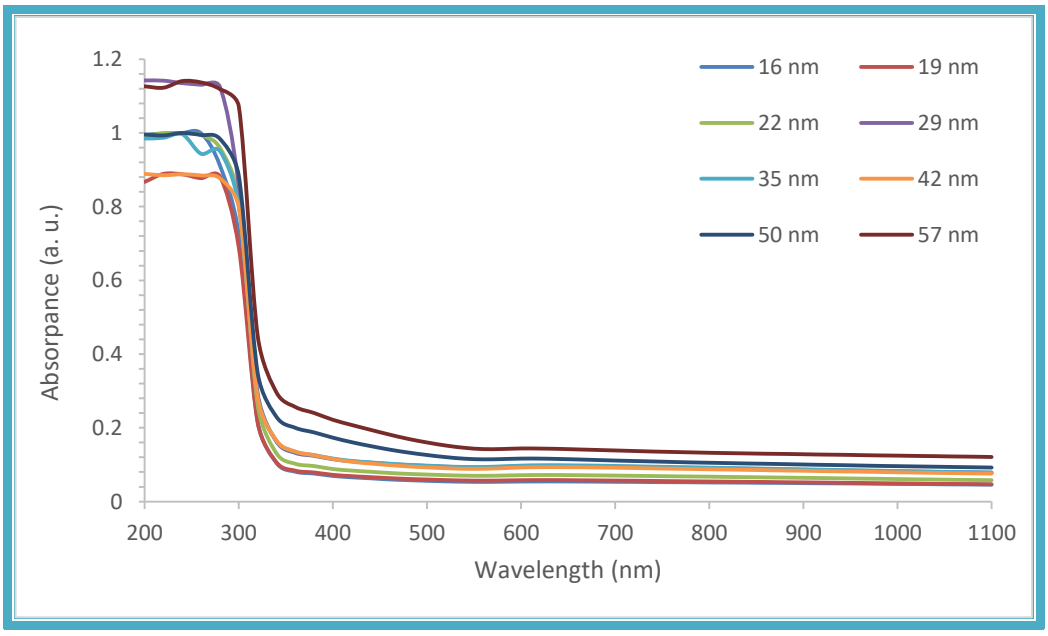

Fig (4.11) The Transmittance Versus Wavelength of $Cu_2O:CaF_2$ Thin Films with Different Thicknesses.

4.3.2 Transmittance (T)

Figure (4.12) explain the variation of transmittance of $Cu_2O:CaF_2$ nanofilm with different thicknesses with wavelength and calculating from the relation (2-6). It can be observed that the transmittance is decreased with the increase of thickness. This behavior is attributed to the increase in the number of atoms with thickness, which leads to the increase in the number of collisions between incident photons and atoms which leads to a decrease in transmittance. Also, the decrease in transmittance due to the onset of absorption edge for films became less sharp which is due to the fact that bigger crystallite sizes are deposited and because in this case, more atoms are present in the film so more states will be available for the photons to be absorbed, which is in accordance with the findings of researchers [94].

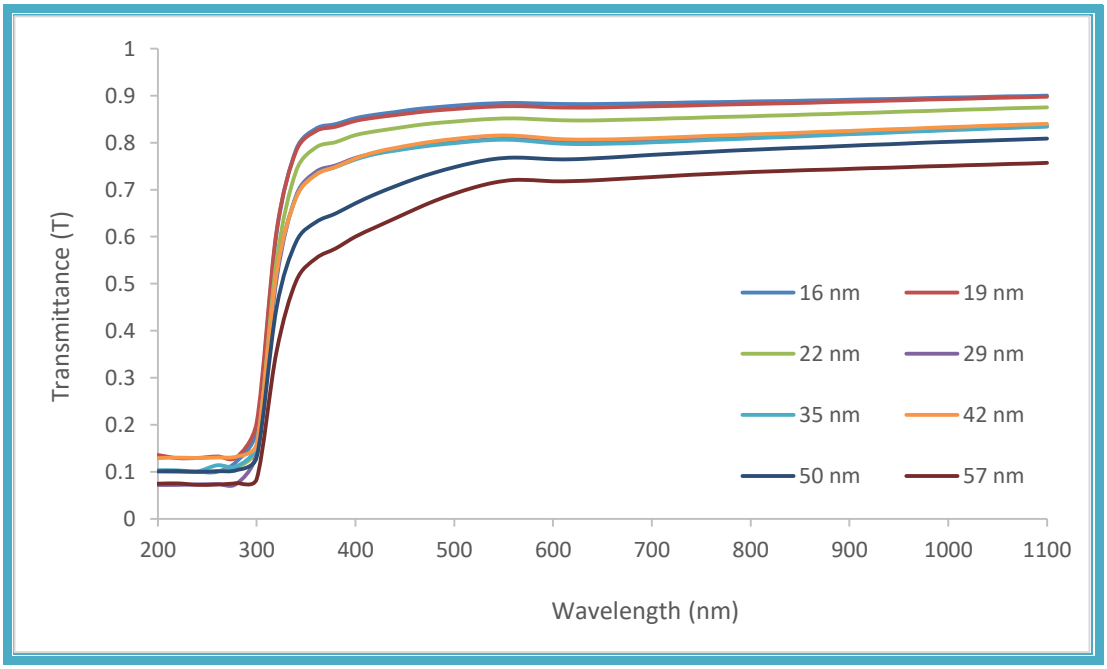

Fig (4.12). The Transmittance Versus Wavelength of $Cu_2O:CaF_2$ Thin Films with Different Thicknesses.

4.3.3 Absorption Coefficient (α)

The absorption coefficient (α) of $Cu_2O:CaF_2$ thin films are calculated using the equation (2-15). The variation of the absorption coefficient versus wavelength of $Cu_2O:CaF_2$ thin films with different thicknesses is presented in

Figure (4.13). From the figure, it can be observed that the absorption coefficient increased with the increase in thickness. Its value is larger than (10^4 cm^{-1}), which causes an increase in the probability of the occurrence of direct transitions. This can be linked with the increase in grain size and it may be attributed to the light scattering effect for its high surface roughness, which is in agreement with the finding of researchers [95].

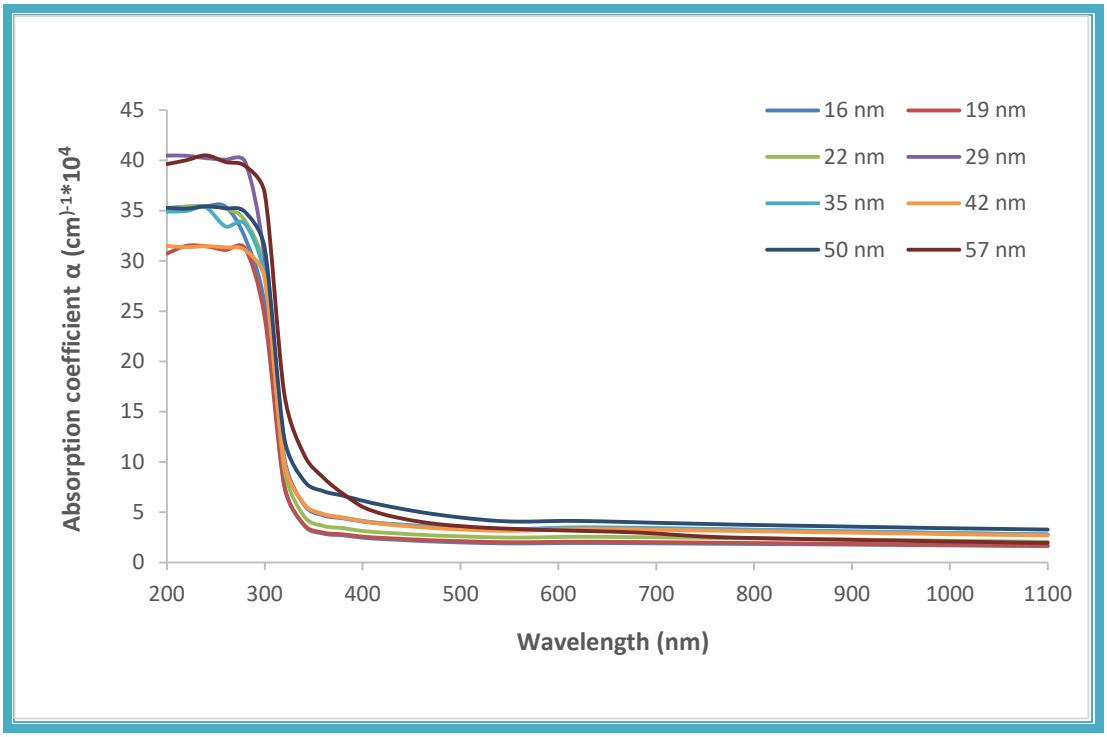

Fig. (4.13). The Absorption Coefficient Versus Wavelength of Cu_2O:CaF_2 Thin Films with Different Thicknesses.

4.3.4 Optical Energy Gaps of the Allowed Direct Transition

The optical energy gap of Cu_2O:CaF_2 thin films is determined using the equation (2-7). The plot of $(\alpha h\nu)^2$ with incident photon energy ($h\nu$) indicates that Cu_2O:CaF_2 films are direct transition type semiconductors for the thin films demonstrated in Figure (4.14). From the figure, it is clear that the direct energy gap of Cu_2O:CaF_2 films decreased from (3.77–3.62) eV as the thickness increased from 16 to 57 nm. This is due to the increase in the localized density of states near the band edges and in turn decreased the value of $E_g^{opt.}$ with thickness. Also, the decrease of the direct band gap with the increase in thickness can be attributed to an increase in particle size. This means that the

thickness also affects the band gap of the film. These results are in good agreement with the findings of the researchers [50, 54, 96]. The values of $E_g^{opt.}$ are listed in Table (4.3).

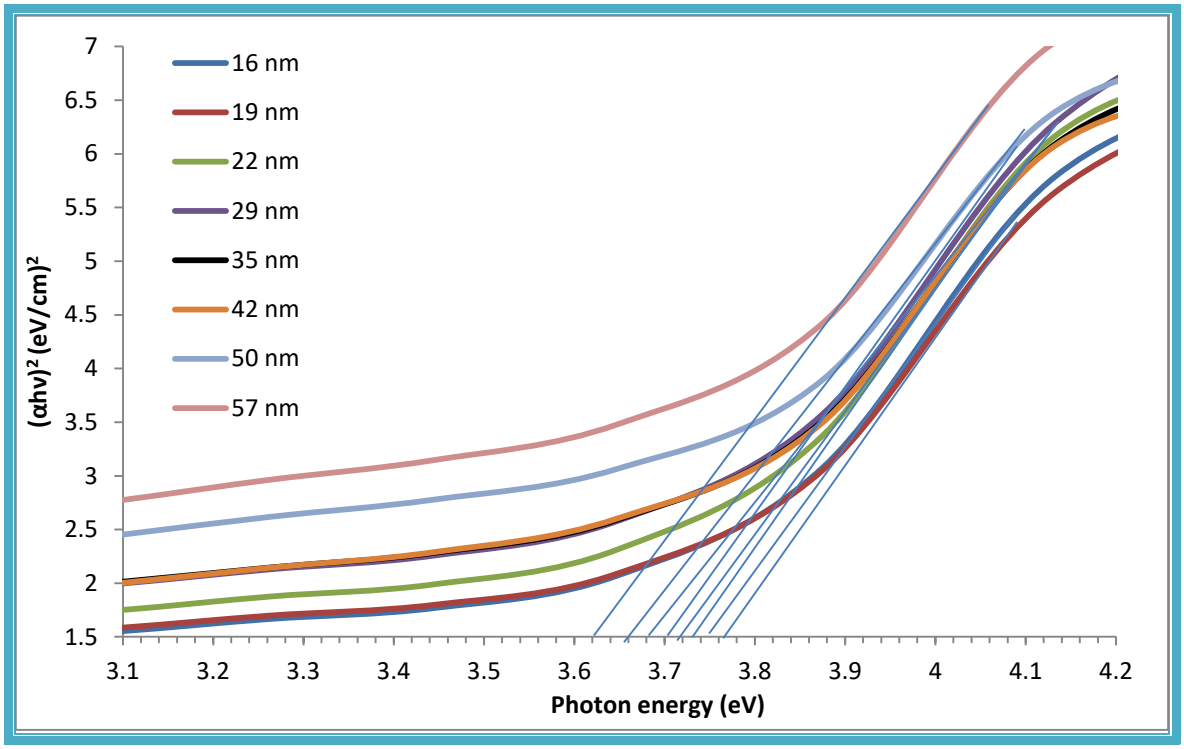

Fig (4.14) The allowed optical energy gap versus photon energy of Cu_2O:CaF_2 thin films with different thicknesses.

Table (4.3) The values of optical energy gap of the allowed direct transition of Cu_2O:CaF_2 thin film with different t57hicknesses.

Thickness (nm)	Allowed direct transition (eV)
16	**3.77**
19	**3.75**
22	**3.73**
29	**3.72**
35	**3.70**
42	**3.68**
50	**3.66**
57	**3.62**

4.3.5 Extinction Coefficient (k_o)

Extinction coefficient (k_o) was calculated using equation (2-14). The variation of the extinction coefficient versus wavelength of $Cu_2O:CaF_2$ thin films with different thicknesses is presented in figure (4.15). The figure shows that extinction coefficient increases with increasing thickness, this is due to the increase in optical absorption and photons dispersion in the $Cu_2O:CaF_2$ thin films. The results agree with the results of the previous researchers [97,98].

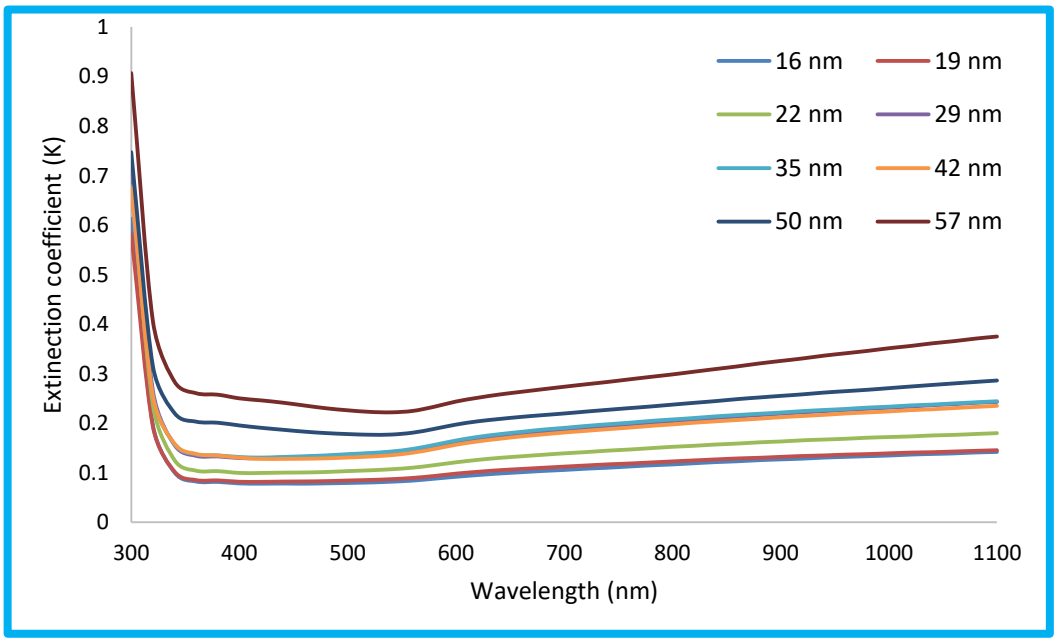

Fig (4.15) The Extinction Coefficient Versus Wavelength of $Cu_2O:CaF_2$ Thin Films with Different Thicknesses.

4.3.6 Refractive Index (n)

The refractive index was calculated from equation (2-13). Figure (4.16) show the change of refraction index of $Cu_2O:CaF_2$ thin films with different thicknesses as a function of wavelength. From the figure, it can see that the refractive index increases with increasing thicknesses, also it is decreased with the increase of the wavelength. This behavior attributed to the increase of the density of nanocomposites. When the incident light interacts with a sample has high refractivity at UV region, hence, the values of refractive index will be increased. The results agree with the results of the previous researchers [99].

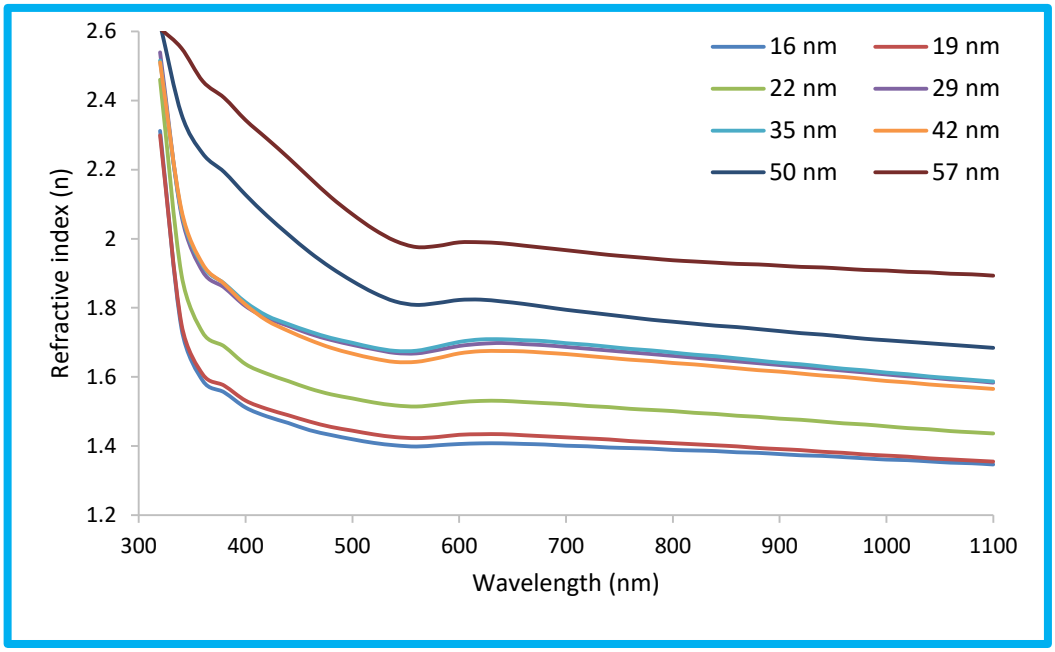

Fig (4.16) The Refractive Index Versus Wavelength of Cu_2O:CaF_2 Thin Films with Different Thicknesses.

4.3.7 Real and Imaginary Parts of Dielectric Constant

The real (ε_r) and imaginary (ε_i) dielectric constant of the Cu_2O:CaF_2 nano films system is determined using the equations (2.21) and (2.22). The variation of real (ε_r) and imaginary (ε_i) parts of the dielectric constant values as a function with wavelength. From these figures, it is found that ε_r and ε_i increased with increasing of thickness. The behavior of ε_r is similar to that of the refractive index because of the smaller value of k_o^2 compared with n^2, while ε_i is mainly dependent on the k_o^2 values according to equations (2.3). This behavior is in agreement with the results of the researchers [56, 100].

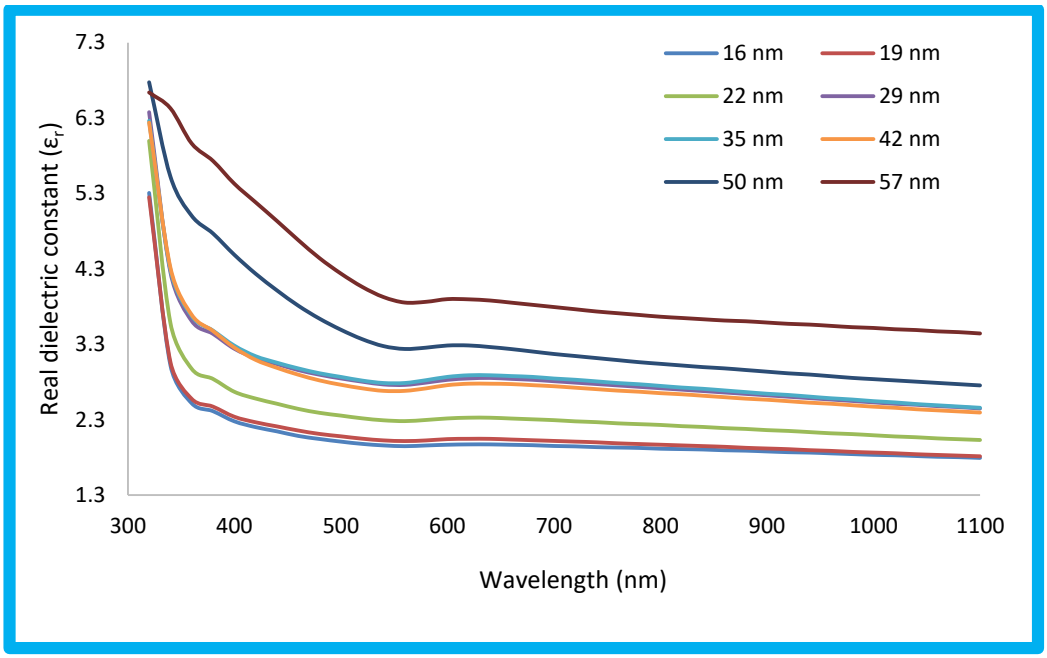

Fig (4.17) The Real Part of Dielectric Constant Versus Wavelength of $Cu_2O:CaF_2$ Thin Films with Different Thicknesses.

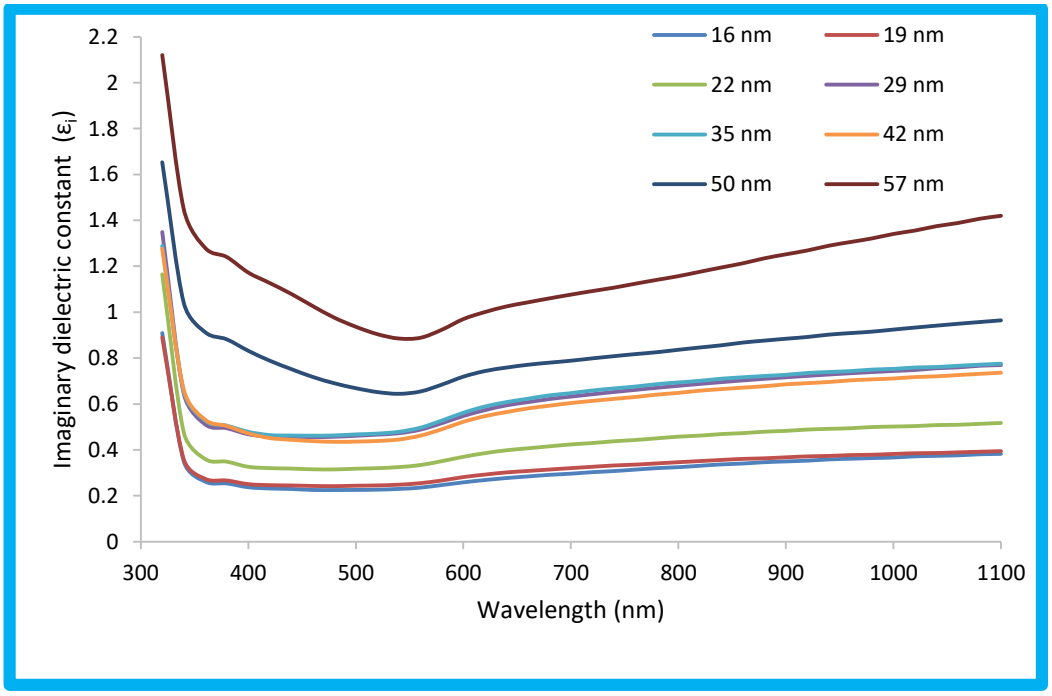

Fig (4.18) The Imaginary Part of Dielectric Constant Versus Wavelength of $Cu_2O:CaF_2$ Thin Films with Different Thicknesses.

4.3.8 The Optical Conductivity (σ)

The optical conductivity (σ_{op}) has been calculated using equation (2-23). Figure (4.19) show that the optical conductivity of the samples versus wavelength of $Cu_2O:CaF_2$ nano films with different thicknesses. The optical conductivity decreases with the increasing of the wavelength, this behavior, attributed to optical conductivity, was strongly dependent on the wavelength of the radiation incident on the $Cu_2O:CaF_2$ nano films; the increases in optical conductivity at low wavelengths of photon is due to high absorbance of all composite samples in this region, resulting in an increasing in charge transfer excitations. The optical conductivity spectra revealed that the samples transmit light in the visible and near-infrared ranges. Additionally, the optical conductivity of $Cu_2O:CaF_2$ nano films increases with the thickness, this behavior is related to the formation of localized levels in the energy gap; an increase in the thickness increasing the density of localized stages in the band structure. hence, increases of the absorption coefficient consequently increasing the optical conductivity of $Cu_2O:CaF_2$ nano films. The results agree with the results of the previous researchers [57, 101].

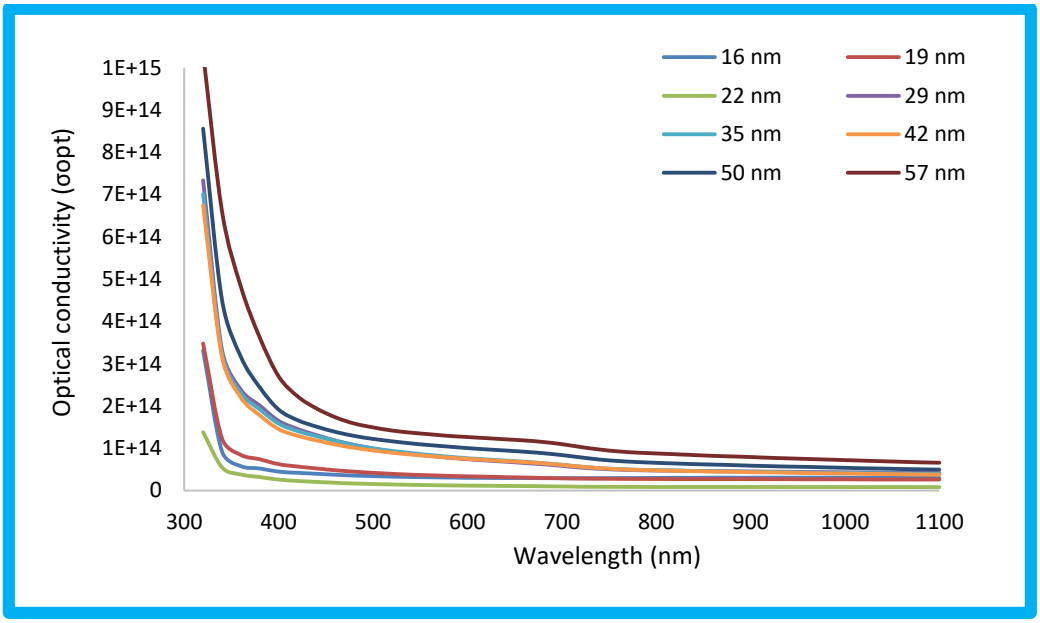

Fig (4.19) The Optical Conductivity Versus Wavelength of $Cu_2O:CaF_2$ Thin Films with Different Thicknesses.

4.4 The Volume Energy Loss Function (VELF) and Surface Energy Loss Function (SELF).

The Surface Energy Loss Function (SELF) and Volume Energy Loss Function (VELF) were calculated from the relations (2-24) and (2-25) respectively. Figures (4.20) and (4.21) display the wavelength dependence of the SELF and VELF values of Cu_2O:CaF_2 thin films with different thicknesses. From the figures, it can be observed that the SELF and VELF increased with the increment of wavelength. As they increased in thickness, the SELF and VELF shift, and the electron transition energy shifts along with them [102].

The surface energy loss function (Figure 4.20) increased with the film thickness increasing for the few nanomaterials, where the surface energy is the ability of the material to interact with a substrate. When the film is very thin and can spread itself on a certain substrate, it is the best possible because it will disappear several energies, including the elastic energy, and it can be neglected because it controls by neglecting this energy, and thus there will be a direct interaction between the nanomaterial and the surface. Also, the potential energy will be neglected, and this will lead to the formation of a first layer on the substrate and then a second surface energy will come to form a second layer and thus a volume will be formed. The volume appears because it is a surface with thickness. It will be volume, and therefore the volume energy will appear. Therefore, the volume energy according to this figure does not show a large difference, while the surface energy will have a difference due to the very little thickness of the film.

From the figures, it can be note that the prepared thicknesses are less than the critical thickness, making the films with the best performance and properties. These results as in the finding in the AFM and SEM results.

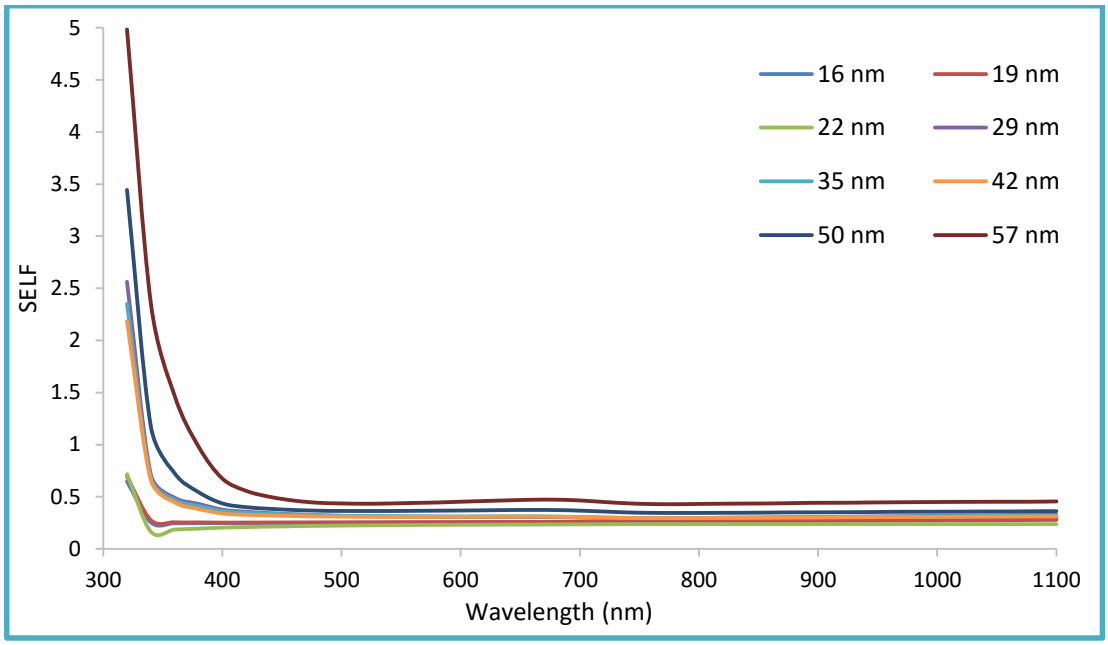

Fig (4.20) Surface Energy Loss Functions as a Function of the Wavelength of $Cu_2O:CaF_2$ Thin Films with Different Thicknesses.

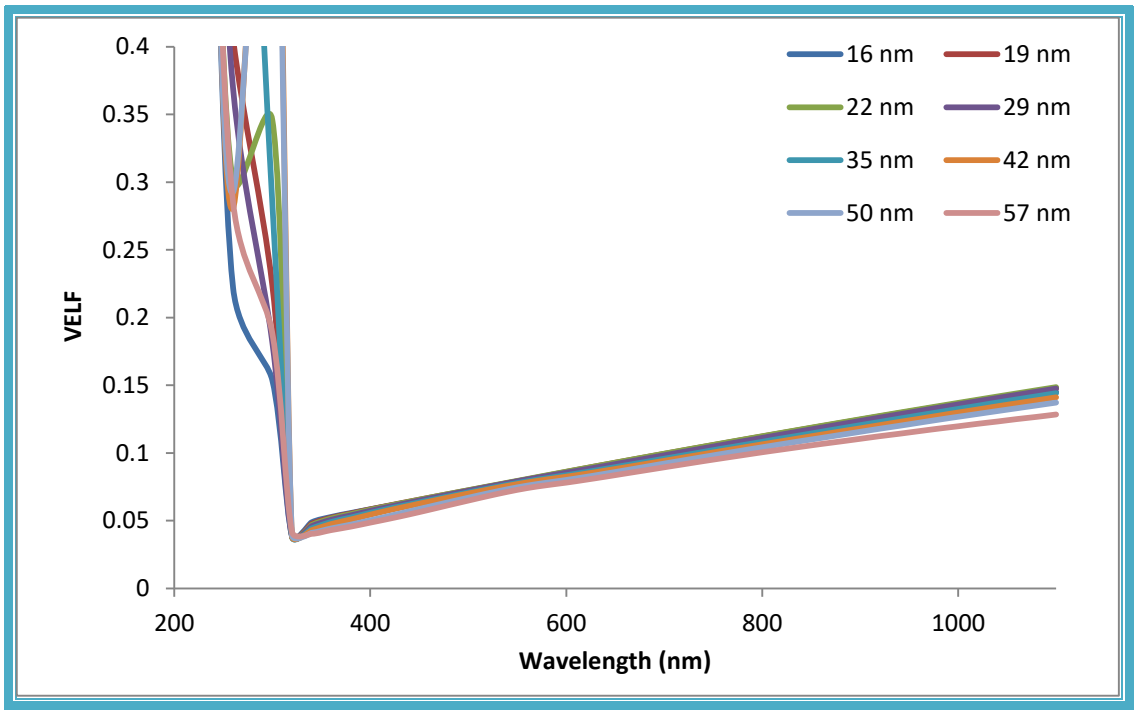

Fig (4.21) Volume Energy Loss Functions as a Function of the Wavelength of $Cu_2O:CaF_2$ Thin Films with Different Thicknesses.

4.5 Dispersion Parameters

Dispersion parameters were studied and diagnosed using the Wemple-DiDomenico model with different thicknesses. The quantities of E_o, E_d, E_g, n_o, n_2, M_{-1}, M_{-3} were calculated from the equations (2.27- 2.30). From drawing the graphic relationship between $(n^2-1)^{-1}$ and $(h\upsilon)^2$ as shown in figure (4.22). The calculated values were listed in Table (4.4) showing an increase in their values; E_g, E_d, n_o and M_{-1} with the increasing of thickness of $Cu_2O:CaF_2$ thin films while the values; E_o and M_{-3} decrease with the increase of thickness of $Cu_2O:CaF_2$ thin films. The value of the energy gap estimated by Wemple–DiDomenico was comparable with the value of the optical energy gap obtained from the Tauc relation. The results agree with the results of the researchers [103].

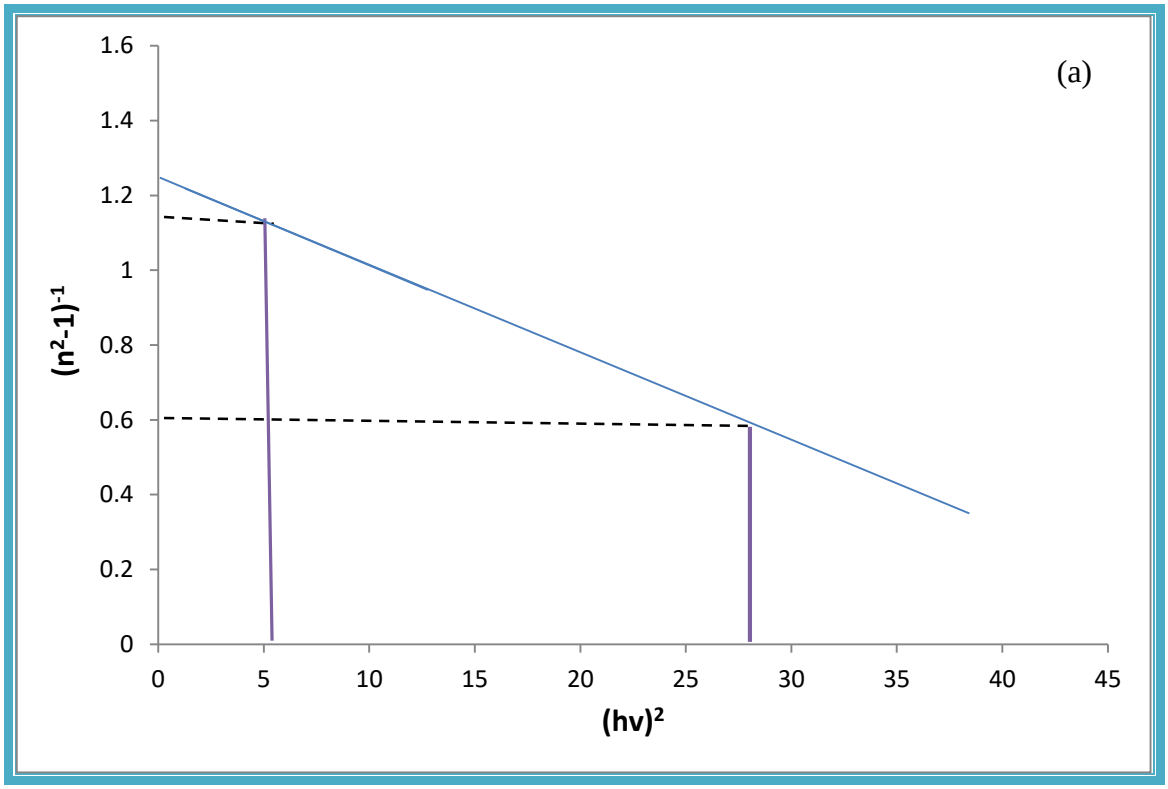

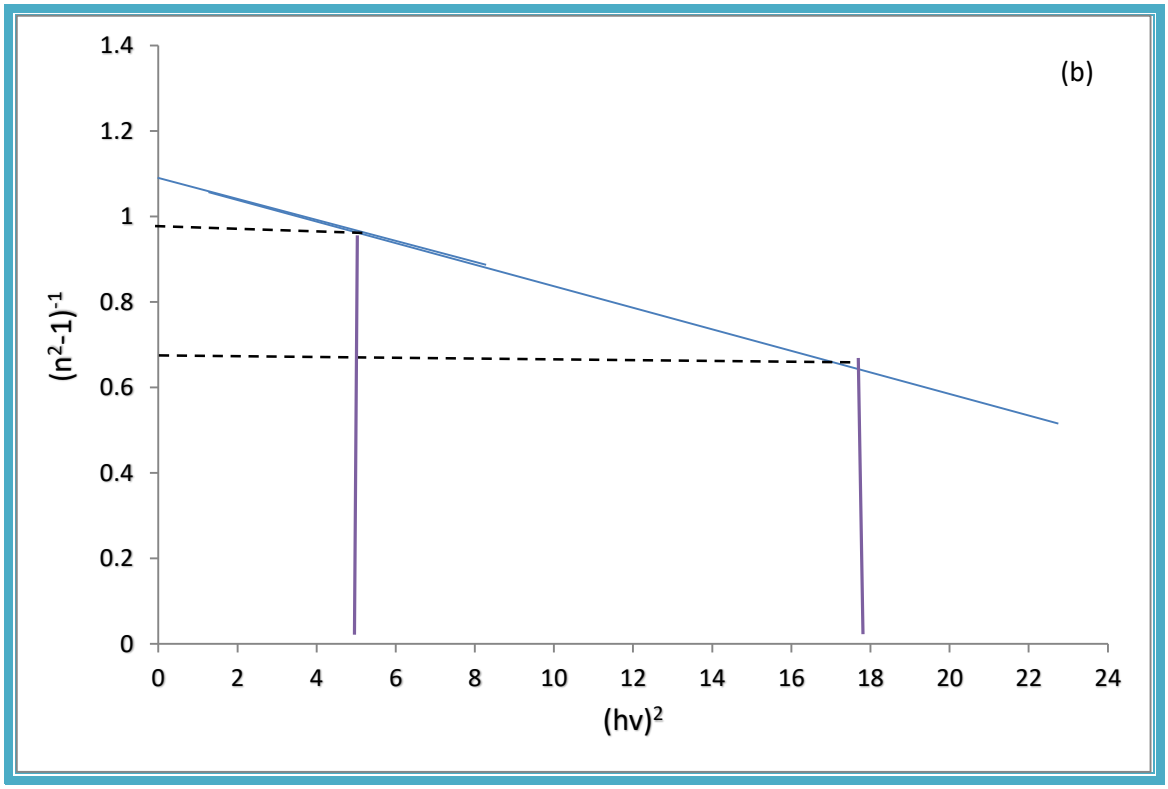
(b)
1.4
1.2
1
0.8
0.6
0.4
0.2
0
$(n^2-1)^{-1}$
0 2 4 6 8 10 12 14 16 18 20 22 24
$(hv)^2$

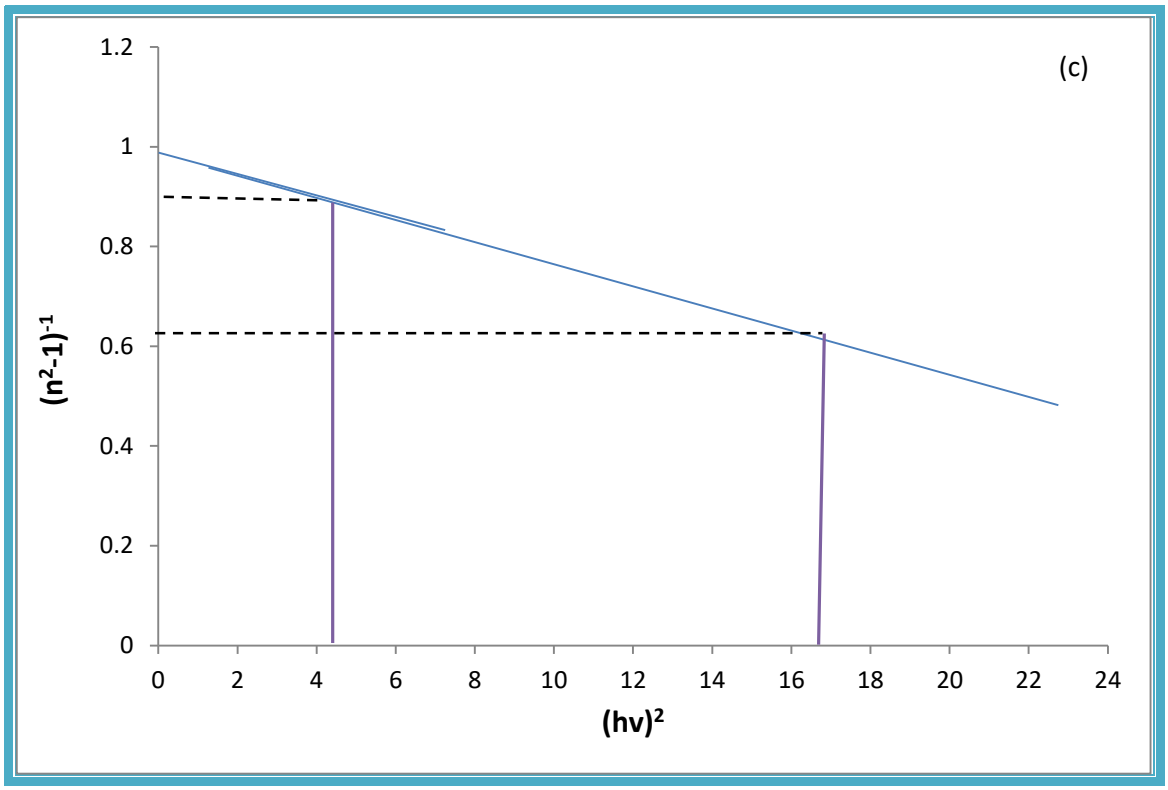
(c)
1.2
1
0.8
0.6
0.4
0.2
0
$(n^2-1)^{-1}$
0 2 4 6 8 10 12 14 16 18 20 22 24
$(hv)^2$

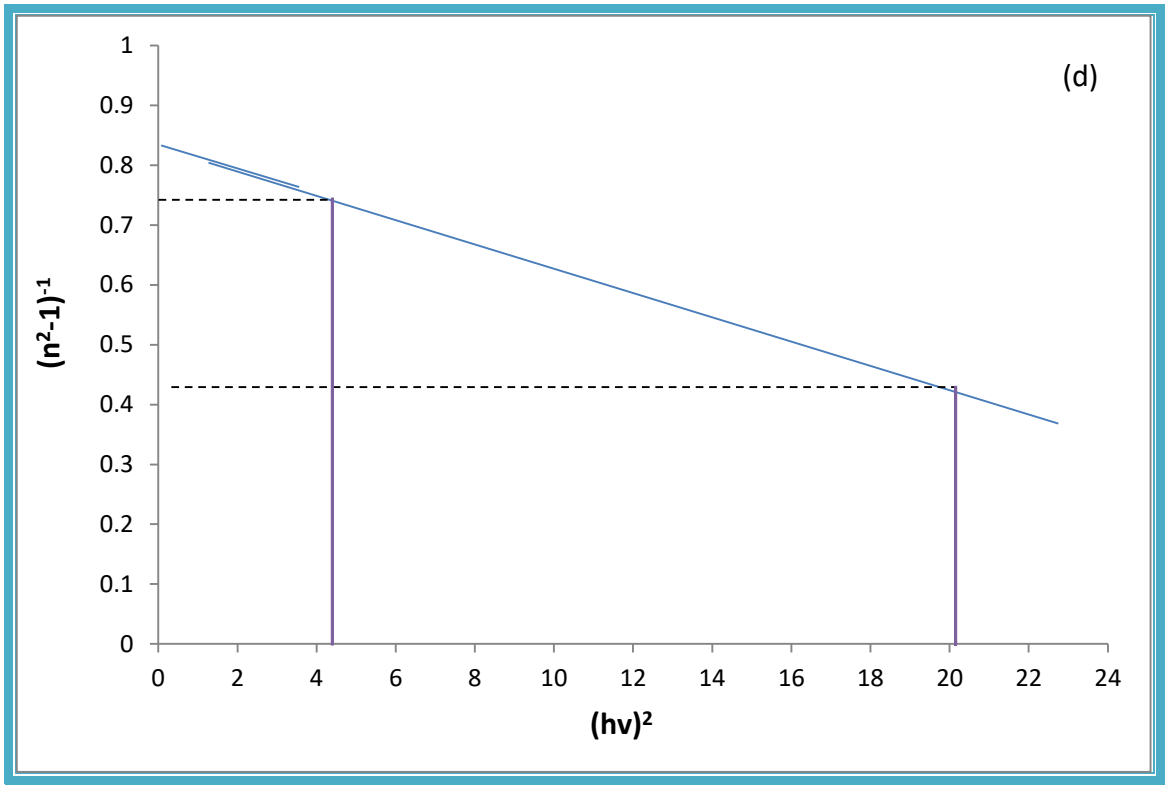
(d)
$(n^2-1)^{-1}$
$(hv)^2$
0
0.1
0.2
0.3
0.4
0.5
0.6
0.7
0.8
0.9
1
0 2 4 6 8 10 12 14 16 18 20 22 24

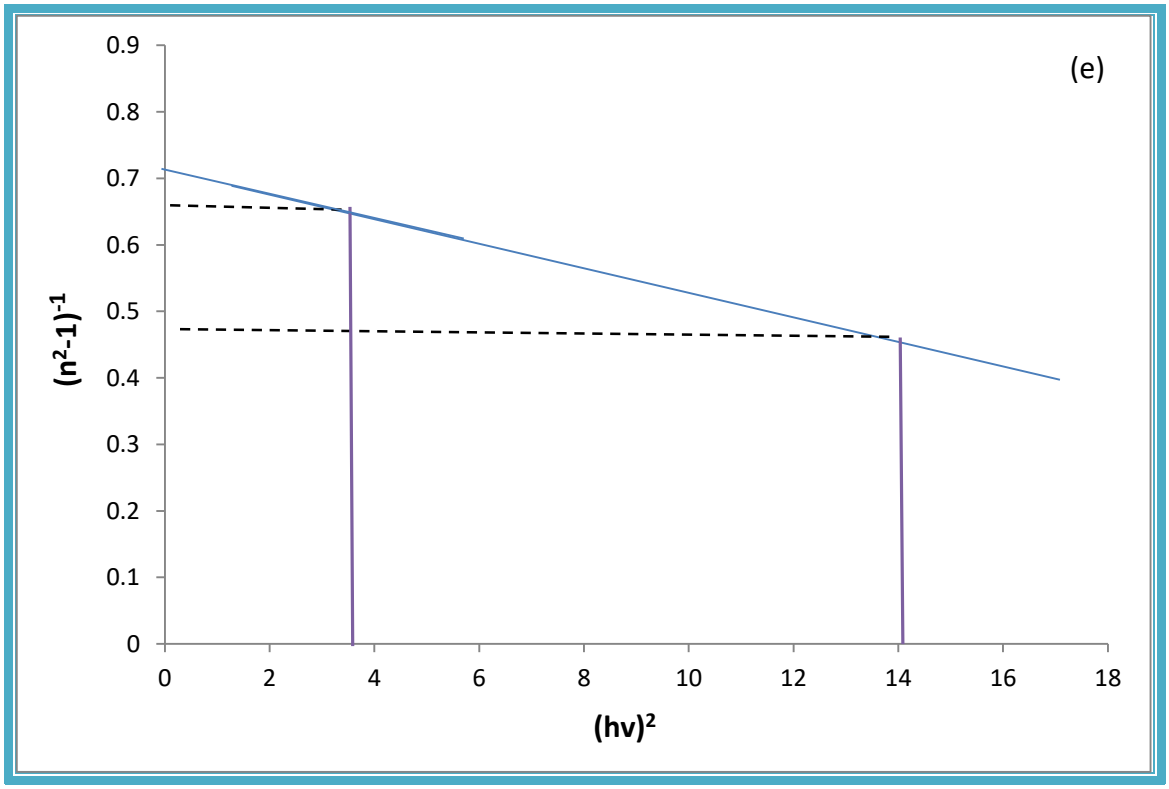
(e)
$(n^2-1)^{-1}$
$(hv)^2$
0
0.1
0.2
0.3
0.4
0.5
0.6
0.7
0.8
0.9
0 2 4 6 8 10 12 14 16 18

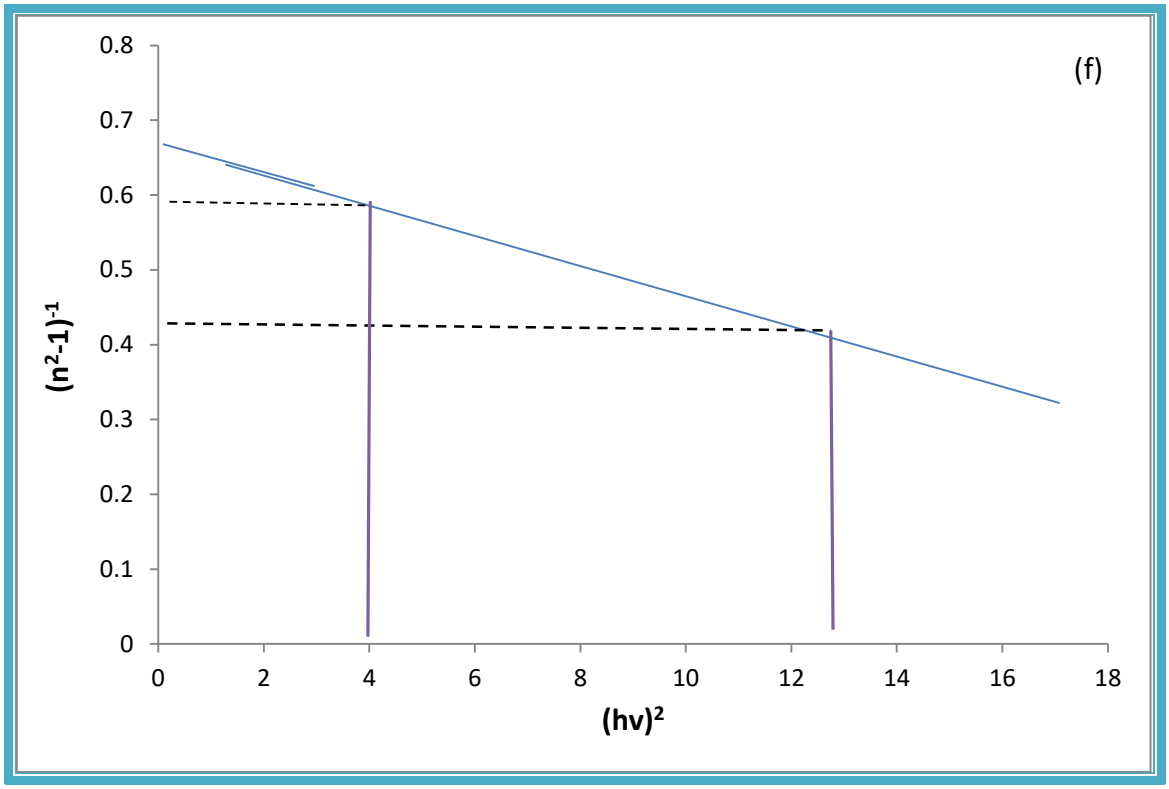
(f)
0.8
0.7
0.6
0.5
0.4
0.3
0.2
0.1
0
$(n^2-1)^{-1}$
0 2 4 6 8 10 12 14 16 18
$(hv)^2$

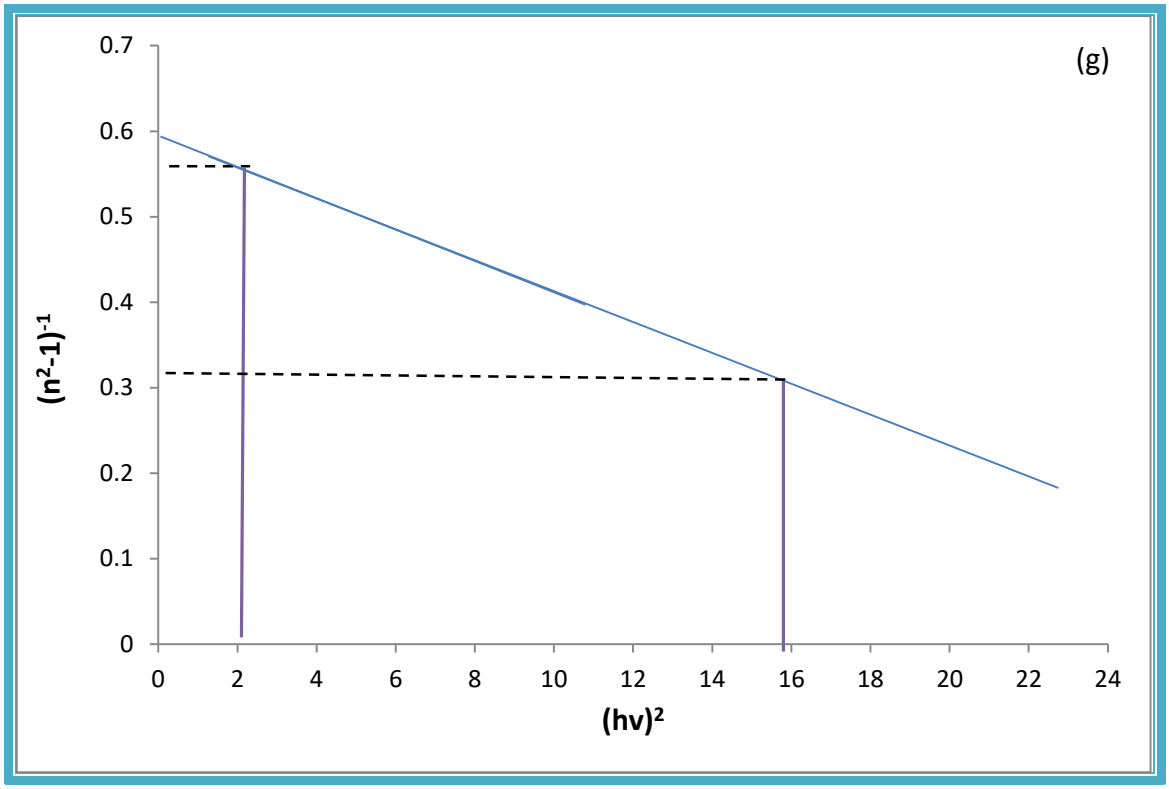
(g)
0.7
0.6
0.5
0.4
0.3
0.2
0.1
0
$(n^2-1)^{-1}$
0 2 4 6 8 10 12 14 16 18 20 22 24
$(hv)^2$

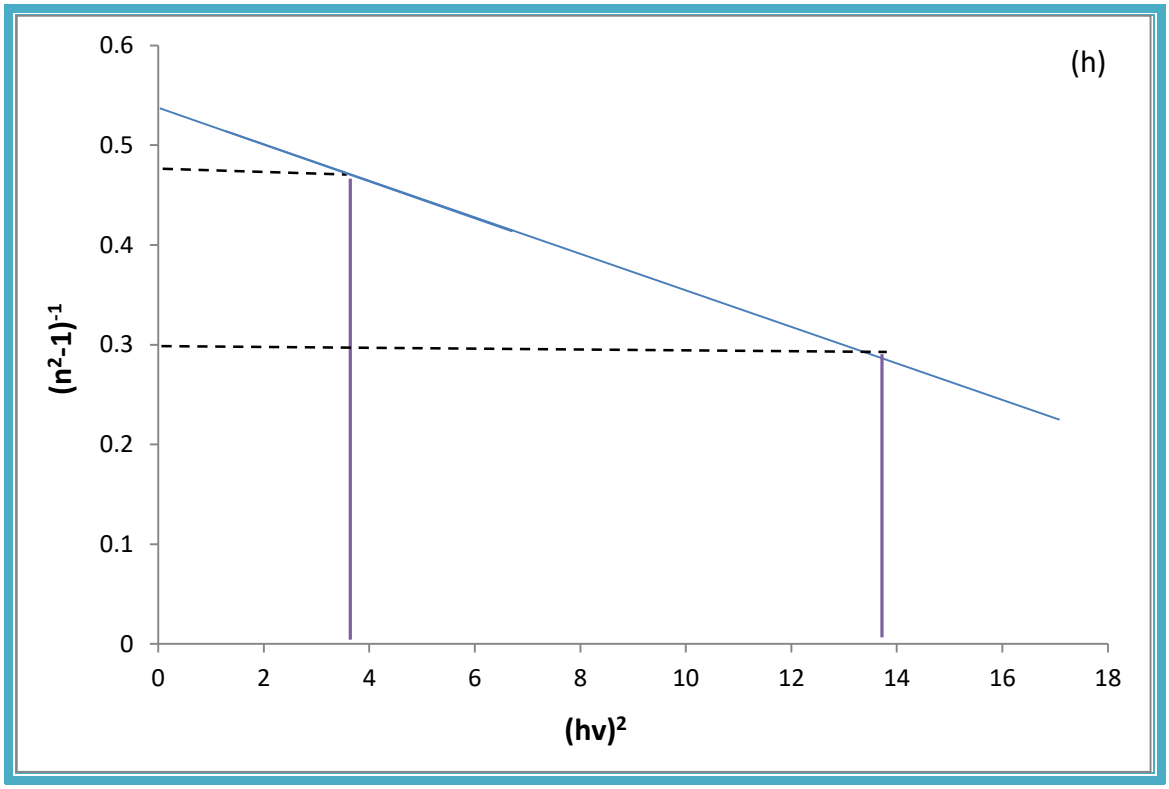

Fig (4.22) Plot of $(n^2 -1)^{-1}$ vs $(h\upsilon)^2$ of $Cu_2O:CaF_2$ Thin Film with Different Thicknesses of (a) 16 nm, (b) 19 nm, (c) 22 nm, (d) 29 nm, (e) 35 nm, (f) 42 nm, (g) 50 nm, (h) 57 nm.

Table (4.4) Dispersion Parameters of $Cu_2O:CaF_2$ Thin Film with Different Thicknesses.

Parameter	$Cu_2O:CaF_2$							
	16 nm	19 nm	22 nm	29 nm	35 nm	42 nm	50 nm	57 nm
E_o	7.072482	6.537802	6.333584	6.23355	6.217359	5.955719	5.815342	5.582711
E_d	5.797116	5.943457	6.597483	7.333588	8.756844	8.889133	9.692234	10.15038
E_g	3.536241	3.268901	3.166792	3.116775	3.10868	2.977859	2.90767	2.791356
$n_2(0)$	1.819672	1.909091	2.041667	2.176471	2.408451	2.492537	2.666667	2.818182
$n_o(0)$	1.348952	1.381699	1.428869	1.475287	1.551918	1.578777	1.632993	1.678744
M_{-1}	0.819672	0.909091	1.041667	1.176471	1.408451	1.492537	1.666667	1.818182
M_{-3}	0.016387	0.021269	0.025967	0.030277	0.036436	0.042078	0.049283	0.058337

4.6 Conclusions

From the results of this work, the following can be concluded

1. A successful thermal evaporation technique was used to prepare (for the first time) $Cu_2O_{(0.75)}$:$CaF_{2(0.25)}$ thin films.

2. from XRD can be concluded that the prepared films were amorphous. With increasing thickness, the peak exhibited at 24.2°, which attributed to the CaF_2 that corresponded to the (111) with face center cubic.

3. Atomic force microscopy (AFM) confirmed that the films grown by this technique had a good homogeneous surface. The roughness average, root mean square value, and average grain diameter increased with the increasing thickness.

4. Field Emission Scanning Electron Microscope (FE-SEM) uniform morphology revealing a rather soft surface and with increase of the thickness led to changes in the morphology of the surface and increase the roughness.

5. The optical properties can be concluded that the absorbance, absorption coefficient, extinction coefficient, refractive index, real and imaginary dielectric constant and optical conductivity increased with increasing thickness while the transmittance and energy gap decreased with the increase of thickness. The Cu_2O:CaF_2 thin films allowed a direct energy gap (E_g) that was decreased from 3.77 to 3.62 eV with the increase of thickness.

6. The SELF and VELF values observed that the SELF and VELF increase with the increment of thickness.

7. The dispersion parameters such as; E_o, E_d, n_o, n_2, M_{-1}, and M_{-3} were calculated using the Wemple–DiDomenico model. The value of the energy gap estimated by Wemple–DiDomenico calculations was consistent with the value

of the optical energy gap obtained from the Tauc relation and found that the parameters were decreased with the increase of thickness.

4.7 Future Works

1- Effect of thickness as antireflection coating of Cu_2O:CaF_2 solar cell by using thermal evaporation technique.

2- Fabrication and study the effect of thickness on efficiency of Cu_2O:CaF_2 solar cell that are prepared by thermal evaporation technique.

3- Using of Cu_2O:CaF_2 thin film as a gas sensor.

References

[1] K. L. Chopra, "Thin film devices application", Plenum press, New York, (1983).

[2] K. L. Chopra, "Thin films phenomena", Mc. Graw-Hill, NewYork, (1969).

[3] L. Eckortova, "Physics of thin films", Plenum press, (1977).

[4] R. H. Bossert, C. J. Tool, J. A. Roosmalen, C. H. Wentink, and M. J. Devaan, "Thin-Film Solar Cells", Technology Evaluation and Perspectives, Netherlands Energy Research Foundation – ECN, (2000).

[5] M. Cernea, "Methods for preparation of $BaTiO_3$ thin films", J. of Opotoelectronics and Advanced Materials, Vol. 6, No. 4, pp. 1349 – 1356, (2004).

[6] N. Abid, A. M. Khan, S. Shujait, K. Chaudhary, M. Ikram, M. Imran, M. Maqbool, M., "Synthesis of nanomaterials using various top-down and bottom-up approaches, influencing factors, advantages, and disadvantages A review. Advances in Colloid and Interface Science, 102597. (2021).

[7] V. Pokropivny, R. Lohmus, I. Hussainova, A. Pokropivny, S. Vlassov, "Introduction to nanomaterials and nanotechnology (Vol. 1, p. 138). Ukraine" Tartu University Press, (2007).

[8] A. D. Gopakumar, A. R. Pai, D. Pasquini, L. S. Y. Ben, A. K. HPS, S. Thomas,"Nanomaterials—state of art, new challenges, and opportunities" Nanoscale Materials in Water Purification, pp. 1-24, (2019).

[9] C. J. Richard, "Film Deposition Introduction to Microelectronic Fabrication", (2nd ed.), Upper Saddle River Prentice Hall. (2000).

[10] S. M. Sze, "Semiconductor Devices Physics and Technology", (2001).

[11] R. D. Mathis, "Company Evaporation Sources Catalog", pp.(1-7), (1992).

[12] M. Fox, "Quantum optics; an introduction", Oxford University, Press, (2006).

[13] A. Guinier, "X-ray diffraction in crystals, imperfect crystals, and amorphous bodies", Freeman, San Francisco, (1963).

[14] J. Als-Nielsen and D. McMorrow, "Elements of modern X-ray physics", John Wiley and Sons, Ltd., Chichester, (2001).

[15] C. S. Barrett and T. B. Massalski, "Structure of Metals", Mc Graw-Hill, New York, (1966).

[16] A. Singh, D. Kumar, P. K. Khanna, B. C. Joshi and M. Kumar, "Effect of post annealing temperature on structural and optical properties of ZnCdO thin films deposited by sol–gel method" Applied Surface Science, Vol. 258, No.5, pp. 1881-1887, (2011).

[17] C. Guillen and J. Herrero, J., "Single-Phase Cu2O and CuO Thin Films Obtained by Low-Temperature Oxidation Processes" Journal of Alloys and Compounds, Vol.737, pp. 718-724, (2018).

[18] J. Sultana, J., S. Paul, R. Saha, S. Sikdar, A. Karmakar and S. Chattopadhyay, "Optical and Electronic Properties of Chemical Bath Deposited p-CuO and n-ZnO Nanowires on Silicon Substrates p-CuO/n-ZnO Nanowires Solar Cells with High Open-Circuit Voltage and Short-Circuit Current" Thin Solid Films , Vol. 699, (2020).

[19] M. Ajili and N. T. Kamoun, "Structural and Optoelectronic Studies of CuO, In2-xAlxS3 and SnO2:F sprayed thin films for solar cell application Au/CuO (p)/ In2-xAlxS3(n)/SnO2:F.", Optik, Vol. 229, (2021)

[20] L. Gao, C. Pang, D. He, L. Shen, A. Gupta, A., N. Bao, N., "Synthesis of hierarchical nanoporous microstructures via the Kirkendall effect in chemical reduction process" Scientific reports, Vol. 5, No. 1, pp.1-12, (2015).

[21] R. Shabu, M. E. Raj, C. Sanjeeviraja and C. Ravidhas, "Assessment of CuO Thin Films for Its Suitablity as Window Absorbing Layer in Solar Cell Fabrications" Materials Research Bulletin, Vol. 68, pp.1-8, (2015).

[22] J. Kondo, "Cu_2O as a photocatalyst for overall water splitting under visible light irradiation" Chemical Communications, Vol.3, pp.357-35, (1998).

[23] J. N. Nian, C. C. Hu and H. Teng, "Electrodeposited p-type Cu_2O for H2 evolution from photoelectrolysis of water under visible light illumination" Int. J. Hydrogen Energy, Vol. 33, No.12, pp. 2897-2903, (2008).

[24] H. Zhang, Q. Zhu, Y. Zhang, Y. Wang, L. Zhao and B. Yu, "One-Pot Synthesis and Hierarchical Assembly of Hollow Cu_2O Microspheres with Nanocrystals-Composed Porous Multi shell and Their Gas-Sensing Properties", Advanced Functional Mater., Vol. 17, No.15, pp. 2771-2766, (2007).

[25] S. T. Shishiyanu, and O. I. Lupan, O. I., "Novel NO_2 gas sensor based on cuprous oxide thin films. Sensors and Actuators B" Chemical, Vol. 113, No.1, pp. 468-476, (2006).

[26] Y. Bessekhouad, D. Robert and J. V. Weber, "Photocatalytic activity of Cu_2O/TiO_2، Bi_2O_3/TiO_2 and $ZnMn_2O4/TiO_2$ heterojunctions" Catalysis Today, Vol. 101, No.3, pp. 315-321, (2005).

[27] W. Siripala, A. Ivanovskaya, T.F. Jaramillo, S. H. Baeck and E. W. McFarland, "A Cu_2O/TiO_2 heterojunction thin film cathode for photoelectrocatalysis. Solar Energy Materials and Solar Cells, Vol. 77, No. 3, pp.229-237, (2003)

[28] T. Minami, Y. Nishi, T. Miyata and J. I. Nomoto,"High-efficiency oxide solar cells with ZnO/Cu_2O heterojunction fabricated on thermally oxidized Cu_2O sheets" Appl. Phys. Expr., Vol. 4, No. 6), (2011).

[29] K. Akimoto, S. Ishizuka, M. Yanagita, Y. Nawa, G. K. Paul and T. Sakurai, "Thin film deposition of Cu_2O and application for solar cells" Solar Energy, Vol. 80, No. 6, pp. 715-722, (2006).

[30] W. Septina, S. Ikeda, M. A. Khan, T. Hirai, T., Harada, M. Matsumura, and L. M. Peter, "Potentiostatic electrodeposition of cuprous oxide thin films for photovoltaic applications" Electrochimica Acta, Vol.56, No. 13, pp. 4882-4888, (2015).

[31] A. Chen, H. Long, X. Li, Y. Li, G. Yang, G. and P. Lu, P., "Controlled growth and characteristics of single-phase Cu_2O and CuO films by pulsed laser deposition" Vacuum، Vol. 83, No.6, pp.927-930, (2009).

[32] T. Maruyama, "Copper oxide thin films prepared by chemical vapor deposition from copper dipivaloylmethanate" Solar Energy Materials and Solar Cells, Vol. 56, No. 1, pp. 85-92, (1998).

[33] M. F. Al-Kuhaili, "Characterization of copper oxide thin films deposited by the thermal evaporation of cuprous oxide (Cu_2O), Vacuum, Vol. 82, No. 6, pp. 623-629, (2008).

[34] C. S. Wang, "Properties of calcium fluoride up to 95 kbar A theoretical study" Bulletin of Materials Science, Vol.33, No. 4, pp.413-418, (2010).

[35] B. B. Bohara, "AB-INITIO COMPUTATIONS OF ELECTRONIC, TRANSPORT, AND BULK PROPERTIES OF CALCIUM FLUORIDE (CaF_2) ", PhD., Southern University, (2016).

[36] C. H. Lee, J. Qi, J., S. T. Lee, L. S. Hung, "Epitaxial diamond on a Si/CaF2 /Ir substrate" Diam." Relat. Mater., Vol.12, pp.1335–1339, (2003).

[37] A. Klust, M. Bierkandt, J. Wollschläger, B. H. Müller, T. Schmidt, J. Falta", Low-temperature interface structure of CaF_2 /Si (111) studied by combining x-ray standing waves with component-resolved photoemission" Phys. Rev., Vol. 65, p.193404, (2002).

[38] J. Wollschläger, T. Hildebrandt, R. Kayser, J. Viernow, A. Klust, A, J. Bätjer, A. Hille, "Schmidt, T.; Falta, J. Effects of electron irradiation on the structure and morphology of CaF2 /Si (111)" Appl. Surf. Sci., Vol. 162, pp. 309–318, (2000).

[39] A. Klust, R. Kayser, J. Wollschläger, "Growth kinetics of CaF_2 /Si (111) for a two-step deposition", Phys. Rev., Vol.62, p.2158, (2000).

[40] J. G. Cook, G. H. Yousefi, S. R. Das, "Mitchell, D.F. RF magnetron deposition of calcium fluoride" Thin Solid Film, Vol. 217, pp. 87–90. (1992).

[41] N. Sata, K. Eberman, K. Eberl, "Maier, J. Mesoscopic fast ion conduction in nanometre-scale planar heterostructures", Nature , Vol.408, pp. 946–949, (2000).

[42] T. Maki, K. Okamoto, M. Sugiura, T. Hosomi, T. Kobayashi, "The great improvement of surface smoothness of CaF_2 in pulsed laser deposition even under the two-photon absorption process" Appl. Surf. Sci., Vol. 197, pp, 448–451, (2002).

[43] S. S. Shushtarian, S. B. Ogale, G. N. Chaudhari, P. Singh, V. J. Rao,, "Epitaxial growth of CaF_2 thin films on (100) GaAs by pulsed-laser deposition and in-situ annealing", Mater. Lett., Vol.12, pp.335–338, (1991).

[44] N. E. Çetin, S. Korkmaz, ¸S. Elmas, N. Ekem, S. Pat, G. Balba, E. Tarhan, S. Temel, M. Özmumcu, "The structural, optical and morphological properties of CaF_2 thin films by using Thermionic VacuumArc (TVA)", Mater. Lett., Vol. 91, pp.175–178, (2013).

[45] K. N. Manjunatha, S. Paul, "Investigation of optical properties of nickel oxide thin films deposited on di_erent substrates" Appl. Surf. Sci., Vol. 352, pp.10–15, (2015).

[46] J. Chen, Z. Zhang, Y. Guo, J. Robertson, J., "Electronic properties of CaF_2 bulk and interfaces", Journal of Applied Physics, Vol. 131, No.21, 2p.15302, (2022).

[47] D. S. Murali, S. Kumar, R. J. Choudhary, A. D. Wadikar, M. K. Jain, A. Subrahmanyam, "Synthesis of Cu2O from CuO thin films Optical and electrical properties" AIP advances, Vol.5, No. 4, p. 047143, (2015).

[48] Y. Yang, Y. Li, M. Pritzker, "Control of Cu_2O film morphology using potentiostatic pulsed electrodeposition", Electrochimica Acta, Vol. 213, pp. 225-235, (2016).

[49] N. A. Raship, M. Z. Sahdan, F. Adriyanto, M. F. Nurfazliana, A. S. Bakri, "Effect of annealing temperature on the properties of copper oxide films prepared by dip coating technique", AIP Conference Proceeding, Vol. 1788, No. 1, p. 030121. (2017).

[50] R. D. Prabu, S. Valanarasu, V. Ganesh, M. Shkir, A. Kathalingam, AlFaify, "Effect of spray pressure on optical, electrical and solar cell efficiency of novel Cu_2O thin films", Surface and Coatings Technology, Vol.347, pp. 164-172, (2018).

[51] C. Qin, Y. Wang, Z. Lou, S. Yue, W. Niu, L. Zhu, "Surface modification and stoichiometry control of Cu_2O/SnO_2 heterojunction solar cell by an ultrathin MgO tunneling layer", Journal of Alloys and Compounds, Vol.779, pp.387-393, (2019).

[52] M. A. Zahid, S. Q. Hussain, Y. H. Cho, J. Yi, "Optical properties of CaF_2 thin film deposited on borosilicate glass and its electrical performance in PV module applications. Applied Sciences, Vol. 10, No. 16, p. 5647, (2020).

[53] D. O. Ozaslan, O. Erken, M. Gunes, C. E. Gumus, "The effect of annealing temperature on the physical properties of Cu_2O thin film deposited by SILAR method", Physica B Condensed Matter, Vol.580, p. 411922, (2020).

[54] S. M. Butte, and S. A. Waghuley, "Optical properties of Cu_2O and CuO" AIP Conference Proceedings, Vol. 2220, No. 1, p. 020093, (2020).

[55] R. Bunea, A. K. Saikumar, K. Sundaram, "A comparison of optical properties of CuO and Cu_2O thin films for solar cell applications", Materials Sciences and Applications, Vol.2, No. 7. pp. 315-329., (2021).

[56] E. Güneri, D. Aker, J. Henry, C. A. Billur, and B. Saatçi, "Cu_2O thin films prepared by chemical bath deposition: An improved method. Phase Transitions, Vol. 95, No. 10, pp. 679-690, (2022).

[57] A. M. Koshy, A. Sudha, S. K. Yadav, and P. Swaminathan, P., "Effect of substrate temperature on the optical properties of DC magnetron sputtered copper oxide thin films" Physica B: Condensed Matter, Vol. 650, P. 414452. (2023).

[58] J. L. Vossen and W. Kern, "Thin film processes II", Boston academic press, (1991).

[59] J. M. Lafferty, "Vacuum from art to exact science", Phys. today, Vol.34, No.11, pp.211–231, (1981).

[60] R. W. Bery, P. M. Hall and M. T. Harris, "Thin film technology", Van Nostrand Reinhold Company, (1968).

[61] D. M. Mattox, "Foundations of vacuum coating technology", William Andrew publishing/Noyes, (2003).

[62] A. A. Bunaciu, E. G. UdriŞTioiu, and H. Y. Aboul-Enein, "X-ray diffraction instrumentation and applications," Crit. Rev. Anal. Chem., Vol. 45, No. 4, pp. 289–299, (2015).

[63] L. Reimer, Transmission electron microscopy physics of image formation and microanalysis, vol. 36. Springer, (2013).

[64] C. J. Brinker and G. Cao, "Annual Review of Nano Research," (2006).

[65] C. Gumus, O. M. Ozkendir, H. Kavak, and Y. Ufuktepe, "Structural and optical properties of zinc oxide thin films prepared by spray pyrolysis method", J. Optoelectronics and advanced materials, Vol.8, pp.299-303, (2006).

[66] A. Khursheed, Scanning electron microscope optics and spectrometers. World scientific, (2011).

[67] R. Baerga and V. Orlando, ―Laser shockwave sintering of micro and nanoscale powders of yttria-stabilized zirconia, (2010).

[68] L. Reimer, Scanning electron microscopy physics of image formation and microanalysis, Vol. 45. Springer, (2013).

[69] R. Elliot and A. I. Gibson, "An introduction to solid state physics and application", Macillian Inc., Vol. 471, pp.92,(1974).

[70] L. Kazmarski and A. Clark, "Polycrystalline and amorphouse thin films and device", Edited by Lawrence Academic Press, New York, Vol. 267, pp.142, (1980).

[71] Y. N. Al-Jamal, "Solid state physics", Al-Mosel University, 2nd ed., Arabic Version, (2000).

[72] R. A. Smith, "Semiconductors", Cambridge press, 2nd ed., (1987).

[73] B. G. Stereeman, "Solid state electronic devices", 2nd ed, Practice hall, Inc. Engle wood cliffs, N. J., (1980).

[74] A. G. Nilens, "Deep imparity in semiconductors", Wiley -Interscience publication, (1973).

[75] J. I. Pankove, "Optical process in semiconductors", Dover Publishing, Inc., New York, (1971).

[76] C. Kittel, "Introduction to solid state physics", 5th ed., Willy, New York, (1981).

[77] A. N. Donald, "Semiconductor physics and devices", Irwin, USA, (1992).

[78] J. Jaffe and A. Zunger, "Electronic structure of the ternary pnictide semiconductors $ZnSiP_2$, $ZnGeP_2$, $ZnSnP_2$, $ZnSiAs_2$, and $MgSiP_2$", Phys. Rev., Vol.28, No.49, pp.1882-1905, (1984).

[79] D. Bonnell, B. Huey and D. Carroll, "In-situ measurement of electric fields at individual grain boundaries in TiO_2", Solid state ionics, Vol.75, pp.35-42, (1995).

[80] J. Marien, T. Wagner, G. Duscher, A. Koch and M. Rühle, "Ag, Pt, Pd, Nb doping (110) TiO_2 (Rutile), growth, structure, and chemical composition of the interface", surface sci., Vol.446, p.219, (2000).

[81] M. Nnabuchi, "Optical and solid state characterization of optimized manganese sulphide thin films and their possible applications in solar energy", The pacific J. of Sci. and technology, Vol.7, No.1, pp.69-76, (2006).

[82] A. El-Denglawey, M.M. Makhlouf, M. Dongol, The effect of thickness on the structural and optical properties of nano Ge-Te-Cu films, Results Phys. Vol. 10, pp. 714–720, (2018).

[83] S. H. Wemple, “Refractive-Index Behavior of Amorphous Semiconductors and Glasses”, Physical Review Journals B, Vol. 7, No. 8, p.3767, (1973).

[84] A. S. Hassanien and A. A. Akl, “Influence of Composition on Optical and Dispersion Parameters of Thermally Evaporated Non-Crystalline Cd50S50− xSex Thin Films”, Journal of Alloys and Compounds, Vol. 648, pp.280-290, (2015).

[85] F. A. Jenkins, H. E. White,. “Fundamentals of Optics”, Indian Journal of Physics, Vol. 25, pp. 265-266, (1957).

[86] F. S. Ahmed, N. Y. Ahmed, R. S. Ali, N. F Habubi, K. H. Abass, S. S, “Chiad Effects of substrate type on some optical and dispersion properties of sprayed CdO thin films, NeuroQuantology”, Vol. 18, No. 3, pp. 56-65, (2020).

[87] F. Y. akuphanoglua, A. Cukurovalib, and I. Yilmazb, “Physica”, B, Vol. 351, p.53, (2004).

[88] K. H. Abass , A. Adil , A. J. Alrubaie, H. R. .Bahaa, A. M. Kadim, S. H. Talib, K. A. Mohammed and A. S. Jassim, "Fabrication and Characterization of p-SnS/n-Si Solar Cell by Thermal Evaporation Technique and the Effect of Ag-doped on Its Efficiency", International Journal of Nanoscience, Vol. 22, No. 01, P.2350003, (2023).

[89] H. Wang, R. Liu, K. Chen, X. Shi, Z. Xu, "Electrodeposition and characterization of CaF_2 and rare earth doped CaF_2 films". Thin Solid Films, Vol. 519, pp. 6438–6442, (2011).

[90] M. A. Zahid, S. Q. Hussain, Y. H. Cho, J. Yi, J. , "Optical properties of CaF_2 thin film deposited on borosilicate glass and its electrical performance in PV module applications" Applied Sciences, 10(16), 5647. (2020).

[91] A. Jafari, K. Tahani, D. Dastan, S. Asgary, Z. Shi, X. T. Yin, S. Ţălu, "Ion implantation of copper oxide thin films; statistical and experimental results. Surfaces and Interfaces, Vol.18, p.100463, (2020).

[92] R. P. Yadav, R. K. Pandey, A. K. Mittal, M. Kumar, A. C. Pandey, "Surface roughness and fractal study of CaF_2 thin films" Materials Focus, Vol. 4, No. 6, pp. 403-408, (2015).

[93] R. G .Kadhim, "Study of Some Optical Properties of Polystyrene-Copper Nanocomposite Films", World Scientific News, Vol. 30, p.14-25, (2016).

[94] M. Dai, S. Lin, Q. Shi, F. Liu, W. Wang, S. Chen, T. Kuo and H. Sun, "Transparent conductive p-type cuprous oxide films in Vis-NIR region prepared by ion-beam assisted DC reactive sputtering", Coatings, Vol.10, No.5, pp.1–9, (2020).

[95] S. Karvinen, "The effect of trace element doping of TiO_2 on the crystal growth and on the anatase to rutile phase transformation of TiO_2", Solid State Sci., Vol.5, pp.811-819, 2003.

[96] A. N. Tuama, K. H. Abass, M. A. B. Agam, "Efficiency enhancement of nano structured Cu2O Ag/laser etched silicon-thin films fabricated via vacuum thermal evaporation technique for solar cell application", Optik, Vol.247, p.167980, (2021).

[97] K. Khurana, A. K. Patel and K. Das, "Refractive Indices Studies on PVA and PVP Blends", International Journal for Scientific Research & Development, Vol. 4, pp.984-985, (2016).

[98] O. Gh. Abdullah, "Influence of Barium Salt on Optical Behavior of PVA Based Solid Polymer Electrolytes", European Scientific Journal, Vol.10, No.33, (2014).

[99] H. Hakim, N. Al- Garah and A . Hashim, "The Effect of Aluminum Oxide Nanoparticles on Optical Properties of (Polyvinyl alcohol-Polyethylene glycol) Blend", Journal of Industrial Engineering Research, Vol. 1, pp.94-98, (2015).

[100] W. X. Cheng, A. L. Ding, X. S. Zheng, P. S. Qiu and X. Y. He, "Optical and electrical properties of ZnO nanocrystalline textured films prepared by DC reactive magnetron sputtering", J. of phys. Conference Series, Vol.152, No.1, (2009).

[101] J. J. Mathen, G. P. Joseph, J. Madhavan, “Improving the optical and dielectric properties of PVA matrix with nano-ZnSe Synthesis and Characterization”, International Journal of Engineering Development and Research, Vol. 4, No.3, pp.1088-1092, (2016).

[102] A.I. Ali, J.Y. Son, A.H. Ammar, A. Abdel Moez, Y.S. Kim, Optical and dielectric results of Y0.225Sr0.775CoO3±δ thin films studied by spectroscopic ellipsometry technique, Results Phys. 3 (2013) 167–172.

[103] K. H. Abass, D. M. A. Latif, "The urbach energy and dispersion parameters dependence of substrate temperature of CdO thin films prepared by chemical spray pyrolysis", International Journal of Chem. Tech Research, Vol. 9, No.9, pp. 332-338, (2016).

الخلاصة

في هذا العمل ، تم تحضير اغشية رقيقة من $Cu_2O_{(0.75)}:CaF_{2(0.25)}$ بتقنية التبخير الحراري تحت ضغط مقداره ($1x10^{-7}$ mbar) وبمعدل ترسيب0.5 نانومتر بالثانية مرسبه على قواعد من الزجاج بدرجة حرارة الغرفة وبسماك مختلفة (١٦، ١٩، ٢٢، ٢٩، ٣٥، ٤٢ ، ٥٠ و ٥٧) نانومتر. تم فحص الخواص التركيبية، المورفولوجية والبصرية.

أظهرت نتائج حيود الأشعة السينية (XRD) أن الأغشية المحضرة كانت غير متبلورة. مع زيادة السمك، تظهر قمة عند $2\theta= 24.2^o$والتي تُعزى إلى CaF_2 التي تتوافق مع (111) مع مكعب مركز الوجه، بينما يمكن أن تُعزى القمة عند $2\theta=7^o$ إلى التفاعل بين الجسيمات النانوية Cu_2O و CaF_2 و الذي سوف يؤدي إلى تكون طور جديد ، وبالتالي لا يمكن الحصول عند هذه القمة على معامل ميلر. أكد فحص مجهر للقوة الذرية (AFM) أن الأغشية التي نمت بهذه التقنية لها سطح متجانس جيد. زاد متوسط الخشونة وجذر متوسط القيمة التربيعية ومتوسط قطر الحبيبة مع زيادة السمك. المجهر الإلكتروني الماسح (FE-SEM) اظهر ان التشكل المنتظم يكشف عن سطح ناعم إلى حد ما ومع زيادة السمك أدى إلى تغيرات في شكل السطح وزيادة الخشونة. أظهرت نتائج الخواص البصرية أن كل من الامتصاصية، معامل الامتصاص، ومعامل الخمود، ومعامل الانكسار، وثابت العزل الحقيقي والخيالي ، والتوصيلية البصرية تزداد بزيادة السمك بينما تقل قيمة كل من النفاذية وفجوة الطاقة مع زيادة السمك. وجد ان فجوة الطاقة المسموحة للأغشية الرقيقة $Cu_2O_{(0.75)}:CaF_{2(0.25)}$ انخفضت من 3.77 إلى 3.62 الكترون فولت مع زيادة السمك. أيضا لوحظت قيم كل من دالة الفقدان الطاقة السطحية (SELF) و دالة الفقدان الطاقة الحجمية (VELF) يزدادان مع زيادة السمك. اما معاملات التشتت فلقد تم حساب $\varepsilon_\infty, E_o, E_d, n_o, n_2$, M_{-1} , M_{-3}باستخدام انموذج Wemple-DiDomenico كانت قيمة فجوة الطاقة المقدرة بواسطة حسابات Wemple-DiDomenico متوافقة مع قيمة فجوة الطاقة البصرية التي تم الحصول عليها من علاقة Tauc حيث وجدت أن المعاملات تقل مع زيادة السمك.

.

جمهورية العراق
وزارة التعليم العالي والبحث العلمي
جامعة بابل
كلية التربية للعلوم الصرفة
قسم الفيزياء

دراسة الطاقات لأغشية $Cu_2O:CaF_2$ النانوية المحضرة بتقنية التبخير الحراري

رسالة مقدمة

الى مجلس كلية التربية للعلوم الصرفة في جامعة بابل

وهي جزء من متطلبات نيل درجة الماجستير

في التربية / الفيزياء

من قبل الطالبة

جنان هاشم علي عباس

بكالوريوس علوم في الفيزياء

جامعة بابل ٢٠١٢ م

بأشراف

أ. د. خالد حنين عباس

٢٠٢٣ م

١٤٤٥ هـ